

# **DEVELOPMENT AND CHARACTERIZATION OF MICRO NEEDLES BASED ELECTRODE FOR BIOPOTENTIAL MEASUREMENT**

Thesis

Submitted in partial fulfillment of the requirements for the degree of

**DOCTOR OF PHILOSOPHY**

by

**N. BALASHANMUGAM**



**DEPARTMENT OF MECHANICAL ENGINEERING  
NATIONAL INSTITUTE OF TECHNOLOGY, KARNATAKA,  
SURATHKAL, MANGALORE - 575 025  
NOVEMBER, 2016**



## **DECLARATION**

I hereby declare that the research thesis entitled “**DEVELOPMENT AND CHARACTERIZATION OF MICRO NEEDLES BASED ELECTRODE FOR BIOPOTENTIAL MEASUREMENT**” which is being submitted to the **National Institute of Technology Karnataka, Surathkal** in partial fulfilment of the requirements for the award of the Degree of **Doctor of Philosophy** in **Mechanical Engineering** is a *bonafide report of the research work carried out by me*. The material contained in this research thesis has not been submitted to any University or Institution for the award of any degree.

Register Number: **ME11P02**

Name of the Research Scholar: **N. Balashanmugam**

Signature of the Research Scholar :

Department of Mechanical Engineering

Place: NITK-Surathkal

Date:



## **CERTIFICATE**

This is to certify that the research thesis entitled “**DEVELOPMENT AND CHARACTERIZATION OF MICRO NEEDLES BASED ELECTRODE FOR BIOPOTENTIAL MEASUREMENT**” submitted by **Mr. N. BALASHANMUGAM (Register No. ME11P02)** as the record of the research work carried out by him, *is accepted as the Research Thesis submission* in partial fulfillment of the requirements for the award of the degree of **Doctor of Philosophy**.

**Prof. Mohan Kumar G C**

Research Guide

Date:

**Prof. Prasad Krishna**

Research Guide

Date:

**Chairman-DRPC**

Date:



**DEDICATED**  
**TO**  
**MY LATE FATHER**



## ACKNOWLEDGEMENTS

I would like to extend special thanks and gratitude to my guides **Prof. Prasad Krishna** and **Prof. G. C. Mohan Kumar**. Thanks for all the inspiring and wonderful discussions, encouragement and patience they provided throughout my research work at **National Institute of Technology Karnataka, Surathkal**. Special thanks go to **Prof. V. R. Sastry** and **Dr. S. M. Murigendrappa** for spending their valuable time in advising me from the very beginning of my research. It has been always a great treasure to me to have them in my committee for training me and for those valuable discussions and suggestions in every step of my research. Also, I am highly indebted to **Mr. K. Naveen**, **Mr. A. Daniel**, **Mr. Ankit. K**, **Mr. Hari Thota**, **Mr. M. A. Manjunath**, **Dr. Aravindha Bhatt**, **Mr. Jagadesh**, **Mr. V. R. Raju** and the entire team of CMTI. I must appreciate their ever-ready helping attitude.

I wish to express my sincere thanks to **Prof. S. Mohan**, **Prof. Arun N. Umarji**, **IISc, Bangalore**, **Mr. B. R. Satyan**, and **Mr. P. V. Shashikumar**, Central Manufacturing Technology Institute (CMTI), Bangalore, especially for visualizing the direction and creating a platform to pursue research.

The continuous support and encouragement provided by **Dr. K. Raghavendra**, **Mrs. S. Usha**, **Mr. P. Rajashekar**, **Mr. V. Shanmugraj**, **Mr. Mahanthesa**, **Dr. N. H. Satheesh**, **Mr. Veeresh Naik**, **Mr. Vignesh** and **Dr. Manjaiah** is worth appreciation. I am also very grateful to all my research friends and my classmates of the Mechanical Engineering Department for their wonderful friendship and help.

Grateful acknowledgement to **Dr. J. K. Radhakrishnan**, DEBEL, Bangalore for helping me in materializing the ideas leading to fruitful research work. Thanks are also due to all the members of staff of the Mechanical Engineering Department, National Institute of Technology Karnataka, Surathkal, who taught me and gave me the scientific base to continue my postgraduate studies. Special thanks go to all the Professors and HOD of Mechanical Engineering Department for their support during my former study.

My most sincere gratitude and appreciation goes to **Smt. Kamalam**, my mother, an all-time inspiration for her patience, continuous encouragement and support

over the past difficult years. Thanks to my father-in-law **Mr. M. Shanmugasundaram**, my wife **Smt. Sathya**, my beloved sisters **Smt. Bharathi**, **Smt. Chitra** and my son **Master. Adhi Pritish. B** for their unrelenting and unconditional support. I am deeply indebted to all my friends, who gave me continuous support and encouragement throughout my life.

*Balashanmugam N*

## **ABSTRACT**

### **Development and Characterisation of Microneedles Based Electrode for Biopotential Measurement**

Bio potential signals of human brain activity are used to monitor the health of an individual. The electroencephalogram (EEG) is a record of the electric signals of the brain activity and is useful in diagnosis, treatment of various diseases, and monitoring the fatigue and alertness of a personnel.

The current electrodes are not suitable for portable and long-term recording applications. Also, the conventional biopotential electrodes demand for additional skin preparation and need conductive gel. However, conductive gel may cause allergic reactions or skin irritation. Microneedle electrodes are dry electrodes and do not require any skin preparation and conductive gel. Microneedles pierce into the skin and keep direct contact with the conductive epidermal layer of the skin and are promising for long-term recording applications.

The research work is carried out to identify suitable materials for microneedle fabrication for biopotential measurement. Microneedle design is carried out by taking skin anatomy and their properties into consideration. Finite Element Analysis (FEA) is carried out to optimize pitch and base diameter for maximum penetration of the skin and minimum strain of the microneedles.

Research is carried out initially using micro-stereolithography (MSL) system to realise microneedles. The research work investigated fabrication of microneedle using Hexanediol diacrylate (HDDA) by UV photo polymerisation. Novel method of step less fabrication of HDDA microneedle by MSL is presented. Investigation carried out to co-polymerise HDDA and PMMA using MSL system is presented. Samples are characterized using FTIR. FTIR spectrum of samples shows limitations in curing PMMA.

Replication technique carried out for micro mould fabrication is presented. The Teflon negative mould is used for making positive polydimethylsiloxane (PDMS) micro mould, which is again used for making PDMS negative mould. The PDMS microneedle fabricated by this work is used as master for subsequent microneedle fabrication using PMMA. It was observed that the PMMA sticks to PDMS mould.

Further, the work is carried out to fabricate microneedles using micromachining centre. Layer-by-layer machining strategy is adopted with varying machining parameters at different heights of microneedles. Microneedle array consisting of 10×10 microneedles having base and tip diameters 120 µm and 5 µm, height 200 µm and pitch 400 µm are micro milled. Fabricated needles are tested for compression, shear and penetration into chicken skin.

Characterisation results of microneedles and chicken skin penetration test results are presented. The results of tests show the microneedles have capability for skin penetration. To make PMMA microneedles electrically conductive, electroless silver plating has been carried out. Electrical testing of needles conducted shows that the needles offer less electrical resistance. The results show that PMMA microneedles with conductive layer are found to be suitable for biopotential measurement.

*Key words: Microneedle, Biopotentials, Polymethyl methacrylate, Micro-Stereo lithography, Micro Milling, Electroless Silver Plating*

# Contents

<b>Title</b>	<b>Page No.</b>
Acknowledgement	
Abstract	
Contents	i
List of Figures	iv
List of Tables	ix
Notations	xi
Abbreviations	xii
<b>Chapter 1 Introduction</b>	<b>1-13</b>
1.1 Overview	1
1.2 Skin Anatomy	2
1.3 Biopotential Signals	3
1.4 Research Hypothesis and Objectives	11
<b>Chapter 2 Literature Survey</b>	<b>15-42</b>
2.1 Introduction	15
2.2 Microneedle Fabrication, Testing and Characterisation	15
2.3 Materials for Micro Needle	36
2.4 Comparison of Mechanical Properties of Needle Materials	39
2.5 Summary	40
<b>Chapter 3 Microneedle Design and Analysis</b>	<b>43-65</b>
3.1 Introduction	43
3.2 Parameters for Design	44
3.3 Force Req'd. to Pierce the Human Skin	44
3.4 Forces Acting on Microneedle	45
3.5 Maximum Bending Force	46
3.6 Maximum Axial Force	47
3.7 Maximum Shear Force	51
3.8 Deformation of Microneedle	52

3.9	Finite Element Analysis	53
3.9.1	Model Information	55
3.9.2	Meshing	57
3.9.3	Output from FEA	58
3.10	Load Vs. Penetration and Strain	60
3.11	Summary	64
<b>Chapter 4</b>	<b>Experimentation</b>	<b>67-108</b>
4.1	Introduction	67
4.2	Fabrication of Microneedles	68
4.2.1	Fabrication of Microneedle by UV Curing	68
4.2.2	Microneedle by Micro Molding	82
4.2.3	Micro Milling of Micro Needles	86
4.3	Conductive Coating	95
4.3.1	Electroless Silver Coating	96
4.4	Peel Off Test for Coating	98
4.5	Compression Test for PMMA Micro Needle	99
4.6	Shear Test	103
4.7	Insertion Test	105
4.8	Test for Conductivity	106
4.9	Summary	107
<b>Chapter 5</b>	<b>Results and Discussion</b>	<b>109-133</b>
5.1	Results of FEM Analysis	109
5.2	Optimization of Parameters for PMMA Curing	111
5.3	Results of Co-Polymerisation	113
5.4	Experimentation on Micro Needle Mould Fabrication	118
5.5	Results of Micro Machining	119
5.6	Electro Less Silver Plating	120
5.7	Skin Impedance Measurement	126
5.8	EEG Signal Acquisition	127
5.9	Compression Test Results	128
5.10	Shear Test Results	130

5.11	Insertion Test Results	132
<b>Chapter 6</b>	<b>Conclusions and Scope for Future work</b>	<b>135-138</b>
6.1	Conclusions	135
6.2	Scope for Future Work	138
	<b>References</b>	139-148
	<b>List of Publications</b>	149-150
	<b>Bio Data</b>	151
<b>Appendix I</b>	Results of Finite Element Analysis	153-161
<b>Appendix II</b>	Plots on Skin Penetration and Needle Strain Vs. Base Diameter	163-185
<b>Appendix III</b>	Micro Needle Dimensions after Micro Machining	187-190
<b>Appendix IV</b>	Summary of Micro Needle Dimensions after Micro Machining	191

## LIST OF FIGURES

<b>Figure No.</b>	<b>Title</b>	<b>Page No.</b>
1.1	(a) Skin Anatomy (b) Cross Section of Human Skin	2
1.2	Cell Wall and Potassium and Sodium Ions	4
1.3	Typical Action Potential	5
1.4	EEG Signal for Various Activities	6
1.5	Cup Electrodes for Measurement of EEG	9
1.6	(a) Spiked Electrode (b) Conventional Electrode	10
2.1	Combination of Isotropic and Anisotropic Etching Process for Out of Plane Fabrication of Microneedle	15
2.2	Hollow Microneedles With Reservoir (For Filling NaCl) for ECG Measurement	17
2.3	3D Printed Microneedle Made Out of Bio Compatible Acrylic Based Resin	18
2.4	Steps Involved in Microneedle Fabrication	19
2.5	(a) and (b) 2 Scale Topography of Microneedle Fabricated by Vacuum Casting Technology	19
2.6	Scheme of Electrically Activated Microneedle Array for DNA Vaccination	20
2.7	Fabrication of Su-8 Micro Mold, Microneedle and Formation of Microneedle Electrode	22
2.8	Yield Stress Values of Different Configurations (Rectangular, Square and Circular) of Microneedles	23
2.9	Mosquito Head and Proboscis and Fascicle Tip With Labella Retracted	24
2.10	Stress Analysis	24
2.11	FEM Analysis of Indentation of Skin	25
2.12	Axial Fracture Force Measurement and Transverse Shear Force Measurement	26
2.13	Mechanical Analysis of Polymeric Micro Needles Under Axial	27

	and Transverse Loading.	
2.14	Fracture Force Vs. Microneedle Interfacial Area and Insertion Force Vs. Microneedle Interfacial Area	28
2.15	Experimental Setup and Measurement of Axial Fracture Force, Shear Force and Skin Insertion Force	29
2.16	400 $\mu\text{m}$ Tall Silicon Microneedle	37
2.17	Sugar Microneedle	38
3.1	Forces Acting on Microneedle	45
3.2	Bending Force on Microneedle	46
3.3	Axial Force on Microneedle	47
3.4	Microneedle Block with Tetrahedral Solid Mesh	57
3.5	Strain Plot	58
3.6	Displacement Plot	59
3.7	Plot on Penetration, Strain Vs. Base Diameter at 6 N Load for Pitch 0.4 mm & 0.6 mm	60
3.8	Plot on Penetration, Strain Vs. Base Diameter at 8 N Load for a Pitch 0.4 mm	61
3.9	Plot on Penetration, Strain Vs. Base Diameter at 9 N Load For Pitch 0.4 mm & 0.6 mm	62
3.10	Plot on Penetration, Strain Vs. Base Diameter at 10 N Load for a Pitch of 0.4 mm	63
4.1	The Cure Mechanism	69
4.2	Photo Polymerization	70
4.3	2D Structure of 1,6-Hexanedioldiacrylate	71
4.4	2D Structure of Benzoin Ethyl Ether	72
4.5	Schematic Diagram of Micro Stereo Lithography Set Up	73
4.6	Structure of MSL Process	74
4.7	MSL Setup	74
4.8	Schematic Diagram of Micro Stage, Petri Dish and Focused UV Light	74
4.9	Gaussian Beam Profile	77

4.10	Microneedles Fabricated by Varying the Intensity	78
4.11	MMA Photo Polymerization	79
4.12	Schematic Diagram of UV LED Lamp Setup	80
4.13	Precision Tool Grinder	83
4.14	Carbide Micro Indenter & Micro Drill	83
4.15	Micro Molding	84
4.16	Micro Holes Drilling Using Micromachining Centre on Teflon Mould	85
4.17	Block Diagram for Micromachining	87
4.18	CAD Model of Microneedle Array	87
4.19	End Mill ( $\varnothing$ 0.2mm) for Micro Milling	89
4.20	Tool Path for Removal of External Surface	91
4.21	Simulation of Tool Path	91
4.22	Simulation of Tool Path for Machining Microneedle	92
4.23	Kern 5 Axis Micro Machining Centre	93
4.24	Microneedle Machining Setup With High Speed Milling Spindle	93
4.25	Micro Machined PMMA Needles	94
4.26	Schematic Representation of PMMA Microneedle Coated With Silver	96
4.27	Generic Reactions for Silver Deposition	97
4.28	Silver Coated Samples for Peel Off Test	98
4.29	Schematic Diagram of Compression Test of Microneedle	99
4.30	Test Setup for Compression Test	99
4.31	Micro Machine Tool for Compression Test	100
4.32	Image of Microneedles Under Compression	101
4.33	Mini Dyn Multi Component Dynamometer	101
4.34	Compression Image Captured Through Camera	102
4.35	SEM Image of Compressed Microneedles	103
4.36	Schematic Diagram of Shear Test of Microneedles	103
4.37	Set Up for Shear Test	104

4.38	Needles Under Shear	104
4.39	Schematic Diagram of Test Setup for Piercing Chicken Skin by Microneedle	105
4.40	Test Setup for Piercing Chicken Skin by Microneedle	106
4.41	Electrical Resistance Measurement Using Multimeter	107
5.1	FEM Analysis-PMMA Microneedle Skin Penetration	109
5.2	Load Vs. Strain & Penetration	110
5.3	Influence of Cure Time on Elastic Modulus of PMMA & Influence of PI Concentration on Hardness of PMMA	112
5.4	Nano Indentation Test to Define Hardness & Modulus Variation With Indentation Load	113
5.5	FTIR Spectrum of HDDA	114
5.6	FTIR Spectrum of BEE	115
5.7	FTIR Spectrum of MMA	116
5.8	FTIR Results of Sample Fabricated at 0.5 mm/Sec	117
5.9	FTIR Results of Sample Fabricated at 1 mm/Sec	117
5.10	FTIR Results of Sample Fabricated at 1.5 mm/Sec	118
5.11	(a) PDMS Microneedle Array (b) SEM Image of PDMS Microneedle Array	119
5.12	(a) SEM Image of Microneedle Arrays (b) Top View of Needles	119
5.13	SEM Image of Single Micro Needle	120
5.14	Images of Roughened Surface With Different Grit Papers	120
5.15	Images of Roughened Surface With Different Grit Papers After Coating	121
5.16	Stacked XRD Spectrum of Silver Coated Polymer	121
5.17	Surface Roughness of Samples	122
5.18	FESEM Images of Coated Samples	123
5.19	Peel Off Test After Electroless Deposition	124
5.20	Resistance Measurement	125
5.21	Impedance Measurement	126

5.22	EEG Signal Acquisition Set up	127
5.23	Signal acquired at (a) Subject in active state (eyes open) (b) Subject in inactive state (eyes closed)	127
5.24	Compression Test on Micro Needles Array (a) Needles before the Test (b) & (c) Needles after the Application of Compressive Load	128
5.25	Compressive Load Vs. Deformation	129
5.26	Shear Test Images (a) Needle Before Shear (b) & (c) Needle After the Application of Shear Load	130
5.27	Results from Shear Test	131
5.28	Insertion Test (a) Test Rig (b) Chicken Skin Under Insertion (c) & Needle Before Insertion (f) Needle After Insertion (d) & (e) Chicken Skin After Insertion	132
5.29	Load Vs. Deformation Plot	133

## LIST OF TABLES

<b>Table No.</b>	<b>Title</b>	<b>Page No.</b>
1.1	Bio Potential Signal Characteristics	3
1.2	EEG Band Width and its Applications	7
1.3	Spiked Electrodes Vs. Conventional Electrode	11
2.1	Fracture Failure Values of Polymers Due to Axial and Transverse Forces	28
2.2	Processes Used for Micro-Needle Fabrication and Features of it	30
2.3	Comparison of Microneedles Developed by Various Researchers	35
2.4	Mechanical Properties of Micro-Needle Materials	40
3.1	Force Required for Piercing the Skin	45
3.2	Maximum Bending Force of Microneedle	47
3.3	Slenderness Ratio	49
3.4	Critical Load of Failure	51
3.5	Maximum Shear Force	52
3.6	Load Vs. Deformation of Microneedle	53
3.7	Constant Parameters/Dimensions	54
3.8	Minimum & Maximum Value of Variables for FEM Analysis	54
3.9	Microneedle Dimensions & Variables	54
3.10	Model Information for FEM Analysis	55
3.11	Physical Properties of Microneedle	56
3.12	Physical Properties of Skin	56
3.13	Parameters Considered for Meshing	57
3.14	Strain and Penetration for Applied Load	64
4.1	Comparison of various processes	67
4.2	Properties of 1,6-HDDA Monomer	71
4.3	Properties of BEE Photo Initiator	72
4.4	Power of The Laser Beam, Voltage and the Distance of Focal	77

	Point	
4.5	Dimensions of Fabricated Micro Needles	78
4.6	Micro Machining Process Parameters	86
4.7	Cutting Tool Data for Face Milling	89
4.8	Cutting Tool Data for Micro Milling of Needles	89
4.9	Process Parameters for Face Milling	90
4.10	Process Parameters for Micro Milling of Needles	90
5.1	FEA Input Parameters and the Results	110
5.2	Mechanical Properties for Varied PI Concentration and Curing	112
	Depth	
5.3	Stretching Frequencies of HDDA	114
5.4	Stretching Frequencies of BEE	115
5.5	Stretching Frequencies of MMA	116
5.6	Surface Roughness Values Before and After Coating	123
5.7	Resistivity of the Sample	125
5.8	Skin Electrode Impedance Values (with wet electrode as reference and ground)	126
5.9	Skin Electrode Impedance Value (with dry electrode as reference and ground)	126

## NOTATIONS

Ag	Silver
Ag NO <sub>3</sub>	Silver Nitrate
AgCl	Silver chloride
Ar <sup>+</sup>	Argon Ion
B	Spot Diameter
C <sub>d</sub>	Curing Depth
Cl <sup>-</sup>	Chloride Ion (-ve)
C <sub>w</sub>	Curing Width
DLC	Diamond Like Carbon Coating
D <sub>p</sub>	Depth penetration.
D <sub>p</sub>	Depth Penetration
E <sub>c</sub>	Critical Energy Required to Convert Resin to Solid State.
E <sub>max</sub>	Maximum Energy Falling on Resin Surface
K <sup>+</sup>	Potassium Ion (+ve)
Na <sup>+</sup>	Sodium Ion (+ve)
NaOH	Sodium Hydroxide
P	Power of the UV Beam Falling on Resin Surface.
P <sub>i</sub>	Initiator Molecule
PM	Polymerisation initiative Molecules
SiO <sub>2</sub>	Silicon Oxide
W <sub>o</sub>	Gaussian Radius (Half Value of Spot Diameter)

## ABBREVIATIONS

ASTM	American Society for Testing and Materials
BEE	Benzoin Ethyl Ether
CAD	Computer Aided Design
CAM	Computer Aided Manufacture
DLC	Diamond Like Carbon
DRIE	Deep Reactive Ion Etching
ECG	Electrocardiogram
EEG	Electroencephalogram
EMG	Electromyogram
FEM	Finite Element Method
FTIR	Fourier Transform Infra-Red spectroscopy
HDDA	Hexadialdiacrylate
k $\Omega$	Kilo Ohms
LED	Light Emitting Diode
MEMS	Micro Electro Mechanical System
mN	Milli Newton
PDMS	Polydimethylsiloxane
PLGA	Poly Lactic Co-glyctic acid
PMMA	Polymethyl metha acrylate
SEM	Scanning Electron Microscopy
UTM	Universal Testing Machine
XRD	X-Ray Diffraction
$\mu\text{m}$	Micrometer
$\mu\text{SL}$	Micro Stereo Lithography

# CHAPTER 1

## 1 INTRODUCTION

### 1.1 OVERVIEW

Biopotential signals like electroencephalogram (EEG), electrocardiogram (ECG) and electromyogram (EMG) are important in monitoring and understanding the pathological and physiological conditions of human beings. EEG, ECG and EMG are biopotential signals acquired from brain, heart and muscle activities, respectively. Use of these biopotential signals is on the rise for various special applications. Traditionally, to get these signals, silver (Ag)/silver Chloride (AgCl) electrodes or gold disks are used. Skin surface is prepared by abrading and then applying a conductive gel between the electrode and the skin to enhance the conductivity. These electrodes are called as wet electrodes. Conductive gel is an electrolyte used as a conductive gel between skin and electrode. The conductive gel can only be used for short time, as it gets dried out over the time and loses its conductivity leading to higher contact impedance (Conor et al., 2011). These wet electrodes are also sensitive to motion artefacts. Also, the electrolyte gel may also cause irritation to the skin.

There are applications where the human subject's biopotentials need to be measured in motion. Application could be to monitor the EEG signal of pilots for alertness or soldiers deployed at borders for monitoring fatigue. These EEG signals need to be tapped continuously to get the mental alertness of subjects. There is a need to use the electrodes for a longer time without causing any irritation to skin, and at the same time electrodes are expected to give biopotential signals on par or better than the wet electrodes without giving any motion artefacts. Sweat accumulation affects the conductivity, which is an issue during long-term usage (Minjae et al., 2015). To overcome the disadvantages caused by the conventional electrodes, various dry electrodes of invasive type have been studied. Conor et al. (2011) studied about silicon-based microneedle array with conductive metal coating on it to acquire ECG signals. The results showed good biopotential signals in terms of signal acquisition

and fidelity. Elena et al. (2012) studied the microneedle array-based dry electrode for EEG, ECG and EMG measurements. Study showed promising results of microneedle-based electrodes and concluded that these electrodes are promising alternative to wet electrodes. Li-Sheng et al. (2014) studied barbed microneedle array-based electrode for EEG and ECG recording and concluded that the results are comparable to wet electrodes. There is a gap exists in realising cost effective bio compatible microneedle based electrode for measuring EEG signal for longer duration.

## 1.2 SKIN ANATOMY

Anatomy of skin is important for designing microneedles. The human skin has three layers, namely stratum corneum, epidermis and dermis as illustrated in Figure 1.1 (www.philipsplastics.com). Stratum corneum (SC) is the top layer of the skin that acts as a barrier for microneedle insertion. It is made of dead, flat skin cells that shed about every 2 weeks (Heather, 2014).

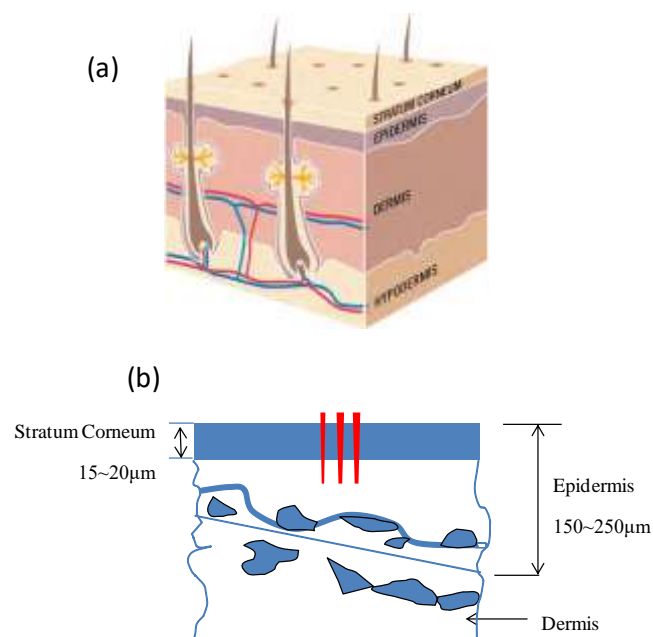


**Figure 1.1** (a) Skin Anatomy (b) Cross-Section of Human Skin  
(www.philipsplastics.com)

Epidermis lies below the stratum corneum. Stratum corneum is of 15 to 20 μm thickness and has less number of nerves and blood vessels. Epidermis thickness varies

from 150 to 250  $\mu\text{m}$  and it has a tissue of living cells. Stratum corneum acts as barrier and causes impedance, which needs to be overcome. Force of 0.1 N to 0.45 N is required to pierce through SC (Henry et al., 1998) reported that the penetration of the microneedle into epidermis is painless, as it is not touching the nerves. Microneedle is not required to reach dermis, which contains living cells, nerves and blood vessels as otherwise it is painful, but it has to penetrate through the stratum corneum and able to have more contact with the living cells of epidermis. Hence, the study of skin anatomy is very important in analysing the effective working of microneedles.

### 1.3 BIOPOTENTIAL SIGNALS

Typical electrical signals or biopotentials that are commonly monitored are ECG from the heart, EEG from brain and electromyograms (EMG) from muscles. The measured signals have extremely small amplitudes in the range of micro-volts. Usually, gold-plated electrodes are secured on the scalp to get EEG signals with low resistance (Nitish, 2000). Characteristics of biopotential signals are tabulated below.

**Table 1.1** Biopotential Signal Characteristics

<b>Signal</b>	<b>Name</b>	<b>Amplitude (mV)</b>	<b>Frequency Range (Hz)</b>
ECG	Electrocardiogram	0.5-5.0	0.01-250
EEG	Electroencephalogram	0.01-50.0	0.1-100
EMG	Electromyogram (surface electrode)	0.1-10.0	0.01-10,000
EMG	Electromyogram (needle electrode)	0.05-5.0	0.01-10,000
ENG	Electroneurogram	0.05-10.0	0.01-1,000

Biopotentials are result of bodily activities. These potentials are measured and used as signals for health monitoring and/or for diagnosis. Measured signals compared with the standard reference signals, and the difference is used for accurate diagnosis. Characteristic signals are amplitude, frequency/time duration and wave shape.

There are biological interferences from skin, electrodes, motion, etc., and noise from environmental sources like power line, radio frequency, electromagnetic, etc.

As shown in Figure 1.2, beneath the skin, human body has ions like sodium  $\text{Na}^+$ ,  $\text{Cl}^-$ , and potassium  $\text{K}^+$ . There is difference in ion concentration depending upon the activities. Ionic Potential difference occurs between two points of ionic concentrations.

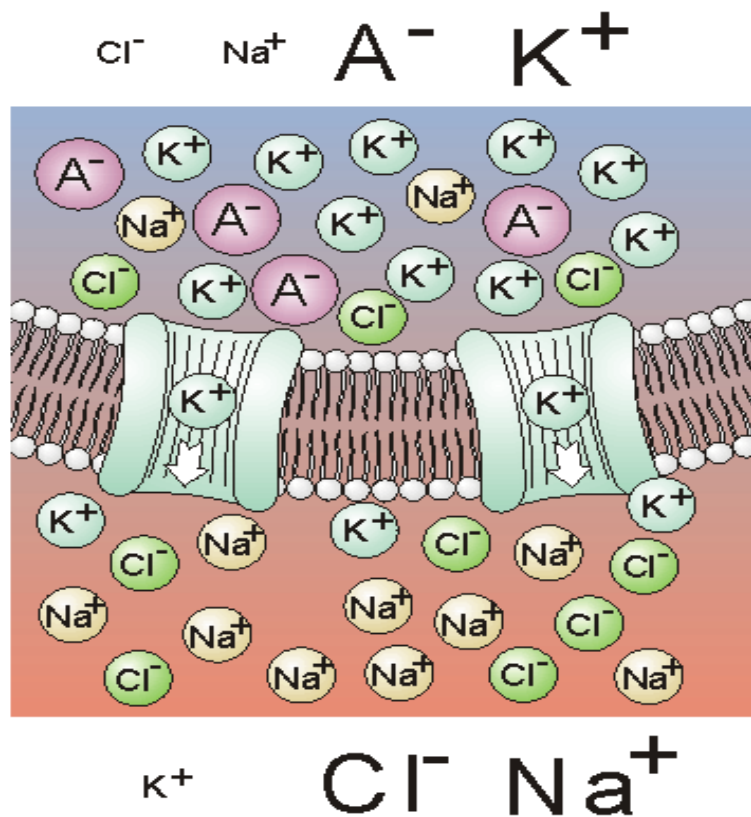


**Figure 1.2** Cell Wall and Potassium and Sodium Ions (Teemu, 2006)

Permeability of the cell changes depends upon the activities. At rest, the cell is more permeable to ions like  $\text{K}^+$  and  $\text{Cl}^-$  than to  $\text{Na}^+$ . Potassium ions ( $\text{K}^+$ ) are pumped in, and sodium ( $\text{Na}^+$ ) ions are pumped out of the cell.

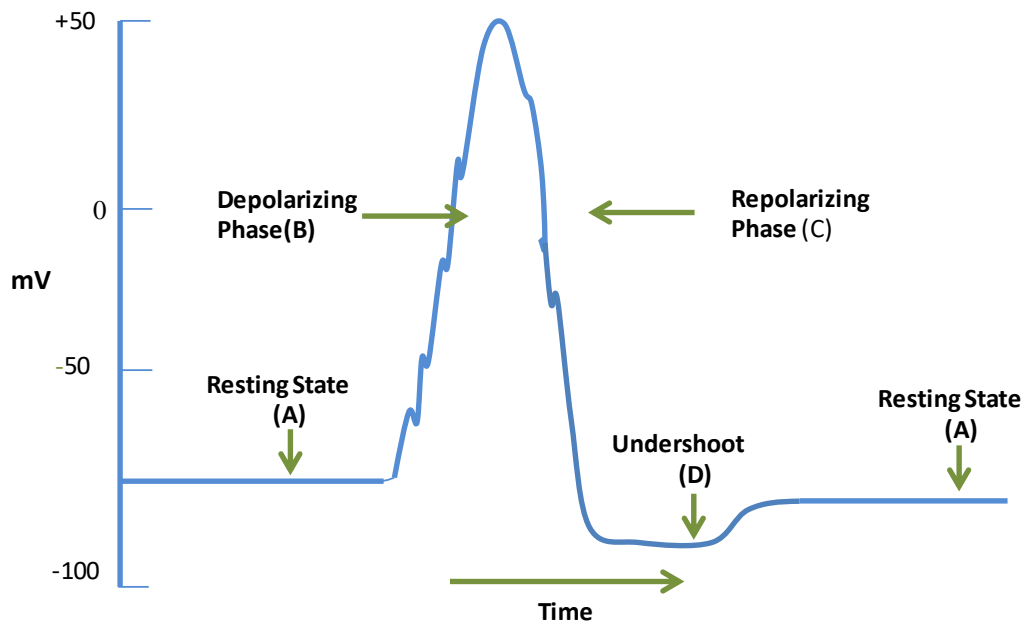


**Figure 1.3** Typical Action Potential

This results in differential rate of pumping of ions ( $\text{Na}^+ > \text{K}^+$ ) and leads to establishment of negative electrical potential of about  $-70$  mV between the inside and outside membrane of the cell. Cell is considered as polarised. Potassium ions ( $\text{K}^+$ ) are pumped out, and sodium ( $\text{Na}^+$ ) ions are pumped into the cell. This again results in differential rate of pumping of ions ( $\text{K}^+ > \text{Na}^+$ ) and leads to establishment of positive electrical potential, which is about  $-20$  to  $40$  mV and lasts for few seconds.

Cell gets depolarised. After some time, the cell permeability returns to original value and the restoration of rest potential happens. Cell is said to be repolarised. The resulting variation in cell potential with respect to time is called as action potential. Figure 1.3 shows the typical action potential. Action potentials produced by combination of many cells result EEG signals. When the wave of ions reaches the electrodes on the scalp, they can push or pull the electrons on the electrode. The difference in push or pull can be measured by a voltmeter. Recording this over time gives us the EEG.

The EEG is defined as electrical activity recorded from the scalp surface after being picked up by metal electrodes and conductive media (Teplan, 2002). EEG measures the electric activity of brain from scalp. It results from the activities of billions of neurons. EEG signal has an amplitude range of 0.001-0.01 mV, bandwidth of 0.5-40 Hz. Figure 1.4 shows the amplitude and bandwidth for various activities.

### EEG in the States of Vigilance

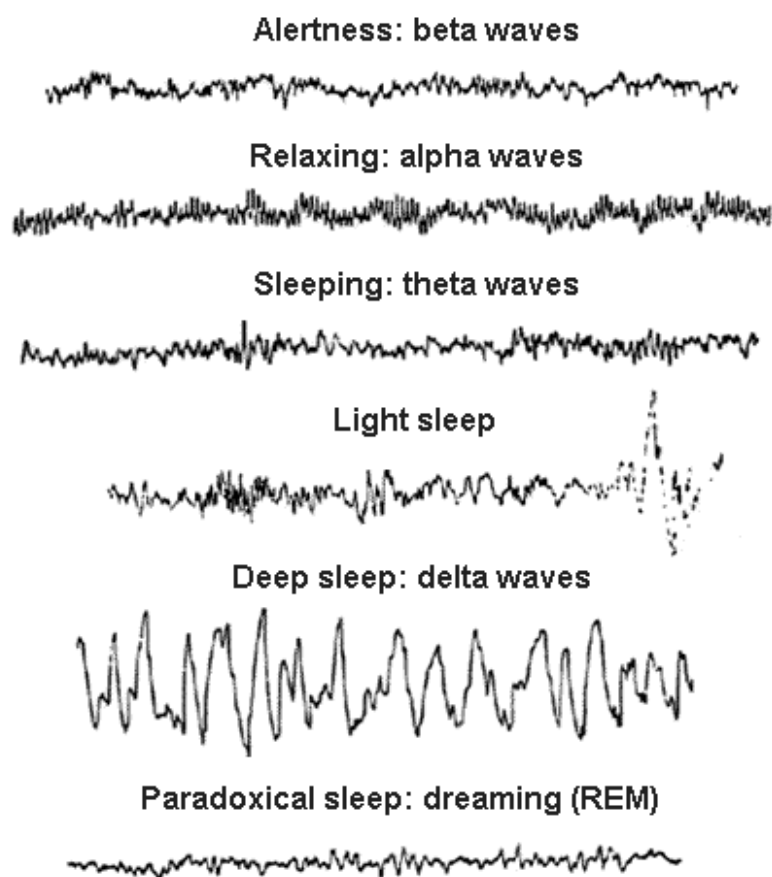


**Figure 1.4** EEG Signals for Various Activities (Sabbatini, 1997)

EEG measures complex neural activities within the fraction of a second. Relative strengths and positions of electrical activity in different brain regions can be determined using EEG.

EEG wave forms are divided into bandwidths and their applications in medical/health are listed below.

**Table 1.2** EEG Band and its applications

<b>Wave</b>	<b>Frequency, Hz</b>	<b>Medical (Normal)</b>
Delta	<4	Sub critical lesions (Adult slow wave sleep)
Theta	4-7	Deep midline disorder (Idling/Drowsiness) Higher in children
Alpha	8-15	Coma (Eyes closed/Relaxed)
Beta	16-31	Benzodiazepines (Mild obsessive, Active Thinking)
Gamma	32+	cognitive decline (Short term memory)
Mu	8-12	Autism

*a) Therapeutic applications of EEG*

EEG is useful for practitioners in the treatment of addiction, migraine, depression, sleep disorders, anxiety, learning disabilities, chronic pain, epilepsy, insomnia, attention deficit hyperactivity disorder (ADHD/ADD), Tourette's Syndrome, etc. (Peter, 2009).

EEG neuro-feedback, which measure brain waves provides a valuable tool for both the therapist and the patient. The patient assumes a much more active and involved role in the process, with the therapist taking one more of the role of educator and coach. Neuro-linguistic programming (NLP) is one example of how the brain codes learning and experience. This can provide skills for development and success in any

area of life, including business, education, training, performing arts, public speaking, etc. The treatment is capable of being time monitored and statistically followed for each patient, which is important for the requirements of managed care organisations ([www.alpha-active.com](http://www.alpha-active.com)).

Hypnosis is a powerful agent in the treatment of many psychosomatic disorders, such as agoraphobia, anxiety states and phobias. The EEG can be used in a pain relief clinic for monitoring patients. It is invaluable to be able to monitor the patients' state of mind to ensure that therapy is effective (Griffiths et al. 2005).

*b) Applications in neuroscience*

EEG monitoring is useful in understanding, treatment and prevention of many neurobehavioral disorders such as head injury, epilepsy, pain syndromes, movement disorders, cerebrovascular disorders, metabolic and neurodegenerative disorders (including age-related), thought disorders, mood disorders, anxiety disorders, personality and substance dependence disorders, chronic stress, Alzheimer's disease, schizophrenia, and many other problems and illnesses. In Cognitive Science Research ([www.alpha-active.com](http://www.alpha-active.com)), the EEG signals can be used in the study of cognitive processes, decision-making, driver alertness, perception of advertising (neuro-economics and neuro-marketing), multi-sensory perception, etc.

*c) EEG in gaming applications*

By developing EEG games controlled by the users' brainwaves directly, users can train themselves to reproduce this mind state when they wish. EEG-driven games are helpful for dynamic mental stress testing, aided learning, in treatment of attention deficit hyperactivity disorder (ADHD), brain training and, for entertainment and fun.

*d) Other applications of EEG*

After the administration of stimulus, neural activity can be recorded within short period, which is an advantage of EEG. EEG is useful determining the relative

strengths and positions of electrical activity in brain (Teplan, 2002). Clinical applications of EEG are listed below.

- To locate areas of damage following head injury, stroke, tumour, etc.
- To test afferent pathways (by evoked potentials)
- To control anaesthesia depth (servo anaesthesia)
- To investigate epilepsy and locate seizure origin
- To test epilepsy drug effects
- To assist in experimental cortical excision of epileptic focus
- To monitor human and animal brain development
- To test drugs for convulsive effects

e) *Electrodes for EEG Measurement*

Biopotential electrodes are used to tap the EEG signal and basically transduce ionic conduction to electronic conduction. Electrodes are metal contacts packaged in such way that they can be easily attached to body.

Basic electrode consists of body and casing, electrode made of high-conductivity material, wire connector, cavity for electrolytic gel and adhesive rim. A layer of an electrolyte gel is used in between metal plate and skin to improve the conductivity.



**Figure 1.5** Cup Electrodes for Measurement of EEG

Nickel–silver alloy, silver, gold and platinum are the materials used as metal electrode. There are suction-type electrodes to make it easy to attach to skin. Figure 1.5 shows typical cup electrode for EEG measurement. Metal disc with conical shape has provision for introducing electrolyte gel or paste from the top of the cone. This is useful when the gel gets dried up. Skin is prepared by abrasion or cleaning and then electrode is placed close to the source being measured.

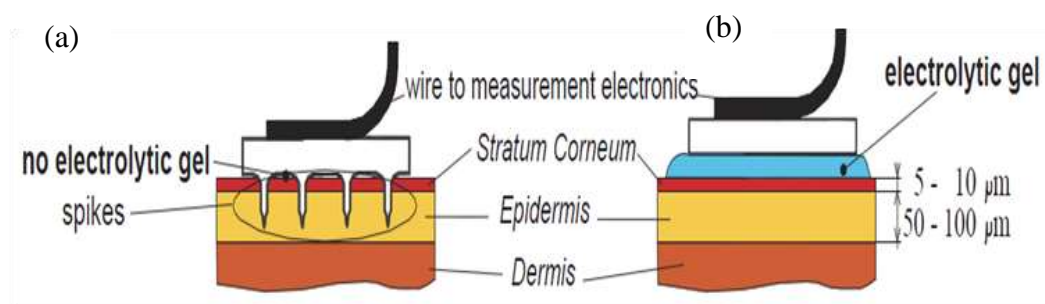


**Figure 1.6** (a) Spiked Electrode (b) Conventional Electrode (Patric Griss, 2002)

To increase the transduction of ionic currents, electrolytic gel is applied between electrode and prepared skin. The top layer of the skin, stratum corneum, is rubbed with abrasive paste to reduce the skin impedance level. Acceptable impedance level for EEG signal acquisition is less than 20 kΩ. With wet electrodes, time required to achieve acceptable value of impedance takes a longer time. Wet electrodes are not suitable for long-term measurement, as the impedance of wet electrodes deteriorate from 5 to 15 kΩ within five hours after gel application (Lopez - Gordo et al., 2014). Wet electrodes and dry electrodes are compared and details given in the table 1.3

To record an accurate EEG signal, the contact impedance value should be between 1 to 10 kΩ (Ali Bulent, 2009). If it is less than 1 kΩ, then there may be short circuit between electrodes and if the impedance value is greater than 10 kΩ, then it would give distorting artefacts.

Microneedles cause less damage to the tissue due to smaller dimensions of the needles (Boehm et al., 2011).

**Table 1.3** Spiked Electrodes vs. Conventional Electrode

<b>SL. No.</b>	<b>Spiked Electrode</b>	<b>Conventional Electrode</b>
1.	No need for skin preparation	Need for skin preparation
2.	Can stick to skin for longer time	Can't stick to skin for longer time
3.	Lesser impedance	Higher impedance
4.	High signal acquisition	Weak signal acquisition
5.	Low electrical noise level	High electrical noise level
6.	Maximum comfort for subject	Minimum comfort for subject

#### **1.4 RESEARCH HYPOTHESIS AND OBJECTIVES**

The basis for using micro-electrode is framed on the supposition that the electrodes penetrate the impedance-causing stratum corneum and are directly in contact with sub dermis. The electrodes are aimed to be used in dry condition without usage of any conductive gel and without any need for skin preparation. Array of micro-electrodes are not expected to reach dermis where nerves presence would cause pain. Dry electrodes are aimed at acquisition of EEG signals for long duration compared. Penetration of array of micro-electrodes into the skin is aimed at keeping electrodes to be in contact with living cells in sub dermis without causing motion artefacts to the acquired signals. From the point of biocompatibility to human skin and method of fabrication, polymer material is considered as the material for fabrication of microneedle based electrode.

The major objective is to design and fabricate biocompatible microneedles that can be used to acquire EEG signals continuously for longer duration. To achieve this, the following objectives are set:

- Study on polymer material suitable for microneedles
- Design and analysis of micro-array needle array
- Fabrication, testing and characterisation of biocompatible microneedle array

## **Organisation of Thesis**

**Chapter 1** provides introduction to micro needle based dry electrode and compares it with traditionally used wet electrode for EEG measurement. This chapter deals with skin anatomy, bio-potential signals and EEG signals for various activities. Research hypothesis and objectives are detailed in this chapter.

**Chapter 2** deals with the material aspects of microneedle. Various materials used for biopotential signal acquisition are reviewed. Comparison of metallic microneedle and polymeric microneedle is dealt. Advantages of selecting polymer material for microneedle based electrodes are detailed. This chapter explains the various techniques and methods used for fabrication of microneedle-based electrodes.

**Chapter 3** describes the design aspects and analysis of microneedle. Analytical design and FEM analysis carried out have been illustrated. FEM analysis has been carried out with the objective of optimising the microneedle parameters for minimum strain of needle and maximum penetration.

**Chapter 4** deals with the experimentation to fabricate microneedle by MSL, micromachining and micro moulding, and directly by micromachining. Experiments conducted for conductive coating have been explained. This chapter explains the mechanical characterisation of microneedle fabricated. Compression test, shear test, penetration test, adhesiveness test and other test for conductivity have been dealt in this chapter.

**Chapter 5** discusses the results of the testing and characterisation performed with respect to:

- MSL process for fabrication of HDDA microneedle
- Limitation of MSL process for processing of microneedle using PMMA materials
- Experimentation of fabrication of micro mould using polydimethylsiloxane (PDMS)
- Direct micromachining of microneedles

- Compression and shear test of microneedle and penetration of microneedle over skin
- Adhesion test of conductive coating
- Conductivity of microneedle for biopotential measurement

**Chapter 6** brings together overall summary of outcome of the research work carried out. The thesis concludes with limitations of the current work and suggestions for future investigation.



## CHAPTER 2

### LITERATURE SURVEY

#### 2.1 INTRODUCTION

This section describes the principles and practices developed and adopted by various researchers and scientists in fabrication, testing and characterisation of microneedles. Here, theoretical and experimental investigations conducted in fabrication of micro needles through various processes have been reported. An overview of the material combinations and fabrications methods used for processing various materials respective to their chemical properties and processing method is also presented. The increasing use of polymers by various researchers and scientists in order to have biocompatible polymers is of prime area for research and is reported here.

#### 2.2 MICRONEEDLE FABRICATION, TESTING AND CHARACTERISATION

Patrick et al. (2002) investigated on micro-fabrication, packaging and testing of a micro machined dry biopotential electrode.

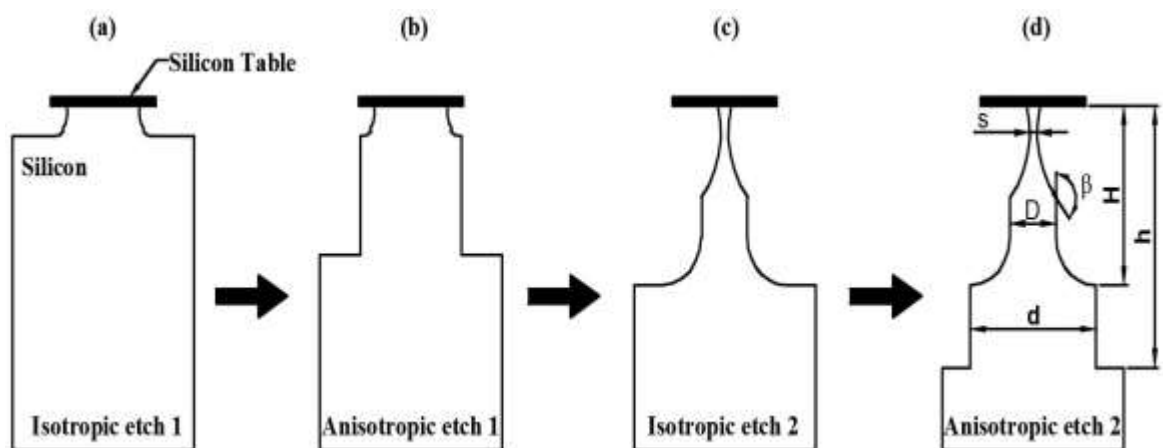


**Figure 2.1** Combination of Isotropic and Anisotropic Etching Process for Out-of-Plane Fabrication of Microneedle (Patric et al., 2002)

The electrode consists of an array of micro-dimensioned, very sharp spikes designed for penetration of human skin circumventing high impedance problems associated with layers of the outer skin. The spikes were etched in silicon by deep reactive ion etching as shown in Figure 2.1 and were subsequently coated with silver chloride double layer.

Observations made by the authors show that low amplitude biopotential from the activity of the brain resulted in EEG signals of high quality. Thus, spiked electrodes allowed a high quality recording of low-level biopotentials. Also, the insertion and removal from the skin was fast and uncomplicated. The spiked silicon electrodes are compared with conventional electrodes and it is stated that the EEG signals are similar. Inference is that spiked electrodes are convenient to use and are comfortable. Hence, the spiked electrode offers a promising alternative to standard electrodes in biomedical applications and is of interest in research of new biomedical methods. However, silicon is neither bio compatible nor bio-stable (Wang et al., 2005). There is a disadvantage in using silicon materials, as it will break during usage.

Luttge et al. (2008) presented the work on microneedle array electrodes for EEG monitoring. A new replication process for numerous types of microneedles arrays was done. Polymer microneedle array electrodes with 64 microneedles in nested 4×4 arrays were positioned on circular disc of 100 μm. Photolithography fabrication was carried through prepared silica hard moulds using photoresist SU-8. The Processes involved for making electrodes are lengthy as it comprises of Photo Lithography, Deep Reactive Ion Etching (DRIE), Hard Lithography and Soft Lithography. Also, proprietary bio compatible plastic material Hysol® had been used to make microneedles. Electrical characterisation of micro needle showed a value of 150 kΩ and it had improved many times when gel was used along with it. These electrodes were certified for EEG measurement. The Ag-coated microneedle array electrodes show excellent signal-to-noise ratios.

A novel micro machined physiological recording electrode with hollow microneedles for ECG measurement was studied by Yu et al. (2008). In comparison with conventional electrode, a unique characteristic of this device was that a hollow

microneedle array was made of silicon, which could pierce through the outer skin surface; fabrication of microneedles of these was done by etching and the formation of back reservoir. The silicon die was fabricated at wafer level using three-SiO<sub>2</sub>-mask and three-step Deep Reactive Ion Etching (DRIE) process. Figure 2.2 shows hollow microneedles with reservoir. This invention was used for ECG measurement.

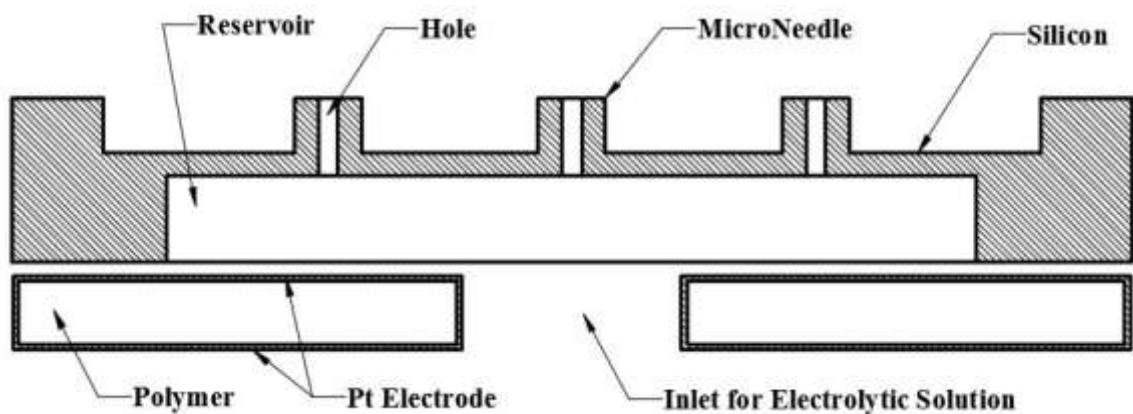


**Figure 2.2** Hollow Microneedles With Reservoir (for Filling NaCl) for ECG Measurement (Yu et al., 2008)

The electrolytic solution stored in the backside reservoir provides direct electric connection between outside electrodes and inner skin layer. This minimised the high signals from skin layer and resulted in a good signal-to-noise ratio. The study compared the ECG signals measured using hollow microneedles and standard wet electrodes. It is reported that the hollow micro needles compare well with the commercially available wet electrodes. Combined with wireless communication, a portable ECG recording system with micro-fabricated bio-electrodes makes it a potential long-term and repetitive ECG measurement for out-of-hospital diagnosis, especially for health-care management of aged people living alone at home.

Yu Mike Ch (2010) described wireless, mobile-based health-care devices having significant interest towards developing alternative biopotential electrodes for patient physiological monitoring. The conventional wet adhesive Ag/AgCl electrodes used universally in clinical applications today provide an excellent signal, but are cumbersome and irritating for mobile use. While electrodes that operate without gels,

adhesives and even skin contact have been known for many decades. However, they are yet to achieve acceptance for medical use. In this paper, the author explored the use of dry/non-contact electrodes for clinical use by explaining the electrical models for dry, insulated and non-contact electrodes and show the performance limits, along with measured data. The theory and experimental data showed that the common practice of minimising electrode resistance might not always be necessary and actually led to increased noise depending on coupling capacitance. Theoretical analysis was followed by an extensive review of the latest dry electrode developments in the literature. The paper concluded with highlighting some of the novel systems that dry electrode technology had enabled for cardiac and neural monitoring. Salvo et al. (2012) presented the design, fabrication and testing of 3D-printed dry electrode. The electrode consisted of a conical support (0.5 mm height, base diameter 15 mm, top base diameter 13 mm) on which an array of conical needles was placed.



**Figure 2.3** 3D-Printed Microneedle Made Out of Biocompatible Acrylic-Based Resin (Full Cure® 720), Salvo et al. (2012)

Each needle was about 3 mm high, 600  $\mu\text{m}$  base diameter and 100  $\mu\text{m}$  tip diameter. The array consisted of 180 conical needles (distance = 250  $\mu\text{m}$ ) on a truncated conical base. The metallisation process underwent two steps sputtering of titanium as adhesion promotion layer and evaporation of gold to lower the impedance and prevent oxidation of the electrode. After electrode characterisation, experimental results were presented and compared with planar wet Ag/AgCl electrodes for recording ECG–EEG. Performance of coating was tested using scotch tape test and it is reported that there was no pulling off of coating. This study is found to be useful for conductive

coating of polymers. The needles were tested using 32 channel impedance analyser. Test results showed impedance value less than  $10\text{ k}\Omega$  for 3d printed dry electrodes. The measured impedance values are less and the electrodes are suitable for EEG measurement. The developed dry electrodes were reported to be suitable as valid sensors for ECG and EEG recording.

Vanlerberghe et al. (2011) studied the design and fabrication of a novel two-scale topography dry electrode using macro-and microneedles. The macro needles enabled biopotential measurements on hairy skin.

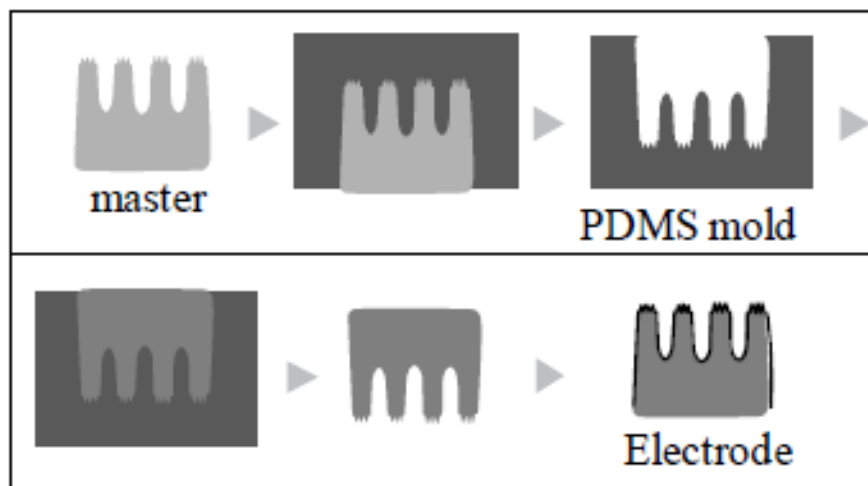


**Figure 2.4** Steps Involved in Microneedle Fabrication (Vanlerberghe et al., 2011)

Also, it was described how micro-precision milling and inexpensive moulding steps were used to create a two-scale dry electrode (Figure 2.5) in a cost-effective way.

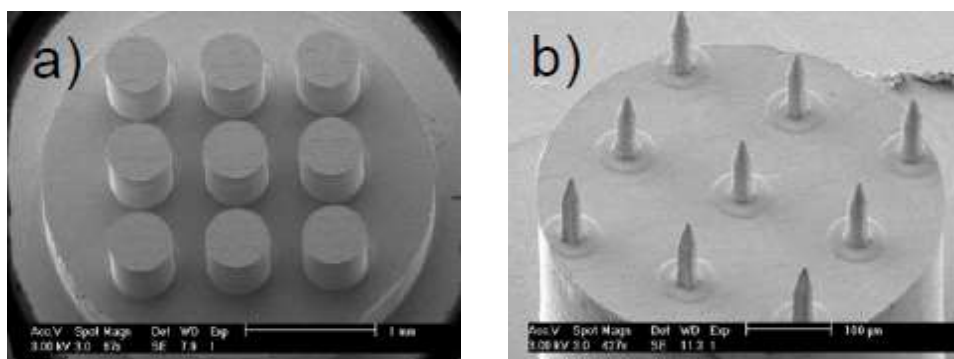


**Figure 2.5** (a) and (b) 2 Scale Topography of Microneedle Fabricated by Vacuum Casting Technology (Vanlerberghe et al., 2011)

Initially, aluminium master mould was fabricated using CNC milling and then silicone rubber (PDMS) was vacuum moulded out from it as shown in Figure 2.4. Silicone mould was used to make SU-8 microneedle structure. Ag/AgCl was done to obtain a conductive layer for signal transmission. Further, a fast and accurate impedance measuring protocol was developed to compare and evaluate the contact impedance of various types of electrodes. The research work showed comparison of different conductive coatings (Ag/AgCl/Au). AgCl is found to be slightly better than Ag as coating material, and Au-coated electrodes have the highest impedance. Also, a fast and reliable impedance characterisation protocol was described. Based on this impedance measurement, promising results were obtained with the fabricated electrodes.

Seong et al. (2010) designed and fabricated PMMA microneedle array with electrical functionality with the final goal of electroporating skin's epidermal cells to increase their transfection by DNA vaccines.

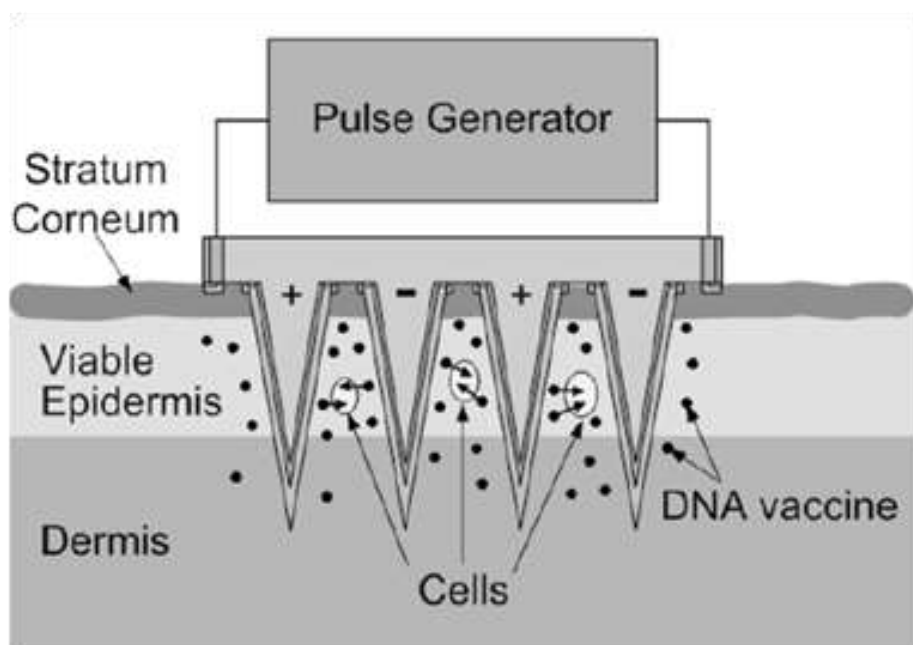


**Figure 2.6** Scheme of Electrically Activated Microneedle Array for DNA Vaccination (Seong et al., 2010)

Fabrication process of microneedle array was made of PMMA by micromolding technology from a master PDMS mould, followed by metal deposition, patterning using laser ablation and electro deposition. Microneedle electrode arrays were strong enough to insert into the skin. Additional experiments with red blood cells and human prostate cancer cells showed that these microneedle electrodes were electrically active and capable of electroporating cells with high efficiency. In this research work, PMMA was chosen as micro needle material citing the reason it has been safely used in medical devices approved by U.S. Food and Drug Administration (FDA). In this study PMMA micro needles have not been used for EEG signal acquisition, however, it was found that the micro needles were able penetrate human skin for electroporation. The research work supports the use of PMMA as material for micro needle.

Patric (2002) studied the characterisation of dry spiked biopotential electrodes and suitability test to be used in anaesthesia monitoring systems based on the measurement of electroencephalographic signals. The spiked electrodes consist of a micromachined chip containing an array of silver or silver chloride-coated microneedles glued onto a carrier. The assembly of the electrode was altered to simplify production, that is, the carrier used consists of a circular double-sided printed circuit board and the lead wire is soldered to the carrier. Biopotential electrodes that were applied onto the forehead dry spiked electrodes had the potential to be used as sensors recording EEG for anaesthesia monitoring.

James (2006) gave details about preliminary data that suggested safety concerns were surmountable due to relatively minor and transient abrasions that were created in skin and the impressive regenerative capacity of the tissue. However, the kinetics and mechanisms of skin healing in response to these assaults on skin integrity were not completely defined.

Miyako (2015) studied about fabrication of SU-8 based polymer microneedle for recording brain activities. SU-8 polymer microneedle was replicated from PDMS mould made using SU-8 mould fabricated using lithography process. Nano-porous parylene was deposited over silver-coated needles to avoid peeling off of silver. The

researchers developed 20×20 polymer microneedles with needle height of 230 μm and a tip curvature radius of 17 μm.

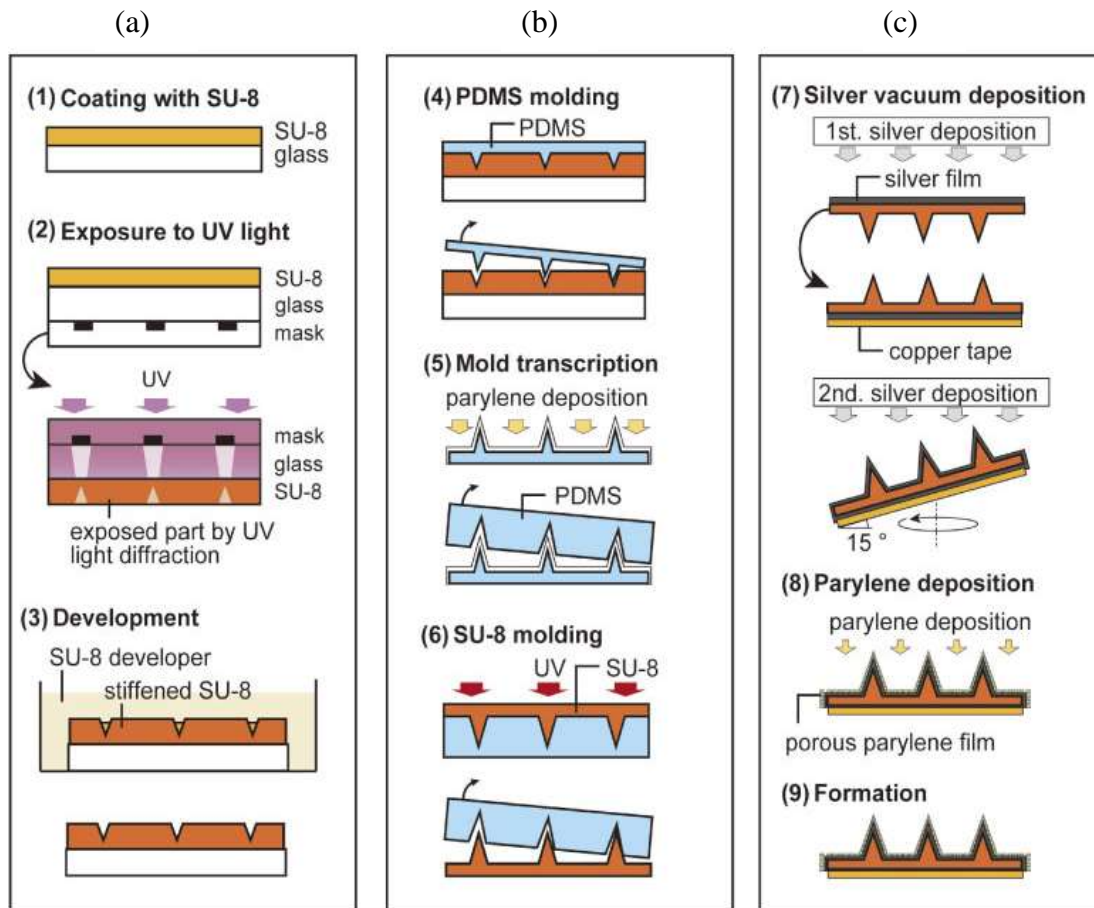


**Figure 2.7** a) Fabrication of SU-8 Micromould, b) Fabrication SU-8 Microneedle c) Formation of Microneedle Electrode (Miyako Arai et al., 2015)

Contact impedance value of less than 10 KΩ was measured, and it was found to be comparable to the impedance value of wet electrode. Micro needles were tested for EEG signal acquisition for 3 hours. Low impedance value observed shows the effectiveness of microneedles for longer duration.

Teplan (2002) reviewed the fundamentals of EEG signal and acquisition. Classification of brain waves like beta (>13 Hz), alpha (8-13 Hz), theta (4-8 Hz) and delta (0.5-4 Hz) with respect to frequency was described. EEG recording technique

using various electrodes, amplifier with filters, A/D converter and recording device were explained in the review. 10-20 electrode placement system for EEG signal acquisition was described.

Priyanka et al. (2004) studied the design of microneedles for medical applications. Skin resistance was taken into account while designing the microneedles.

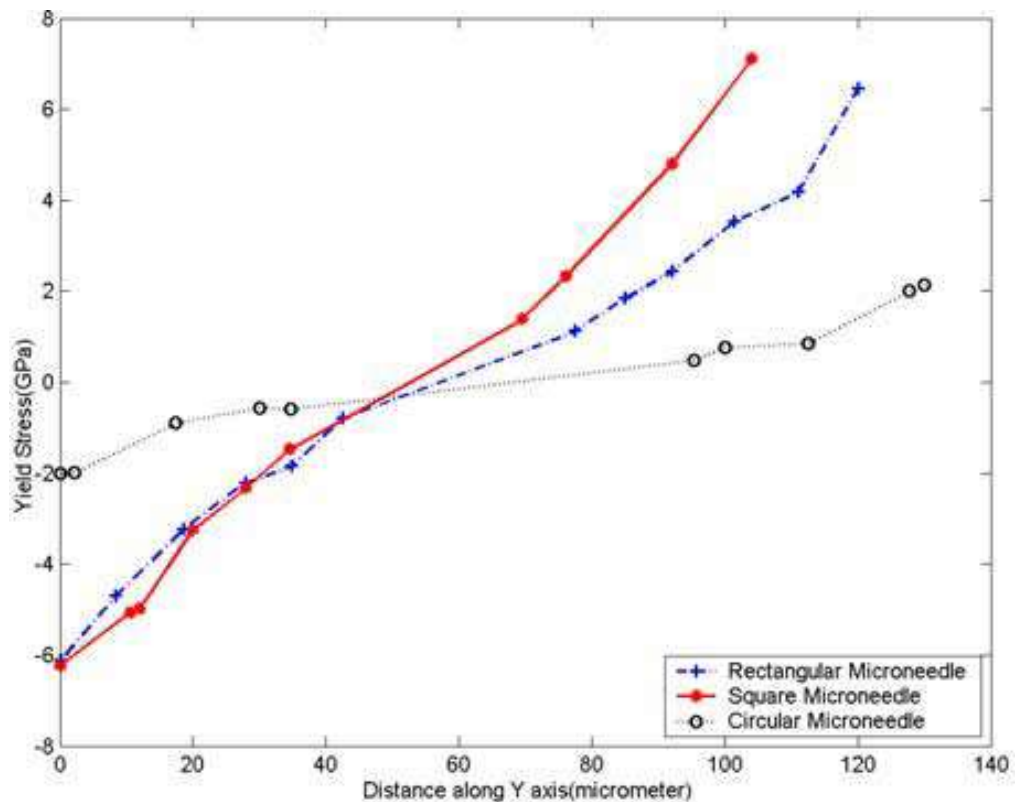


**Figure 2.8** Yield Stress Values of Different Configurations (Rectangular, Square and Circular) of Microneedles (Priyanka et al., 2004)

Various cross-sections of microneedles were analysed from the mechanical strength point of view, and it was concluded that circular cross-section preferred over square and rectangular cross-sections for in-plane micro needles. Ramasubramanian et al. (2008) analysed the mechanism of fascicle insertion into the skin by mosquito. Analytical and mathematical modelling was compared with experimental data obtained from a high-speed camera.

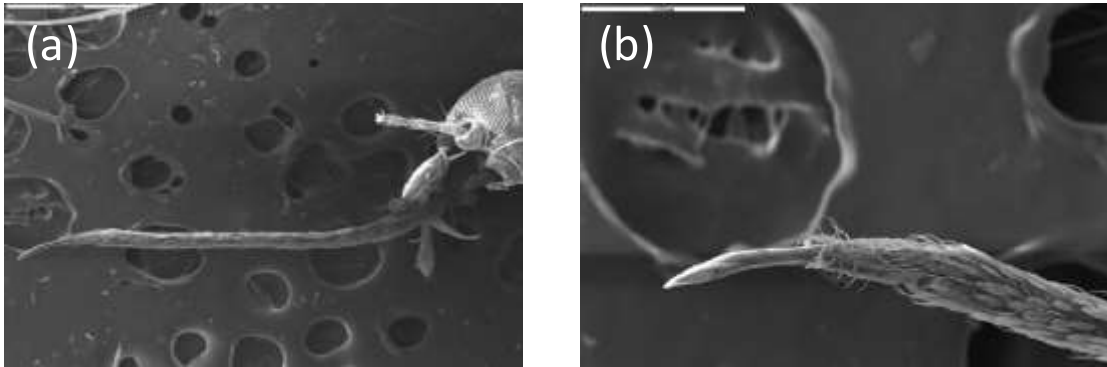


**Figure 2.9** a) Mosquito Head and Proboscis b) Fascicle Tip with Labella Retracted (Ramasubramanian et al., 2008)

Results show that the lateral support of the fascicle provided by labium avoids buckling of the fascicles. The lowest force of 10 mN has been estimated for sharp microneedle. It was observed that the mosquito moves its head back and forth, at a frequency starting from 15-17 Hz and gradually reducing to about 6 Hz during the insertion process. The critical buckling load for a typical fascicle is very low ( $\sim 3$  mN) and not sufficient to penetrate the skin. This study reveals the fact that the human skin can be easily penetrated by a tiny fascicle tip with very low force.

Nahe Mane et al. (2013) analysed microneedle design for drug delivery using COMSOL. Silicon as material for hollow microneedle was considered for analysis.

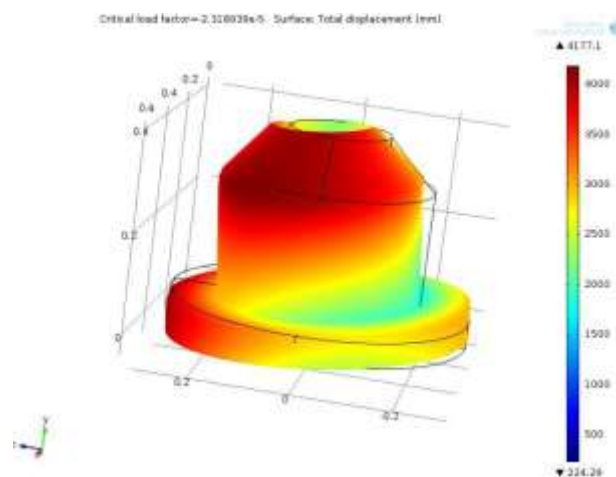


**Figure 2.10** Stress Analysis (Nahe Mane et al., 2013)

Analysis showed that needle can withstand a pressure of more than 3.18 MPa. This is the pressure required to puncture the skin. Maximum buckling force of microneedle was found to be more than the resistance force in the microneedle. Breaking of needles was not reported.

Ashraf et al. (2010) used FAE to determine the mechanical forces exerted on the skin during the insertion of silicon microneedle in transdermal drug delivery applications. Authors studied the effect of compressive force and transverse force. Results showed that the yield strength of the material was much higher than the force required to penetrating the skin.

Groves et al. (2013) modelled the human skin in FEA and described that the needle penetration was having non-linear stress–strain relationship.

It was described that the skin exhibits anisotropic, non-linear and viscoelastic properties. FEA results were compared with indentation tests on the skin. Figure 2.11 shows the FEM analysis of indentation of skin.

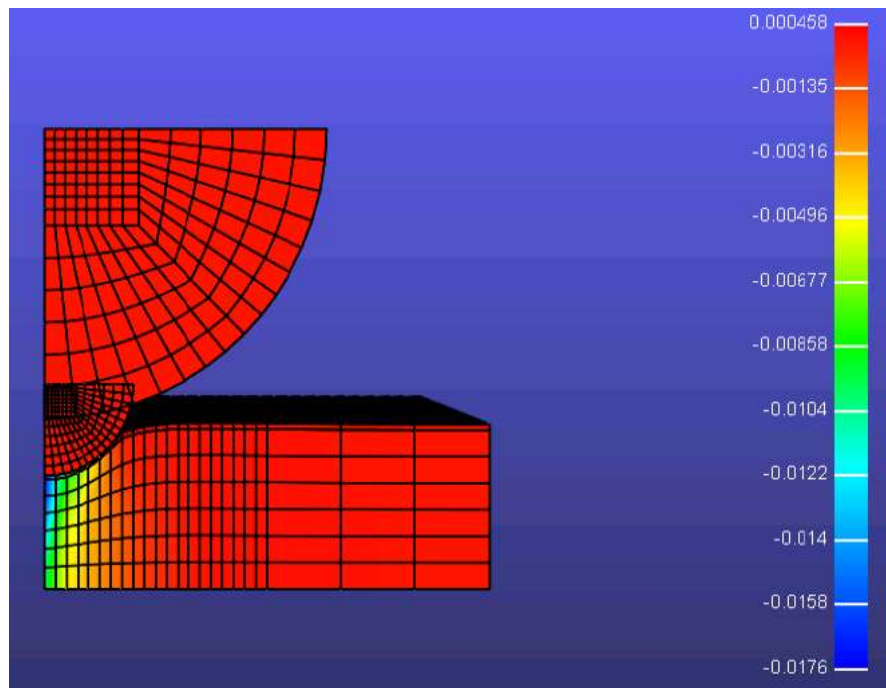
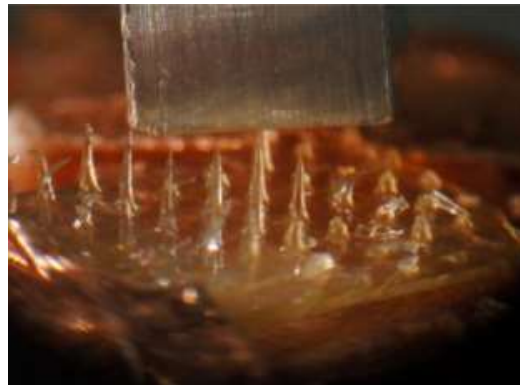


**Figure 2.11** FEM Analysis of Indentation of Skin (Groves et al., 2013)

(a)



(b)

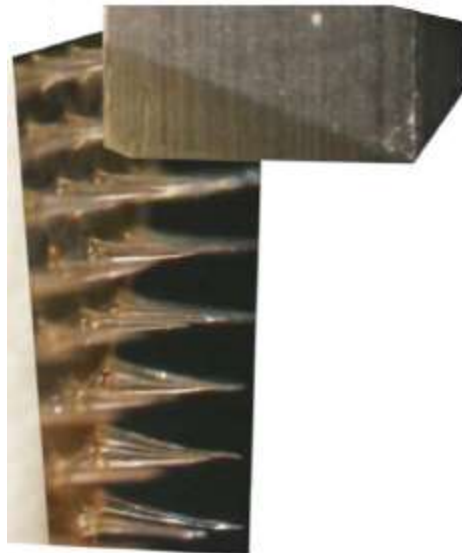


**Figure 2.12** (a) Axial Fracture Force Measurement (b) Transverse Shear Force Measurement (Yusuf et al., 2013)

Yusuf et al. (2013) tested the polymer microneedles using micromechanical tester (Instron H Model 5969, Instron, Norwood, MA). A single microneedle was forced into the metal mill at 500 mm/sec in each test. Figure 2.12 (a) and (b) shows loading on microneedle in axial direction and transverse direction. The mill and microneedle were aligned using a microscope camera. Needle failure force was determined as the point just before sudden decrease of force during the application of axial load and transverse load. Figure 2.13 (a) to (d) shows deformation of the microneedle when axial load and transverse loads are applied on microneedles made of Sodium Alginate

(PA) and Poly Lactic-co-Glycolic Acid (PLGA). Table 2.1 lists the force at which the microneedles failed due to axial and transverse load.

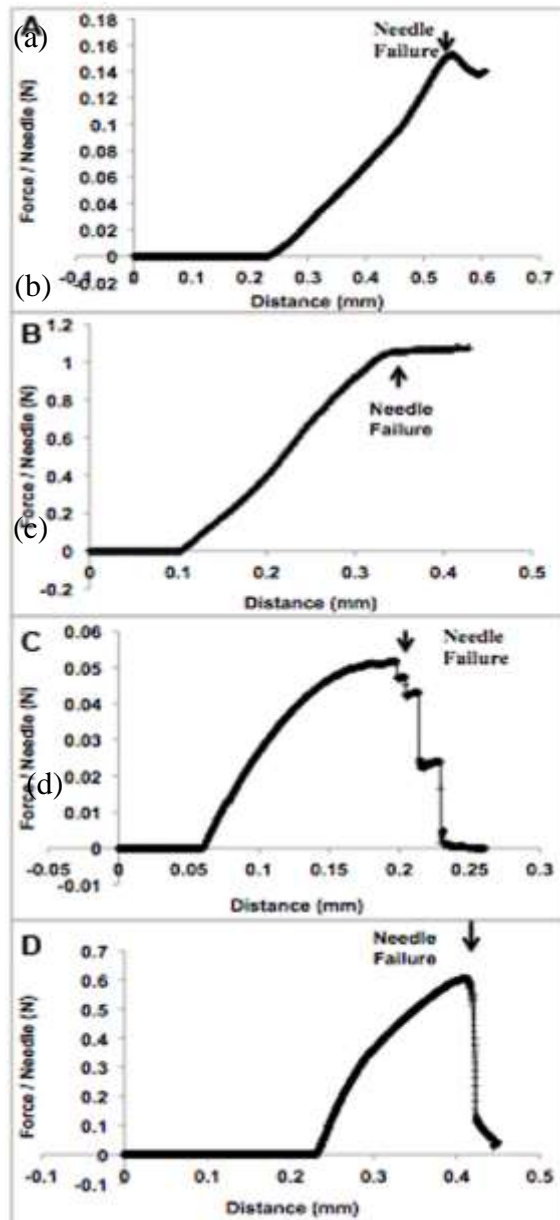


**Figure 2.13** (a) Mechanical Analysis of SA MNs Under Axial Loading. (b) Mechanical Analysis of Polymeric PLGA MNs under Axial Loading. (c) Mechanical Analysis of Polymeric 10% (w/w) SA MNs under Transverse Loading. (d) Mechanical Analysis of Polymeric PLGA (Yusuf et al., 2013).

**Table 2.1** Fracture Failure Values of Polymers due to Axial and Transverse Forces

Test Type	MN Type	Force/Needle (N)
Axial failure	PLGA	1.06±0.02
	SA (Sodium alginate)	0.18±0.05
Transverse failure	PLGA	0.46±0.04
	SA	0.04±0.02

For failure to occur, PLGA MNs required a force of 1.06 N/needle under axial loading, whereas the force acting on the needle was 0.18 N/needle. It is therefore concluded that the fracture force of PLGA MNs was approximately five times greater than that of SA MNs. Similarly, fracture force required in transverse for PLGA was more than 10 times in the case of PLGA compared with SA.

Davis et al. (2004) studied the effect of microneedle fracture force with respect to the tip radius and force of insertion with respect to microneedle interfacial area.

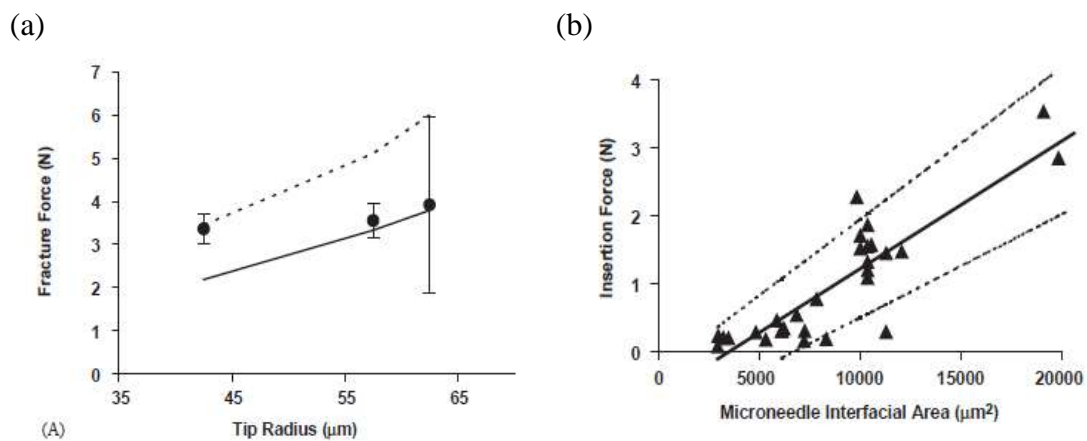


**Figure 2.14** (a) Fracture Force vs. Microneedle Interfacial Area  
 (b) Insertion Force vs. Microneedle Interfacial Area (Davis et al., 2013).

Figure 2.14 (a) shows analytical values and experimental values of fracture force on increase of tip radius. As the tip radius increased, a marginal increase in fracture force was observed. Figure 2.14 (b) shows the experimental values with 95% confidence

limits marked in dotted lines. Increase in microneedle surface area necessitated the need for higher insertion force.

Khanna et al. (2010) quantified the fracture limits of axial and radial forces of silicon microneedle. Figure 2.15 (a) shows the set up for applying axial and radial force.

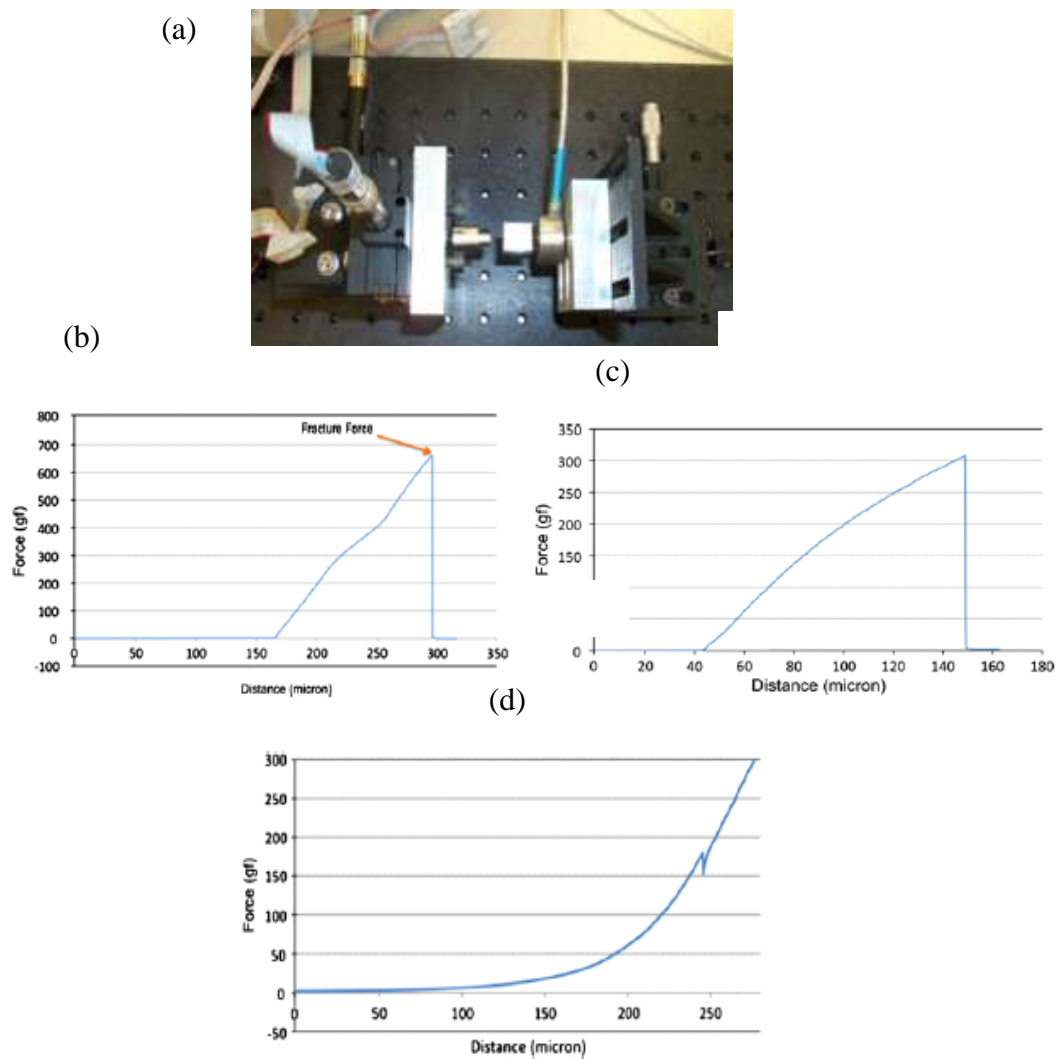


**Figure 2.15** (a) Experimental Setup for Testing Axial Fracture Force, Shear Force and Skin Insertion Force (b) Plot of Axial Force vs. Needle Deformation (c) Plot of Shear Force vs. Needle Deformation (d) Applied Force on Skin vs. deformation of Microneedle (Khanna et al., 2010)

Custom-built Lab View programme was used to control the actuators. The setup also consisted of facilities for video capturing and imaging through high-resolution camera. Figure 2.15 (a) reveals that the axial fracture force at which the microneedle failed is about 740 gram-force (7.25 N) and Figure 2.15 (b) shows the shear force required for fracture due to shear load was about 300 gram-force (2.94 N). Figure 2.15 (d) reveals the force required to penetrate the skin is much less than the fracture force of the silicon microneedle.

Literature on various processes used for microneedle fabrication and features of it are listed in Table 2.2.

**Table 2.2** Processes Used for Micro-needle Fabrication and Its Features

<b>Team/Year</b>	<b>Process</b>	<b>Special Feature</b>	<b>Remarks</b>
Park et al. (2004)	MEMS masking and etching, vacuum-based PDMS mould	BD polymer	
Kabseog Kim et al. (2004)	MEMS-based process Spin coating of SU-8 UV exposure, Ni electroplating, planarising SU-8, polishing, removal of SU-8	SU-8 is used for fabrication	Hollow metallic microneedle
Park et al. (2007)	Photo lithography technique is used. SU-8 master mould is made by integrated lens technique.	Master Mold: SU-8 Mold: PDMS Micro needle materials: PLA/PLGA/PGA	PDMS mold is used about 100 times. Micro needles are meant for transdermal drug delivery.

<b>Team/Year</b>	<b>Process</b>	<b>Special Feature</b>	<b>Remarks</b>
Wang et al. (2008)	LIGA-like technique used	Biodegradable PLA is used as moulding material	Micro-injection method is used for molding microneedles
Seong – O Choi et al. (2009)	PMMA-micro moulding forms PDMS Metal deposition Patterning using laser and electro deposition	PMMA	First MEMS fabricated MN for DNA vaccine delivery for electroporation
Shaun et al. (2009)	2 photon polymerisation and micromolding Solid microneedle arrays, fabricated by means of 2PP, were used to create negative moulds from PDMS.	Using these moulds, microneedle arrays were prepared by moulding, eShell 200, a photo-reactive acrylate-based polymer	Polymer exhibits water and perspiration resistance
Chu et al. (2010)	Localising of more drug at the tip	Dissolving polymer microneedle matrix, drug encapsulation Model drug used: Sulfothodamine B	
Fiedler et al. (2010)	Standard titanium pins with interconnections have been used		Electrode of Ø1.5 mm has been used. TiN coating produced excellent

			electrochemical characteristics. EEG signal quality has been compared with Ag/AgCl electrode and quality of signal is adequate.
Ashraf et al. (2010)	MEMS-based DRIE Isotropic and anisotropic etching (ICP)	Piezo electrically actuated micro-pump Effect of voltage and frequency on silicon membrane deflection and flow rate were studied	Silicon hollow Microneedle with integrated pump
Donnelly et al. (2010)	Optical coherence tomography is used to study the effects of microneedle geometry on skin penetration.	Piercing force versus depth of penetration studied	Polymeric microneedle 520 $\mu\text{m}$
Daudimont et al. (2010)	Micro-array needle was used with electric pulse and vibratory assistance to disrupt stratum corneum	Association of microneedles with electric pulses for electroporation	Hollow microneedle limitation for DNA electro transfer
Lyle Hood et al. (2011)	Design analysis silica tubing for microneedles	150 diameter of silicon tube showed laminar flow	Diameter 100 $\mu\text{m}$

Boehm et al. (2011)	Light dynamic Mask MSL, Micromolding and ink jet printing	Biodegradable polymer Wide range of pharmacologic agent compositions Microneedles with quantum dot	Imaging of quantum dot by multi-photon microscopy
Ashraf et al. (2011)	MEMS-based micro-pump and microneedles	Micro-pumps and Microneedles	Overview on micro-pumps and microneedles
Donnelly, 2011	Micromoulding microneedles	Laser-based micro mould preparation OCT study of piercing	Polymeric microneedle 600 and 900 $\mu\text{m}$ ht.
Prasanna Gandhi et al. (2011)	Bulk lithography technique is used. Step-less process	Step-less feature Fast	Polymer microneedle has not been tried
Shaun D et al. (2011)	MSL-based process Fabrication of BD polymer by visible light and dynamic mask lithography Silver coating using pulsed laser	Microneedle dimensions: height: 748 to 828 $\mu\text{m}$ . Width: 517 to 805 $\mu\text{m}$ . Depth: 311 to 347 $\mu\text{m}$ .	Silver coating used for antimicrobial therapy
Choi SO et al. (2012)	Micromoulding by metal transfer	Electroporation	Electroporation improves uptake of molecules
Miyako Arai et al. (2015)	Micromoulding	Mould material: PDMS	Meant for EEG measurement.

		Needle material: SU-8	Deposited with silver in vacuum and parylene film. Used artificial skin (urethane elastomer) for testing
--	--	--------------------------	--

**Table 2.3** Comparison of Micro-needles Developed by Various Researchers

<b>Team</b>	<b>Material</b>	<b>Process</b>	<b>Needle size</b>	<b>Impedance value</b>	<b>Coating</b>
Patric et al. (2002)	Silicon	MEMS/dry etching	Ht: 160 $\mu\text{m}$ Q: 40 $\mu\text{m}$	-	Ag/AgCl
Wilke et al. (2005)	Silicon	Wet Etching	Ht: 300 $\mu\text{m}$	-	Gold
Lutege et al. (2008)	SU-8	Photo lithography	Ht: 320 $\mu\text{m}$ Q: 100 $\mu\text{m}$	150 $\text{k}\Omega$	Ag
Lin et al. (2011)	Foam + Cu layer	-	14 mm $\times$ 8 mm $\times$ 8 mm	4-12 $\text{k}\Omega$ Impedance	Cu Foil
Lun-De Liao et al. (2011)	Beryllium copper	Turning, Coating	Dia.>0.5 mm 17elect rodes	10 $\text{k}\Omega$ Impedance	Gold
Vanlerberghe et al. (2011)	SU 8	Vacuum moulding	-	-	Ag/AgCl
Salvo et al. (2012)	Acrylic-based polymer	3D printing	Ht.: 3 mm Dia.: 600 $\mu\text{m}$ Tip dia.: 100 $\mu\text{m}$	-	Titanium & gold
Miyako et al. (2015)	SU 8	Moulding/lithography	Ht.: 230 $\mu\text{m}$ Tip dia.: 17 $\mu\text{m}$	6 $\text{k}\Omega$ Impedance	Parylene /silicon

### 2.3 MATERIALS FOR MICRONEEDLE

Materials for microneedles are required to have mechanical strength to penetrate the skin and are required to be biocompatible. Metals and silicon have enough strength to penetrate. Not all polymers have the required strength and are biocompatible. Metal and silicon needles are brittle, and there is a possibility of breaking off while inserting into the skin. Polymers are emerging as alternative material. Failure forces for polymer microneedle are much more than the forces required for penetrating the skin. Biodegradable polymers have required mechanical properties as the needles penetrate into the skin and remain in the skin for a longer time. Hence, biocompatibility is an important factor in selecting the material for microneedles.

**Tungsten** was studied for its high mechanical properties. However, it has long-term effect to health (Laurence Knott, 2014). Stainless steel being corrosion resistant, biocompatible, highly stiff and easily electrochemically coated was considered to be a suitable material ([www.microprobes.com](http://www.microprobes.com)). Pure iridium has by far the lowest tip impedance. Also, it is found to be inert and very resistant to corrosion. Surface can be easily activated to increase the charge by electrochemical cyclic voltammetry ([www.microprobes.com](http://www.microprobes.com)).

**Stainless steel** has properties like high corrosion resistance, good formability and strength; it finds application in medical industry where manufacturing precision, reliability and hygiene are important (Nitish et al., 2000). Stainless steel (SS316/316L) is used in medical industry, as it does not corrode and stain. It has antibacterial properties and non-magnetic. In medical industry, stainless steel is used as temporary implant. Some of the medical applications of stainless steel including medical needles are precision stainless steel tubing, orthopaedic implants (predominantly 316/316L), artificial heart valves (predominantly 316/316L), bone fixation, mandrels/tools, chemical containers/hazardous waste containers, wires, wire coils, wire forms, speciality guide wires, currettes, screws/prostheses/plates, medical needles, medical syringes, sensor probes, catheters, otolaryngology ear scope nozzles, sinks/bowls/surfaces/trays/knives. Stainless steel is among the difficult to machine

materials. It has poor machinability because it is tougher and tend to work harden rapidly.

**Titanium** is a biomaterial. In medical industry, titanium and its alloy are used as bioimplants. Typical implants include hip joint, knee joints, bone plates, dental implants, screws, pacemakers and artificial hearts. Elias et al. (2008) had listed the important biocompatible properties as low level of electronic conductivity, high corrosion resistance. Dielectric properties of titanium are comparable to water. Titanium material is used as dental implants, cardiovascular devices, external prostheses and surgical instruments. Weight of the titanium is about 56% of steel, and strength is equivalent to steel. Titanium is poor conductor of electricity and heat (www.totalmateria.com). Titanium is considered as difficult machine material due to its high strength, low thermal conductivity and chemical reactivity with tool materials. Also, due to its low young's modulus of elasticity, spring back happens. This results in poor surface quality on the finished part. It will be much more challenging to machine micro features on titanium.

**Silicon**, a semiconductor material, is widely used in electronic industry due to its physical and chemical properties. Silicon allows fabrication of precise features using micro-fabrication process. Technology for fabrication micro-features using silicon is sophisticated, well established and is used for production of devices in mass in semiconductor industry. The cost of the device is low due to production of parts in volume. Silicon is neither biocompatible nor biostable (Anfenget et al., 2005). Use of porous silicon for biomedical application is being researched. Research study on porous silicon-based biomaterials for bone tissue engineering was carried out by Wei Sun et al. (2007). Wei Sun had concluded that porous silicon is a strong candidate for bone tissue engineering.



**Figure 2.16** 400  $\mu\text{m}$  Tall Silicon Microneedles (www.tyndall.ie)

Tyndall National Institute, Ireland, had developed silicon-based microneedles (Figure 2.16) for drug delivery as well as for EEG and ECG monitoring ([www.tyndall.ie](http://www.tyndall.ie)).

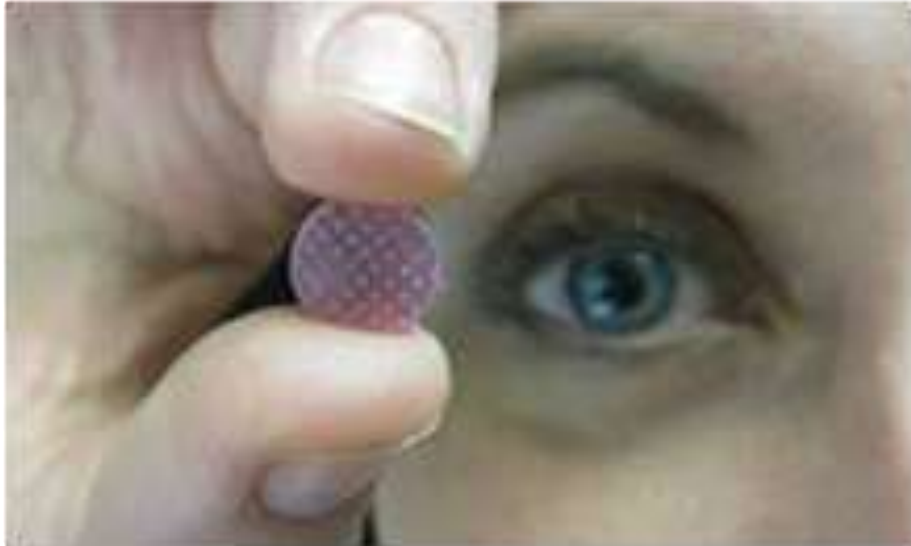


**Figure 2.17** Sugar Microneedle ([www.kcl.ac.uk](http://www.kcl.ac.uk))

**Sugar** (sucrose) micro needle array (Figure 2.17) has been used by Kings College, London. Sugar microneedles dried up with vaccines get dissolved when inserted into the skin. Silicon mould is used for casting sugar microneedles ([www.kcl.ac.uk](http://www.kcl.ac.uk)).

Lifeng et al. (2013) used **poly (ethylene glycol) diacrylate (PEGDA)** to fabricate polymeric microneedle using photo lithography technique for drug delivery. Tests conducted show that the PEGDA can be used as microneedle for drug delivery.

From literature, **SU-8** is found to be the most suitable material for fabrication of micro components especially with high-aspect ratio by lithography process. Its mechanical properties like elastic modulus and hardness are also similar to PMMA. Also, SU-8 is mostly referred as biocompatible material (Nemeni et al., 2013). Sung et al. (2008) indicated that SU-8 is biocompatible after proper curing and sterilisation and is little to no toxic. Gabriela et al. (2003) successfully tested SU-8 on test animal and concluded that gold, silicon nitride, silicon dioxide and silicon are biocompatible and gold, silicon nitride, silicon dioxide and SU-8 showed reduced bio fouling. Ferdinand Walthe et al. (2007) concluded by conducting cell proliferation assays on plasma-

activated SU-8 that SU-8 is biocompatible but do not allow tissues to grow on SU-8 unless activated with oxygen plasma.

**Poly lactic acid (PLA)** is prepared by polymerising the fermented renewable agricultural feed stocks such as corn starch. It is biodegradable and has properties comparable to petroleum-based products (Victoria et al., 2005). Kyriacos et al. (2009) had reported polyglycolic acid (PGA) may be suitable for orthopaedic applications. PLA is suitable for slow releasing of bioactive agents in situ. PLA has degradation duration of about six months to two years (Donald, 2001).

**PMMA**, also called as acrylic glass, is compatible with human tissue. It is commonly used to manufacture intraocular lenses that are implanted in eyes. PMMA is also used as bone cement to affix the bone and prosthesis in orthopaedic surgery. It is transparent, strong and light weight. To reduce wrinkles and scars, PMMA microspheres are suspended in biological fluid and injected under the skin. To meet the stringent requirement of pressure rated bioprocess chromatography columns, acrylic tubes are used as alternative to stainless steel. PMMA is durable and safe; hence, it is used as material for incubators.

Advantages of PMMA:

- Bio-compatible and bio-degradable
- Non - toxic
- Long service life
- Easy to fabricate by thermoforming
- 100% recyclable
- Relatively easy to manipulate
- Versatile and reliable
- Encourages tissue growth

## **2.4 COMPARISON OF MECHANICAL PROPERTIES OF MICRONEEDLE MATERIALS**

Mechanical properties of various materials that were used as microneedle materials are listed in Table 2.4. Metallic needles have very high tensile strength, and sugar has the least tensile strength.

**Table 2.4** Mechanical Properties of Microneedle Materials

Material	Tensile Strength	Yield Strength	Elongation %	Young's Modulus
	MPa	MPa		GPa
SS304	540	250	45	180
Titanium ASTM (Grade 1-5)	240-550	170-483	24-15	103-107
Silicon	7,000	-	-	135-185
Sugar	1.3	-	-	
PLA	57.8	-	10	2.7-16
Polymers-PMMA	48-76	-	2-10	1.3-3

## 2.5 SUMMARY

Patric et al. (2002), Yu Mike Ch (2010), Salvo et al. (2012), Vanel berghe et al. (2011) and Miyako, (2015) carried out research in using dry electrodes for biopotential measurement. Results of their research show that the dry electrodes are promising alternative to wet electrodes. Micro fabrication processes like deep reactive ion etching (DRIE), photo lithography, 3D printing, micro molding and milling were used in fabrication of dry electrodes. PDMS material was used as a mould material for replicating micro needles. Materials like Silicon, SU-8, Foam and Copper layer, PDMS, and Beryllium copper were used by various researchers. Literature shows the use of Ag/AgCl, titanium, parylene and gold coating on electrodes to improve the EEG signal quality.

From the point of fabrication of micro features with titanium and stainless steel materials offers more challenges compared to polymers. The speeds and feeds that could be used for micromachining of PMMA can be manifold compared to the cutting conditions used for machining metallic micro needles. This offers huge advantage in

improving productivity. Stainless steel and Titanium can be a choice of microneedle material if the cost making is not a concern when compared to polymer.

Silicon and metal microneedles are brittle; there is a possibility of accidental breakage. Also, as these materials are not biodegradable, biocompatibility is still questionable. On the other hand, biocompatible polymers will not be an issue with human skin. As failure forces for polymer microneedle are much more than the forces required for penetrating the skin, biopolymers have potential for human health monitoring. PMMA is a bio compatible material. PMMA had been used as micro needle material for DNA vaccination by Seonget et al. (2010). However, use of PMMA as microneedle material for electro potential measurement has received little attention. Analysis of mechanism of fascicle insertion into the skin by mosquito is found to be useful in designing micro needle geometry.

Not all microneedle designs can penetrate into the skin and at the same time to tap the biopotential signals. No previous study has been made to model and analyse the mechanical behaviour of PMMA microneedle and behaviour of skin while insertion into skin. There has not been any previous study on optimisation of base diameter and pitch distance between needles with respect to skin penetration and strain. Also, there is no previous study made on coating of silver on PMMA using electroless deposition. Also, PMMA as a material has not been used in micro additive process for micro needle fabrication. Similarly, micro machining of PMMA micro needles has also been not attempted. Stainless steel and Titanium materials are electrically conductive. PMMA is not conductive and hence conductive coating needs to be done to acquire bio potential signals. Salvo et al. (2012) used two step process for metallisation of bio-compatible acrylic-based Resin (Full Cure® 720). Titanium layer was coated first for improving the adhesiveness and then gold was coated to make acrylic material electrically conductive. The same method can be adapted for making PMMA electrically conductive. However, it calls for optimisation coating thickness. Cost of conductive coating can be brought down by using a batch of microneedle patches for coating together.

In this research work, effort is made to use PMMA as material for micro needle. Design and analysis of micro needle is carried out to ensure that the micro needle array would be able penetrate the skin with less deformation. Experimentations are carried out using micro stereolithography, micromolding and micro machining to establish the process for fabrication of PMMA micro needles. Effort is made to find out the failure loads of the micro needles when forces are applied in axial and transverse direction. Also, effort is made to have conductive coating on PMMA micro needle for EEG signal acquisition.

## CHAPTER 3

### MICRONEEDLE DESIGN AND ANALYSIS

#### 3.1 INTRODUCTION

In this chapter, design and analysis of microneedle is dealt. The objective of the study is to design the microneedle to assure robust design so that the needle can be inserted without breaking. Park et al. (2007) estimated that the force required for piercing skin was about 5 mN for polymer material having Young's Modulus of 3 GPa. Also, recommendation was made to use geometries with an aspect ratio (length-to-equivalent diameter) of below 12:1 and suggested to use needles with sharp tip that facilitate insertion. For the same cross sectional area of rectangular and circular needles, the axial load carrying capacity remains same. From the point of fabrication, circular microneedle geometry is preferred.

The effective working of a microneedle poses significant challenges during design and development. Following are the few major requirements need to be considered during the development of microneedle.

- Needle needs to be biocompatible
- Needle should have longer life (two days or more)
- It should be painless to user
- Needle should withstand penetration (compressive) force
- Needle should withstand shear force
- It should be sharp enough
- Needle should have high electrical conductivity

### **3.2 PARAMETERS FOR DESIGN**

- Type of material
- Tensile strength and Young's modulus
- Base diameter and Tip diameter
- Length
- Compressive force on microneedle during insertion
- Bending and Shear force on microneedle during use

Human skin consists of epidermis and dermis. Epidermis has a thin top layer called stratum corneum. Microneedle has to penetrate and overcome the resistance offered by stratum corneum. Microneedle is not required to reach dermis that contains living cells, nerves and blood vessels, as otherwise it is painful; however, it has to penetrate through the stratum corneum and it has to have more contact with the living cells of epidermis. The stratum corneum is of around 15  $\mu\text{m}$ , which also varies from person to person and different locations of human body. The thickness of epidermis is varies from 150 to 250  $\mu\text{m}$ . Based on the thickness of stratum corneum (15  $\mu\text{m}$ ) and epidermis (150 to 250  $\mu\text{m}$ ), the length of needle is fixed as 200  $\mu\text{m}$  to ensure the needle is very much in contact with living cells of epidermis. Penetration is easier if the tip is sharp. Keeping manufacturing challenges and strength of the needle into account, the tip diameter was fixed as 0.005mm.

### **3.3 FORCE REQUIRED TO PIERCE THE HUMAN SKIN**

A study on pressure distribution during piercing of needle into the skin was carried out by Henry et al. (1998). The theoretical pressure required to pierce human tissue was reported to be 3.183 MPa. The decrease in pressure was observed once the needle enters into the skin after a certain depth. After piercing the skin, the pressure was about 1.6 MPa (Priyanka et al., 2004). Force required to pierce the skin depends on the tip diameter and properties of the skin. Based on theoretical pressure required for piercing the skin, force required for puncturing the skin is calculated for tip diameter of 0.005 mm.

The resistance offered by human tissue is given by the following equation.

$$F_{\text{tissue}} = P_{\text{tissue}} \times A \quad \text{Eqn. 3.1}$$

$$P_{\text{tissue}} = 3.183 \text{ MPa}$$

$$F_{\text{tissue}} = 3.183 \times \frac{\pi \times 0.005^2}{4}$$

$$F_{\text{tissue}} = 0.00006 \text{ N}$$

An axial force of 0.06 mN is sufficient for penetration of human skin by a single microneedle having tip diameter of 0.005 mm. Table 3.1 shows the force required to pierce the skin for different tip diameters. After piercing SC, the force required for further penetration will be much less, as the skin below SC is softer (Priyanka et al., 2004).

**Table 3.1** Force Required for Piercing the Skin

Parameters	1	2	3	4	5
Tip dia., $\mu\text{m}$	5	10	15	20	30
$F_{\text{tissue}}$ , N	0.00006	0.00025	0.00050	0.00100	0.00220

### 3.4 FORCES ACTING ON MICRONEEDLE

When the microneedles penetrate into the top layer of skin, stratum corneum, there will be a compressive load on the needles. Stratum corneum is a tougher than the layer beneath it. Also, microneedles are subjected forces of bending, and shear as shown in the Figure 3.1 depending upon the direction of application of microneedle.

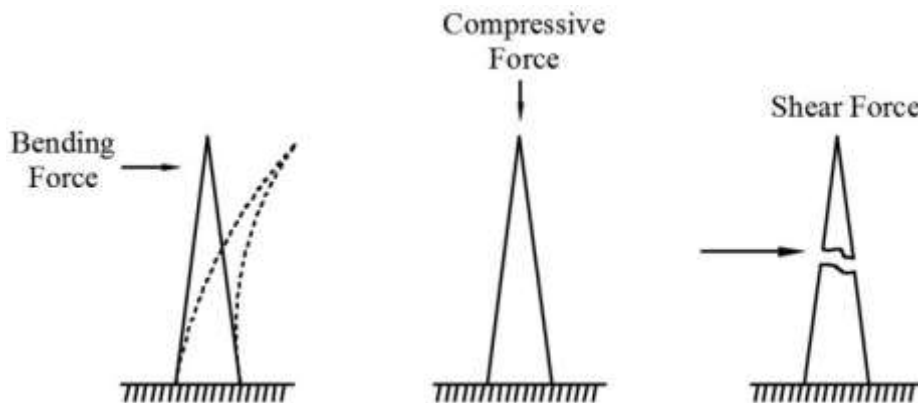


**Figure 3.1** Forces acting on Microneedle

### 3.5 MAXIMUM BENDING FORCE

In an ideal situation, the needle is expected to experience only compression due to axial load. In actual applications, the needle is also subjected to bending moment and shear load. Figure 3.2 shows the bending force action on microneedle.

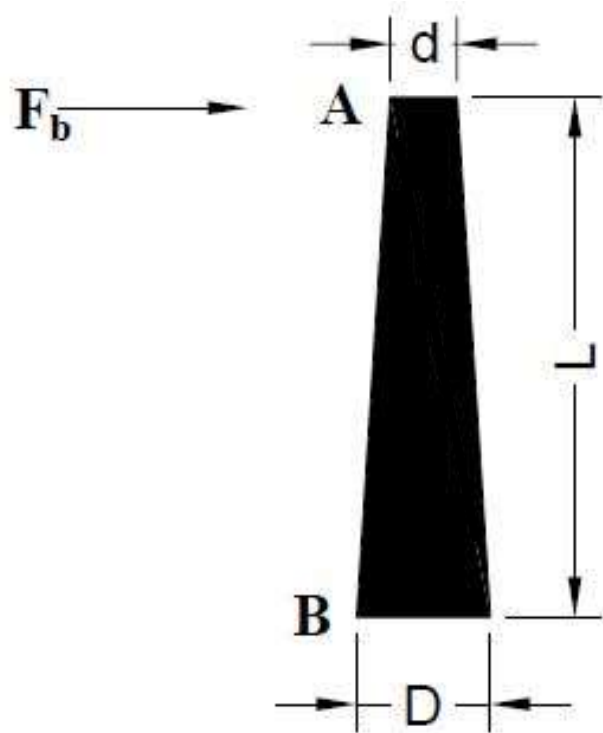


**Figure 3.2** Bending force on Microneedle

The maximum bending force that the microneedle can withstand is given by equation.

$$F_{bm} = S_y \times \frac{I}{cL} \quad \text{Eqn. 3.2}$$

Where  $S_y$  is the Yield strength, 50 MPa

$$I, \text{ Moment of inertia} = \frac{\pi d^4}{64}$$

$c$  is the neutral axis to outer edge of the microneedle,

$$c = \frac{D}{2} = \frac{0.05}{2} = 0.025 \text{ mm}$$

$L$ , length of the microneedle = 0.2 mm

$D$  is the base diameter of microneedle = 0.05 mm

$\rho$ , Specific gravity = 1.14 g/cm<sup>3</sup>

$$F_{bm} = S_y \times \frac{I}{cL}$$

$$= 50 \times \frac{\pi \times 0.05^4 / 64}{0.025 \times 0.2}$$

$$F_{bm} = 0.003 \text{ N}$$

$$F_{bm} = 0.0015 \text{ N (with factor safety of 2)}$$

Maximum bending force the needle can withstand is calculated for different diameters and is given in the table 3.2. As expected, large base diameter of the needle gives more strength against bending.

**Table 3.2** Maximum Bending Force of Microneedle

Parameters	1	2	3	4	5	6
Base dia, $\mu\text{m}$	50	70	90	110	130	120
Bending Force, $F_{bm}$ , N	0.0015	0.0042	0.0089	0.016	0.026	0.021

### 3.6 MAXIMUM AXIAL FORCE

Micro-needle is normally aimed for insertion in axial direction. The Figure 3.1 shows the axial force on single microneedle.

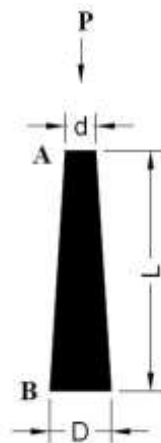


**Figure 3.3** Axial Force on Microneedle

To determine maximum compressive force, Euler equation is used for long column (Zhan et al., 2000) and Johnson's equation is used for short column. Slenderness ratio decides whether the column is short or long. If the slenderness ratio is less than the critical slenderness ratio then it is considered as short column (Zhan et al., 2000). For a tapered column, the surface area; A, varies with the height of the column. To evaluate the mechanical failure of the tapered microstructure, the general buckling formula for a straight column needs to be adapted to a tapered column by introducing an equivalent diameter. The equivalent diameter of a linearly tapered column can be calculated from the equation 3.3 to analyse a tapered member. This equivalent value can be used for computing the slenderness ratio and the critical load.

$$D_{eq} = D_{tip} + \left( \frac{D_{base} - D_{tip}}{3} \right) \quad \text{Eqn. 3.3}$$

$$\begin{aligned} \text{Critical Slenderness Ratio} &= \left( \frac{L}{k} \right)_{cr} \\ &= \sqrt{\frac{\pi^2 E}{2 \times S_y}} \end{aligned} \quad \text{Eqn. 3.4}$$

Length of the needle, L = 0.2 mm

Young's Modulus, E = 2770 MPa

Yield Strength, Sy = 50 MPa

Factor of Safety = 2

Radius of gyration,  $k = \sqrt{\frac{I}{A}}$

$$\text{Critical Slenderness Ratio} = \left( \frac{L}{k} \right)_{cr} = \sqrt{\frac{\pi^2 \times 2770}{2 \times 25}} = 23.36$$

Calculation of slenderness ratio for the needle having equivalent diameter of 0.0633 mm and length of 0.02mm:

$$\text{Slenderness Ratio}, \frac{L}{k} = \frac{L}{\sqrt{\frac{I}{A}}}$$

$$\text{Slenderness Ratio}, \frac{L}{k} = \frac{L}{\sqrt{\frac{\frac{\pi D_{eq}^4}{64}}{\frac{\pi D_{eq}^2}{4}}}}$$

$$\frac{L}{k} = \frac{0.02}{\sqrt{\frac{\frac{\pi 0.063^4}{64}}{\frac{\pi 0.063^2}{4}}}} = 13.33$$

Slenderness ratios calculated for various equivalent diameters of the micro-needle are calculated given in the table 3.3.

**Table 3.3** Slenderness Ratio

Parameters	1	2	3	4	5	6
Tip dia, $\mu\text{m}$	5	10	15	20	30	5
Base dia, $\mu\text{m}$	50	70	90	110	130	120
D equivalent, $\mu\text{m}$	20	30	40	50	63.33	43
Length, $\mu\text{m}$	200	200	200	200	200	200
Slenderness Ratio, $L/k$	40	26.6	20	16	13.33	18.62
Critical Slenderness Ratio, $L/k$	23.36					
Column Type	Long	Long	Short	Short	Short	Short

From the table 3.3, it can be observed that the needles having equivalent diameter 20 and 30  $\mu\text{m}$  are to be treated as long column due to their high slenderness ratio. Whereas other needles are treated as short column as their slenderness ratio is less than the critical slenderness value.

Maximum force that the needles withstand due to buckling can be calculated (Park et al., 2007) by considering needles under Sl. No. 3, 4, 5 & 6 of table 3.3 as short column by using Johnson's formula:

$$P_{cr} = A S_y \left[ 1 - \frac{S_y \left( \frac{L_e}{r_g} \right)^2}{4\pi^2 E} \right] \quad \text{Eqn. 3.5}$$

Deq = 0.02 mm

Sy = Yield Strength of PMMA= 50 MPa

Factor of safety= 2

Sy = 50/2 = 25 MPa

Le, Effective Length = L x K

L, Length of the needle= 0.2

K, End fixity factor = 0.7

Le, Effective Length = 0.2 x 0.7=0.14mm

R = Eq. Dia./2=0.043/2

rg, Radius of gyration= D/4= 0.050/4=0.0125

E- Young's Modulus= 2770 MPa

The above values are substituted in eqn. 3.5 to calculate P<sub>cr</sub>

$$P_{cr} = 0.00363 \times 25 \left[ 1 - \frac{25 \left( \frac{0.14}{0.0125} \right)^2}{4\pi^2 2770} \right]$$

P<sub>cr</sub> = 0.036 N (for base diameter of 50 μm, tip diameter of 5 μm and height of 200 μm)

Micro needles can be modelled as long column for needles having equivalent diameters 20 and 30 μm and the Euler equation for buckling load calculation can be applied.

$$P_{Cr} = \frac{C\pi^2 EI}{L^2} \quad \text{Eqn. 3.6}$$

Critical load calculation for equivalent diameter of 0.020 mm by substituting values in eqn. 3.6.

$$P_{Cr} = \frac{0.2 \times \pi^2 \times 2770 \times \frac{\pi \times 0.02^4}{64}}{0.2^2} = 0.001 \text{ N}$$

Critical loads for various base diameters and tip diameters were calculated and presented in Table 3.4.

**Table 3.4** Critical Load of Failure

Parameters	1	2	3	4	5	6
Tip diameter, $\mu\text{m}$	5	10	15	20	30	5
Base diameter, $\mu\text{m}$	50	70	90	110	130	120
D equivalent	20	30	40	50	63.33	43
Length, $\mu\text{m}$	200	200	200	200	200	200
Critical load, Pcr N	0.001	0.005	0.029	0.048	0.074	0.036
Minimum force required to pierce skin Skin pr. $\times$ area, N	0.00006	0.00025	0.0005	0.001	0.002	0.00006

From the table, it could be observed that the critical load of failure of microneedle due to buckling is much higher than the minimum force required piercing the skin.

### 3.7 MAXIMUM SHEAR FORCE

Shear force is another mode that can cause failure to micro needle. Shear strength is approximated as half the value of yield strength. Needle can shear at any plane depending upon where the load is applied. Here, equivalent diameter is considered while calculating area of shear.

$$\text{Maximum shear force, } S_{sh} = \frac{S_y}{2} \times A \quad \text{Eqn. 3.8}$$

Factor of safety = 2

Maximum shear force the needle can withstand for equivalent diameter of 0.020 mm diameter is calculated as below

$$F_{sh} = \frac{50}{2 \times 2} \times \frac{\pi \times 0.02^2}{4} = 0.0039\text{N}$$

The maximum shear force the needle can withstand for other equivalent diameters are calculated and listed in the table 3.6.

**Table 3.5** Maximum Shear Force

<b>Parameters</b>	<b>1</b>	<b>2</b>	<b>3</b>	<b>4</b>	<b>5</b>	<b>6</b>
Tip diameter, $\mu\text{m}$	5	10	15	20	30	5
Base diameter, $\mu\text{m}$	50	70	90	110	130	120
D equivalent	20	30	40	50	63.33	43
Maximum shear Force, N	0.0036	0.0083	0.0157	0.0245	0.0389	0.0181

From the table 3.5, it is evident that the larger needle base diameter and larger tip diameter can take higher shear force.

### **3.8 DEFORMATION OF MICRONEEDLE**

The needle is considered as supported at the end B and subjected to compressive load of P from the top. Deformation at critical load of failure can be calculated by using the formula from strength of mechanics. The equation for deformation due to axial loading for varying cross section is given as:

$$\delta = \frac{4PL}{\pi E d D} \quad \text{Eqn: 3.7}$$

Deformation for  $d = 0.005 \text{ mm}$ ,  $D = 0.050 \text{ mm}$ ,

Critical load of failure:  $0.001 \text{ N}$

$$\delta = \frac{4 \times 0.001 \times 0.2}{\pi \times 2770 \times 0.005 \times 0.050}$$

$$\delta = 0.00036 \text{ mm}$$

$$\delta = 0.36 \mu\text{m}$$

Deformation of the needle for critical load for various micro needle dimensions are calculated and given in Table 3.6.

**Table 3.6** Load vs. Deformation of Microneedle

<b>Parameters</b>	<b>1</b>	<b>2</b>	<b>3</b>	<b>4</b>	<b>5</b>	<b>6</b>
Tip diameter, d, $\mu\text{m}$	5	10	15	20	30	5
Base dia., D, $\mu\text{m}$	50	70	90	110	130	120
Length, L, $\mu\text{m}$	200	200	200	200	200	200
Critical load, P <sub>cr</sub> , N	0.001	0.0185	0.031	0.048	0.077	0.034
Deformation, $\delta$	0.36 $\mu\text{m}$	1.9 $\mu\text{m}$	2.0 $\mu\text{m}$	1.7 $\mu\text{m}$	3.8 $\mu\text{m}$	5.4 $\mu\text{m}$

Maximum deformation of the needle was from the minimum size of the microneedle. The deformation was less than 5%.

### **3.9 FINITE ELEMENT ANALYSIS**

Design on PMMA microneedle insertion into skin is reported. Simulation study was performed using Solidworks Simulation Package. Design of microneedle array block is carried out to meet below requirements. The model dimensions and variables selected are also listed in Table 3.4. The aim of the study is to design microneedle array for skin insertion around 200  $\mu\text{m}$  with allowable strain as 5-7%. The study involves testing microneedle block with different microneedle pitch, base diameter and compressive load.

Keeping skin anatomy into consideration, microneedle is expected to penetrate skin to a depth of at least 120  $\mu\text{m}$  and the strain on needle length is to be  $\leq 5-7\%$ . To model the microneedle, parameters like microneedle block size, length, tip diameter and number needles in the block are kept as constant. All these parameters are listed in the table 3.7.

**Table 3.7** Constant Parameters/Dimensions

Microneedle block size	10 mm
Number of needles in array	100
Tip diameter	$\geq 5 \mu\text{m}$
Length	200 $\mu\text{m}$

It was necessary to arrive at set of values for pitch, base diameter and the load. Based on manufacturing considerations and the load required to penetrate the skin, values were arrived and listed in Table 3.8.

**Table 3.8** Minimum and Maximum Value of Variables for FEM Analysis

Parameter	Min.	Max.
Pitch of the needles	0.3 mm	0.7 mm
Base diameter	50 $\mu\text{m}$	120 $\mu\text{m}$
Load	5 N	10 N

Table 3.9 gives the consolidated data consisting of requirement, fixed parameters and variable parameters. Table 3.9 gives the values for needle dimensions and variables like pitch, base diameter and load.

**Table 3.9** Microneedle Dimensions & Variables

Model Dimensions and Variables	Value
Microneedle penetration into skin	$\geq 120 \mu\text{m}$
Microneedle block size	10 mm dia. $\times$ 2 mm thick
No. of needles in array (For max. pitch of 0.7 mm)	100
Tip diameter	5 $\mu\text{m}$
Pitch of the needles, mm	0.3, 0.4, 0.5, 0.6, 0.7
Base diameter, micrometres	50, 60, 70, 80, 90, 100, 110, 120
Load, N	5, 6, 7, 8, 9, 10

### *Assumptions*

- Complete skin anatomy is considered as having homogenous mechanical properties.
- Linear and static model is considered for analysis.

### **3.9.1 Model information**

Information on microneedle material and its properties, skin properties, parameters for meshing, loads and fixtures are given in the tables 3.10.

**Table 3.10** Model Information for FEM Analysis

<b>Treated As</b>	<b>Volumetric Properties</b>
Solid body	Mass: 0.187019 g Volume: 157.158 mm <sup>3</sup> Density: 1.190 g/cm <sup>3</sup> Weight: 0.00183278 N
Solid body	Mass: 0.000399007 kg Volume: 339.292 mm <sup>3</sup> Density: 1.176 g/cm <sup>3</sup> Weight: 0.00391027 N

Microneedle made out of PMMA and skin is considered as solid body. Skin is considered to exhibit property uniformly in all direction (isotropic). Skin is assumed to behave in a linear mode and is considered as elastic. Table 3.11 and table 3.12 gives out the complete physical properties of microneedle material PMMA and skin.

**Table 3.11** Physical Properties of Microneedle

<b>Physical Properties Micro Needle</b>	
Material	PMMA
Model Type	Linear Elastic Isotropic
Default failure criterion	Max von Mises Stress
Yield strength	65 MPa
Tensile strength	81 MPa
Elastic modulus	2,770 MPa
Poisson's ratio	0.394
Mass density	1,190 g/cm <sup>3</sup>

**Table 3.12** Physical Properties of Skin

<b>Physical Properties Skin</b>	
Model type	Linear Elastic Isotropic
Default failure criterion	Max von Mises Stress
Yield strength	0.5 MPa
Tensile strength	0.6 MPa
Elastic modulus	5 MPa
Poisson's ratio	0.49
Mass density	1,176 g/cm <sup>3</sup>

### 3.9.2 Meshing

Curvature-based MESH and elements with tetrahedron shape (Figure 3.4), which has four vertices, six edges and four triangular faces were considered in meshing. Details of parameters considered for meshing are listed in the Table 3.13.

**Table 3.13** Parameters Considered for Meshing

Mesh used	Curvature-based mesh
Jacobian points	4 points
Maximum element size	0.891 mm
Minimum element size	0.178 mm
Total nodes	75,479
Total elements	50,116
Maximum aspect ratio	228.25
% of elements with aspect ratio < 3	86.3
% of elements with aspect ratio > 10	3.48
% of distorted elements (Jacobian)	0

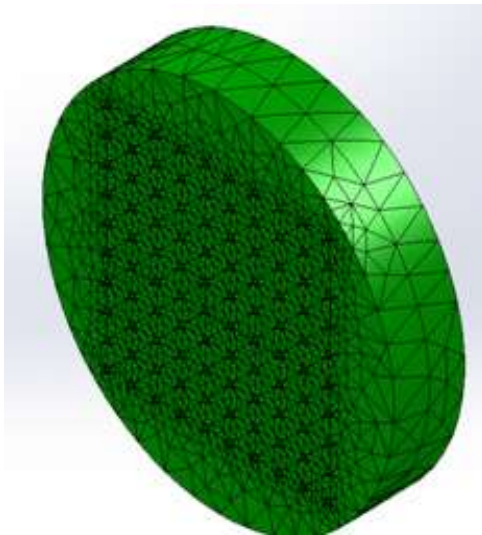


**Figure 3.4** Microneedle Block With Tetrahedral Solid Mesh

### 3.9.3 Output from Finite Element Analysis

Strain plots for various loads, pitches and base diameters are generated as output from FEM analysis. Output is generated for varying loads of 2 N to 10 N, pitches of 0.3 mm to 0.7 mm and base diameters of 0.05  $\mu\text{m}$  to 120  $\mu\text{m}$ .

Figure 3.5 shows the typical output for 0.4 mm pitch and load 6 N. From Figure 3.5, it is observed that strains on all needles are uniform and the variation in strain is between 3 - 6  $\mu\text{m}$ , which is less than 5% of 200  $\mu\text{m}$  (needle length).

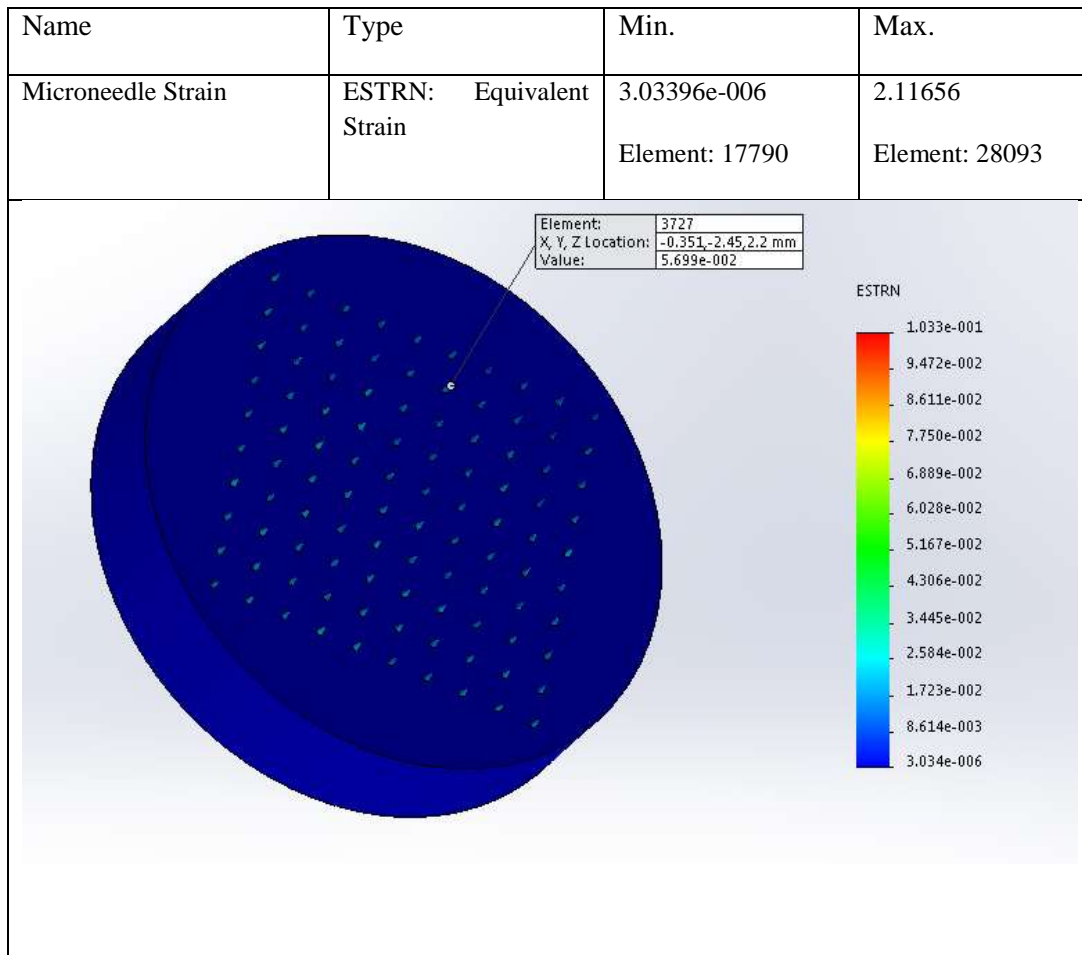


**Figure 3.5** Strain Plot

Displacement plot of skin due to penetration by microneedle is shown in Figure 3.6. Centre portion of the plot shows that the deformation of whole skin to certain depth.

Valley created by the needles shows the deformation of the skin due to individual microneedle.

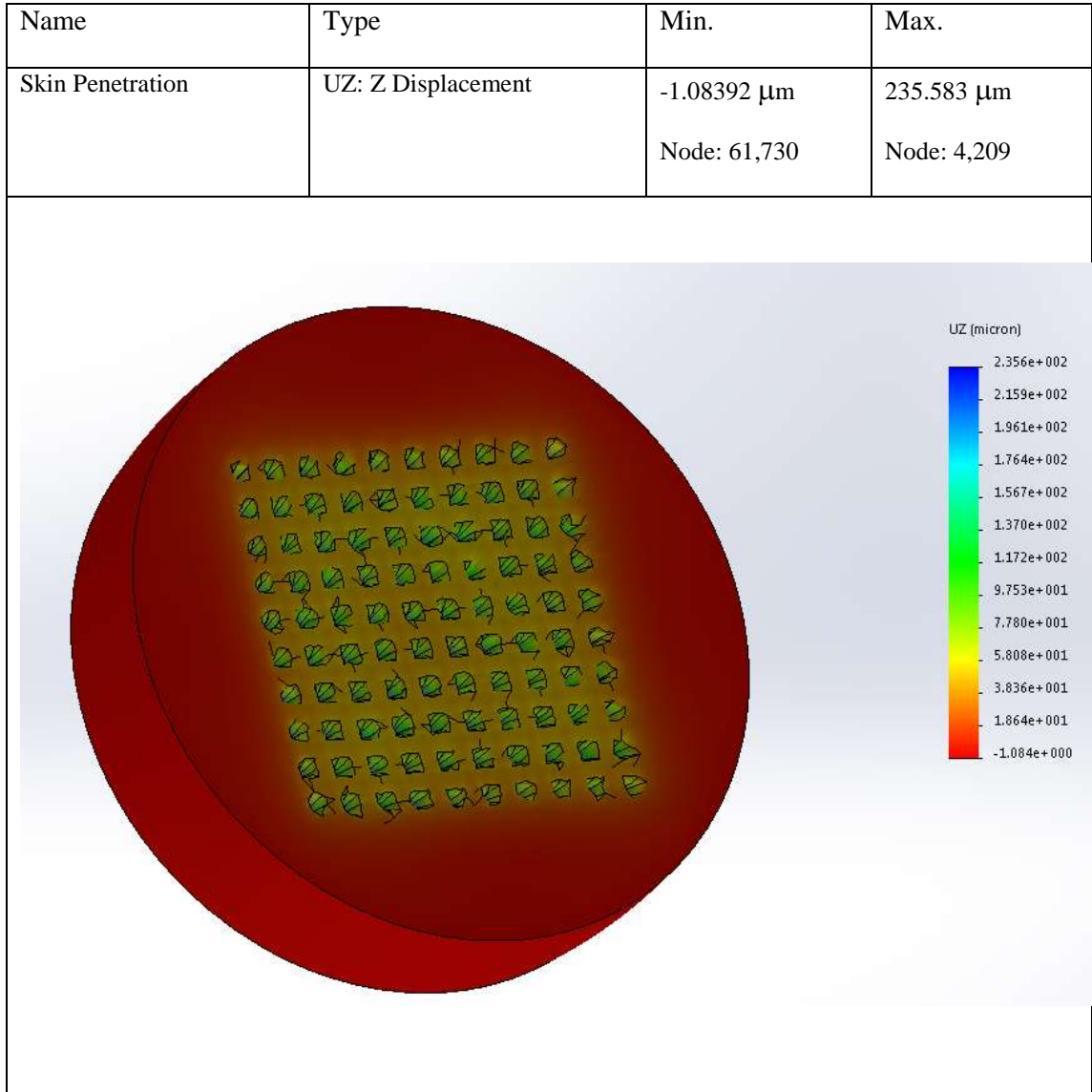


**Figure 3.6** Displacement Plot

### 3.10 LOAD VS. PENETRATION AND STRAIN WITH RESPECT TO APPLIED LOAD

To arrive at optimum microneedle design, simulation study was performed by applying various loads on different geometries of microneedles. Height of the needle is kept constant. Load is varied from 2 N to 10 N, and the base diameter is varied from 0.04 mm

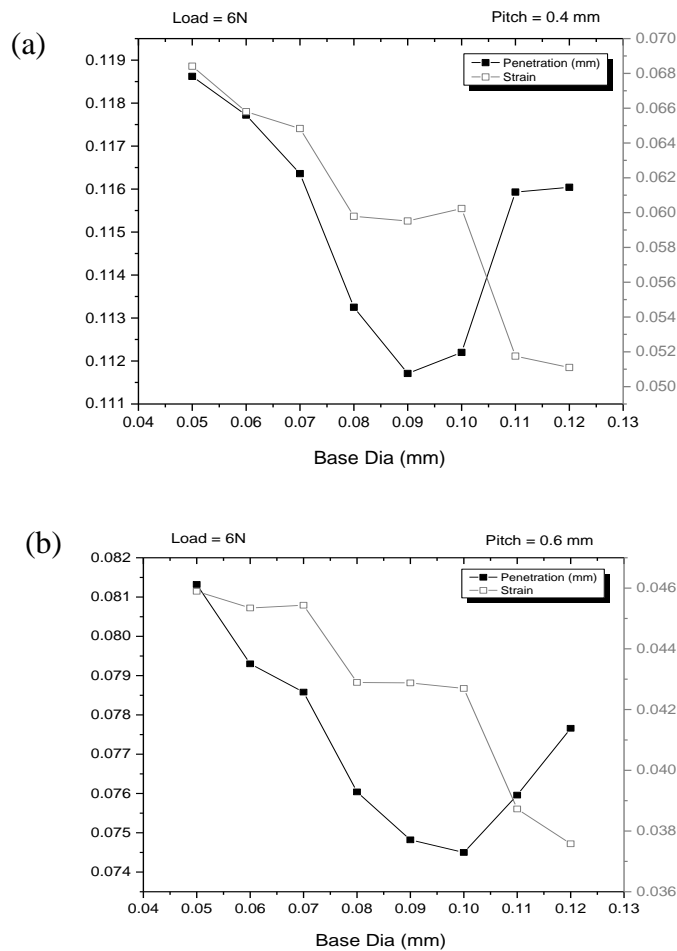


**Figure 3.7** Plots on Penetration, Strain Vs. Base Diameter at 6 N Load for a Pitch of 0.4 mm & 0.6mm

to 0.120 mm. 0.3 mm to 0.7 mm pitch values are considered for study. Results arrived are plotted as Load vs. Penetration of the needle into the skin and strain with respect to applied load for the given base diameter and pitch (Figure 3.7).

Figure 3.8 shows the reduction in strain and the penetration for increase in base diameter increases. Reduction is due to the reason the increase in base diameter reduces the included angle of the conical microneedle.

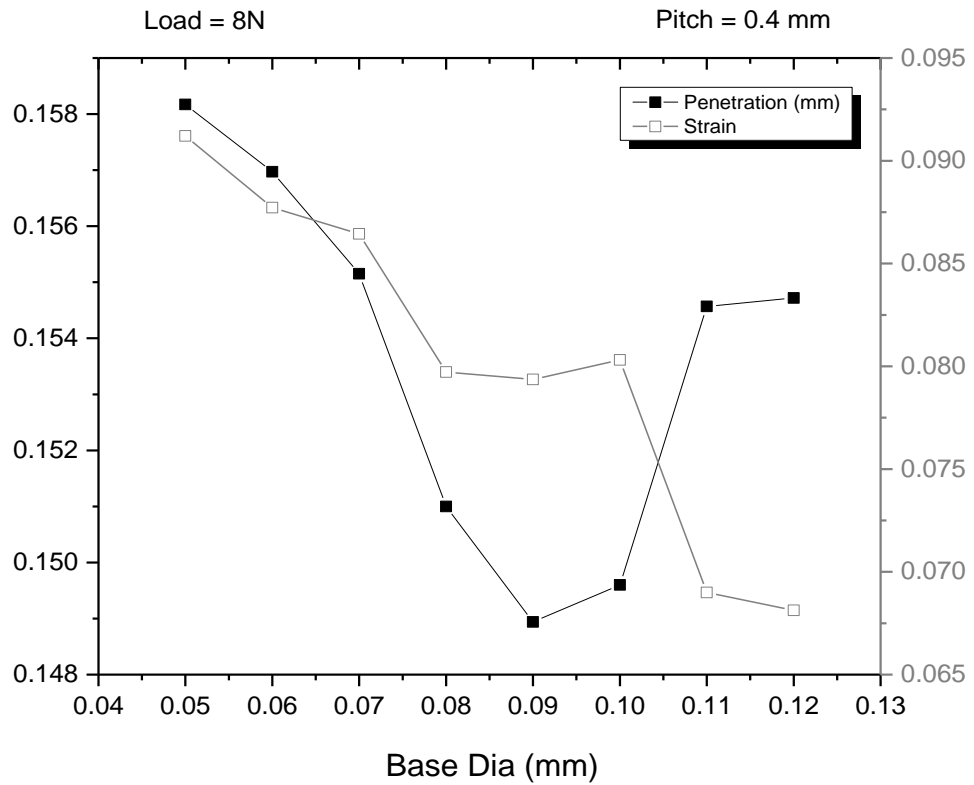


**Figure 3.8** Plot on Penetration, Strain vs. Base Diameter at 8 N Load for a Pitch 0.4 mm

Steeper the needle better would be the penetration. Beyond certain point, i.e., from 0.09 mm base diameter, increase in base diameter leads to increase in penetration due to the reason the needle becoming strong enough to penetrate the skin. At 0.12 mm base diameter, the penetration is high and the strain is almost the least.

Plot in Figure 3.9 shows similar trend as that of plots in Figure 3.8. Reduction in strain is observed when the base diameter keeps increasing. Increase in penetration occurs after 0.09 mm base diameter.

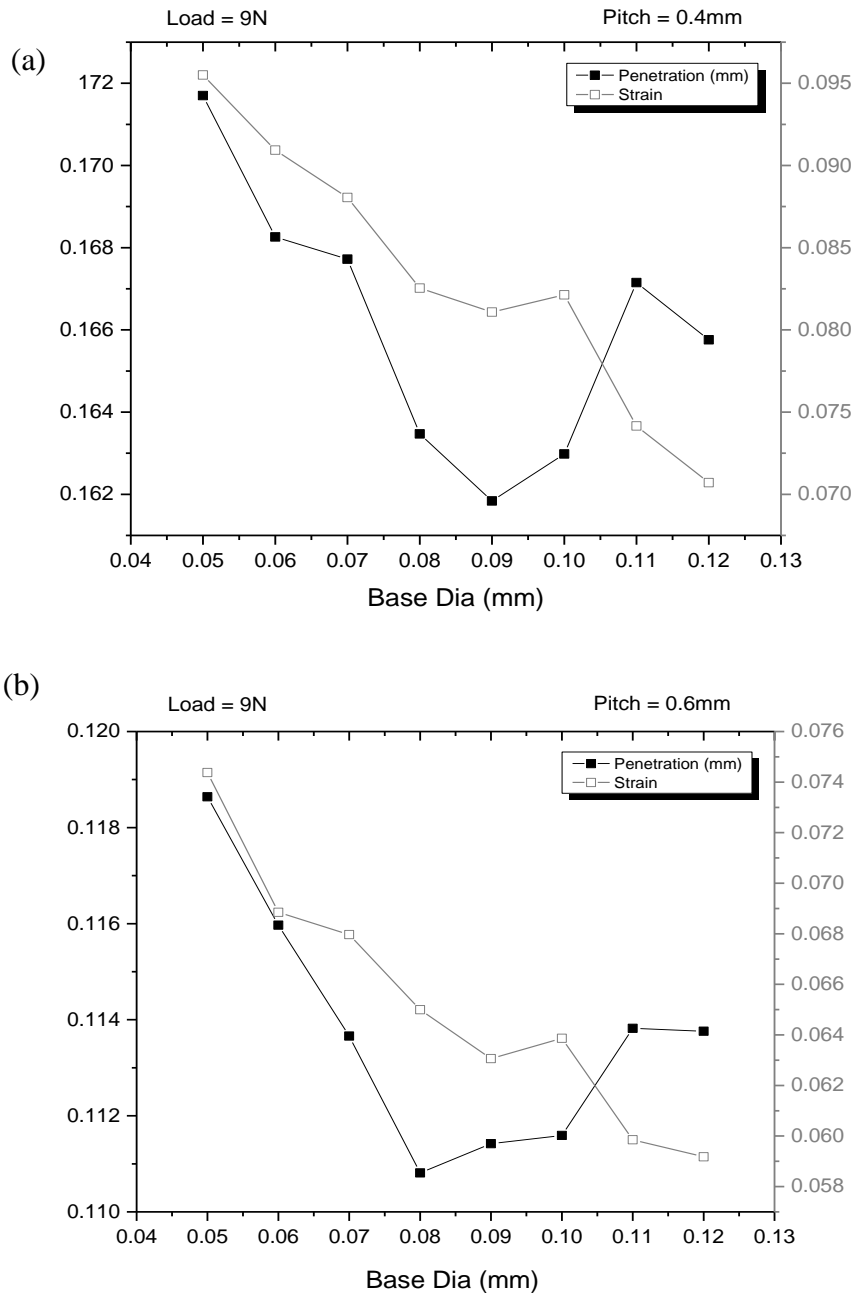


**Figure 3.9** (a) and (b) Plot on Penetration, Strain vs. Base Diameter at 9 N Load for a Pitch of 0.4 mm & 0.6 mm

Figure 3.10 shows the reduction in strain and the penetration as the base diameter increases. Reduction is due to the reason the increase in base diameter reduces the included angle of the conical microneedle.

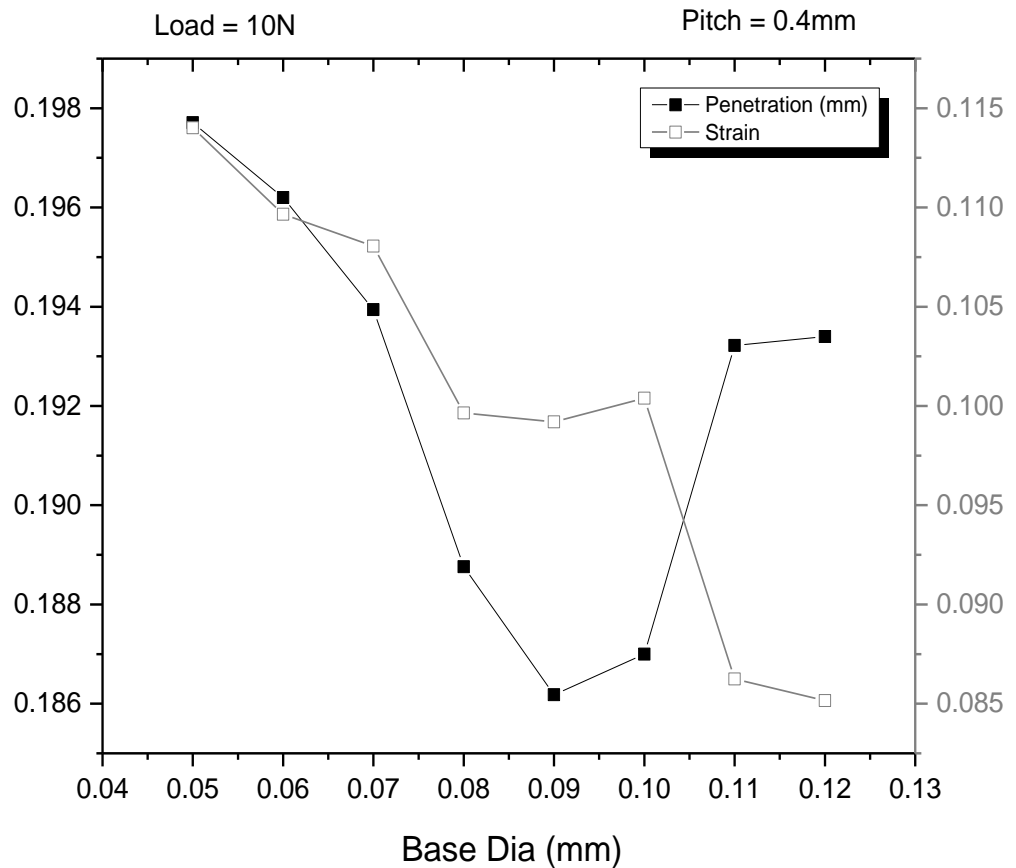


**Figure 3.10** Plot on Penetration, Strain vs. Base Diameter at 10 N Load for a Pitch of 0.4 mm

Plots in Figure 3.10 show the reduction in strain and the penetration as the base diameter increases. Reduction is due to the reason the increase in base diameter reduces the included angle of the conical microneedle. In the simulation study, as expected, increase in load leads to increase in strain and penetration of the microneedle array. As the base diameter increases, strain is found to be less and the penetration of the needle is found to be reducing. Beyond certain value, the

penetration of the needle increases due to the reason the needle has become strong. Table 3.14 shows the selected results for pitches for which the penetration is more and the strain is less.

**Table 3.14** Strain and Penetration for Applied Load

Sl. No.	Load (N)	Penetration (mm)	Base Dia. (mm)	Needle Pitch (mm)	Strain
1	6	0.116	0.12	0.4	0.051
2	6	0.118	0.12	0.6	0.068
3	8	0.154	0.12	0.4	0.068
4	9	0.115	0.06	0.4	0.068
5	9	0.165	0.06	0.6	0.070
6	10	0.129	0.12	0.4	0.090

### 3.11 SUMMARY

Design and analysis of microneedle for skin penetration is described in this chapter. The information on requirement of microneedle is explained. Geometry of microneedle with respect to cross-section and length is discussed. Based on anatomy of skin, length of microneedle is fixed as 200  $\mu\text{m}$ . This is arrived to avoid microneedle reaching nerves through dermis of the skin. An axial force of 0.06 mN is sufficient for penetration of human skin by a single microneedle having tip diameter of 0.005 mm. This is because pressure required to pierce human tissue is 3.183 MPa. Safe loads for failure due to different failure modes like bending, compressive and shear forces are calculated. Safe bending load for single microneedle having base diameter of 120  $\mu\text{m}$  and tip diameter of 5  $\mu\text{m}$  is 0.021N. Safe load in compression is 0.036 N and in shear is 0.018N. It can be observed that the microneedle tend fail in shear much easily than bending and compressive loads. Microneedle penetration into

the skin is modelled, and simulation is performed for varying conditions of load, pitch and base diameter of the microneedle patch. Strain and penetration of microneedle into the skin are studied. Based on the simulation study, microneedle dimensions and pitch value are arrived for maximum penetration and minimum strain. From the table 3.14, it can be inferred that micro needle patch with the base diameter of 120  $\mu\text{m}$  and pitch of 0.4 mm gives maximum penetration and minimum strain. Micro needle dimensions like base diameter (120  $\mu\text{m}$ ) and tip diameter (5  $\mu\text{m}$ ) are almost in agreement with the design adopted by Seong et al. (2010). In their study, PMMA microneedle of base diameter 110  $\mu\text{m}$  and tip diameter of 15  $\mu\text{m}$  were used for electroporation of skin for gene delivery.

Experiments conducted for fabrication and characterisation of microneedle are dealt in Chapter 4.



## CHAPTER 4

### EXPERIMENTATION

#### 4.1 INTRODUCTION

This chapter gives a detailed insight into the various processes that have been considered during development of microneedles. The main focus is to develop microneedle using micro stereolithography (MSL), as it offers numerous advantages over other processes. Micro stereolithography is a mask less process and bottom up process. There will not be any material removal in this process. This process has got potential to deploy for large quantity production with latest developments happening in projection based MSL. In projection based MSL, entire layer is scanned at a time instead of scanning the polymer line by line. This chapter describes the use of scan based MSL system for microneedle fabrication. This is expected to pave way for migration to projection based MSL. There is a limitation regarding achievable finer feature size in micromolding and micro milling. Comparison of all these three processes is given in Table 3.1.

Table 4.1 Comparison of Various Processes

Sl.No.	Micro Stereolithography	Micro Moulding	Micro Milling
1	Bottom up process: No wastage of material	Near net shape process. Less wastage of material	Top down process: Wastage of Material due to removal
2	No tools/ Tooling required	Needs expensive Tooling	Micro cutting tools required
3	Feature size as small as 10 $\mu\text{m}$ possible	Limitation in minimum feature size 50 $\mu\text{m}$ and above possible	Limitation in minimum feature Size of 30 $\mu\text{m}$ and above possible
4	Scaling up possible with Projection MSL	Offers high volume production capability. Hence, reduced cost/piece	SPMs with multi spindle heads required to volume production

This chapter describes work carried out using micro stereolithography, micromolding and micromilling processes. Problem formulated and objectives defined were investigated along with the details of laboratory conditions, experimental setup, testing equipment used and procedure adopted for the experimental investigations.

#### Experimentation

- Micro needle fabrication by micro stereolithography with HDDA as material
- UV Curing of MMA
- Co-polymerisation of HDDA and PMMA
- Micro Molding
- Micro Machining
- Conductive Coating on PMMA

#### Testing and Characterisation:

- Peel off Test
- Compression Test
- Shear Test
- Insertion Test on Chicken Skin
- Test for electrical conductivity

## **4.2 FABRICATION OF MICRONEEDLE**

### **4.2.1 Fabrication of Microneedle by UV Curing**

Initially, experiments were conducted to fabricate microneedle by curing HDDA liquid resin by exposing UV light source. UV laser and UV LED are the light sources available for radiation curing. Radiation curing is a process used to transform the specially formulated 100% reactive liquids into solids with UV or any other light as energy source by polymerising and cross-linking of functional monomers and oligomers into a cross-linked polymer network (Takhcs &Wojnarovits, 1997).

In principle, UV light is exposed over the photocurable resin surface and then a light-induced photopolymerisation occurs, constructing solid microstructures. With focused light spot scanning, a focused laser spot permits micron-scale spatial resolution.

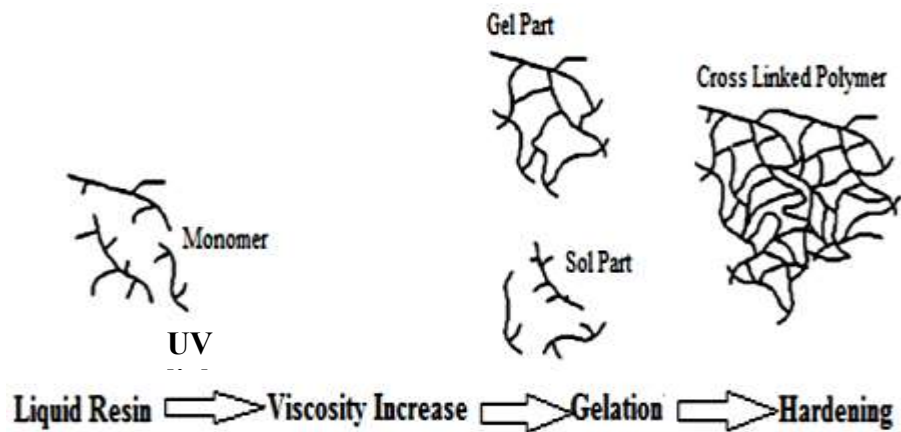


**Figure 4.1** The Cure Mechanism (Mcgrath et al., 1998)

Since most monomers or pre-polymers do not have the ability for self-initiation of cross-link upon irradiation, a low-molecular-weight organic molecule (initiators) introduction becomes necessary that will start polymerisation, through photo physical and photochemical processes (Mcgrath et al., 1998). Figure 4.1 shows a schematic representation of the curing mechanism for any photo-polymerisable resin. Photo initiators are mixed with monomers and are exposed to UV source.

During the irradiation of light, the photo initiators absorb some of the photons that are in excited state. Some of these are converted into reactive initiator molecules  $Pi^*$ . These molecules then react with monomers to form polymerisation initiative molecules,  $PM^*$ . This is the chain initiation step. Additional molecules go on to react and form longer molecules (Varadan et al., 2001)

Figure 4.2 shows the sequence of photo polymerisation process for HDDA monomer mixed with BEE initiator.

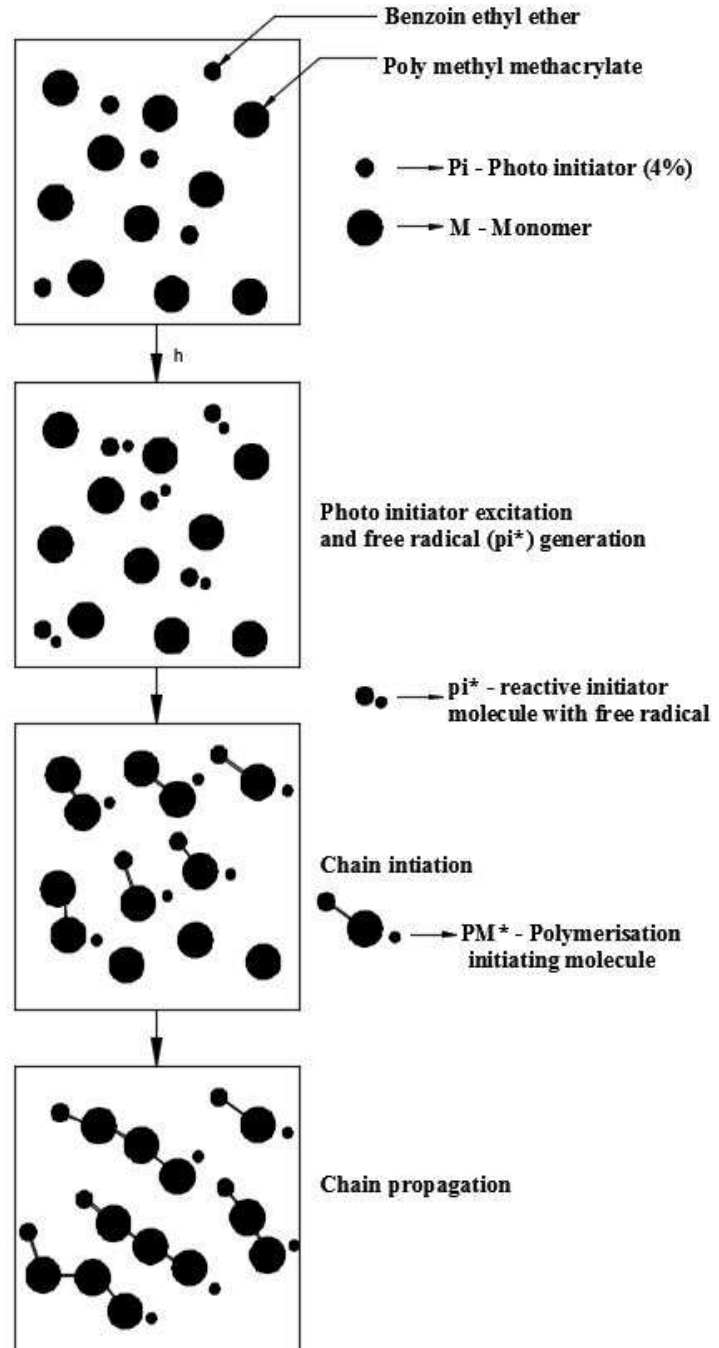


**Figure 4.2** Photo polymerisation (a) Monomer and Photo Initiator (b) Free Radical Generation (c) Polymerisation Initiating Molecule (d) Chain Propagation (Varadan et al., 2001)

### *Polymerisation of HDDA*

Initial experimentations were carried out using HDDA and the BEE initiator. In-house built MSL system was used for UV curing of HDDA. For the preparation of polymer, commercially available precursor material, 1,6-HDDA (Sigma Aldrich, USA) was selected as the monomer and mixed with benzoin ethyl ether (BEE, Sigma Aldrich, USA), a type I photo initiator undergoing a uni-molecular bond cleavage upon irradiation to yield free radicals. Table 4.2 and 4.3 shows the various properties of the precursor material.

**Table 4.2** Properties of 1,6-HDDA Monomer

Sl. No.	Properties	Values
1	Molecular weight	226
2	Chemical formula	C <sub>12</sub> H <sub>18</sub> O <sub>4</sub>
2	Appearance	Colourless to yellowish
4	Physical form	Liquid
5	Odour	Ester-like
6	Density at 25°C	1.015 g/cm <sup>3</sup>
7	Refractive index at 20°C	1.457
8	Boiling point	107°C at 0.3 mbar
9	Solidification point	8-11°C
10	Viscosity at 25°C	6 mPa·s
11	Specific heat capacity (of liquid)	1.88 kJ/(kg·K)

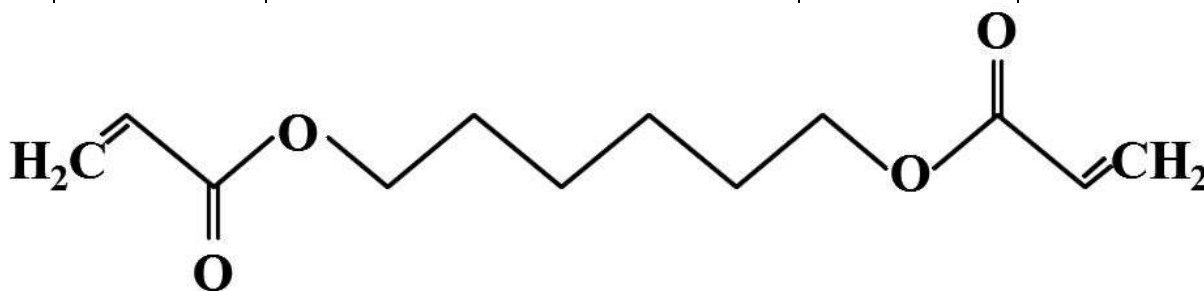


**Figure 4.3** 2D Structure of 1,6-HDDA

**Table 4.3** Properties of BEE Photo Initiator (Sigma Aldrich MSDS)

Sl. No.	Properties	Values
1	Molecular weight	240.3
2	Formula	C <sub>16</sub> H <sub>16</sub> O <sub>2</sub>
3	Appearance	White to off-white powder
4	Melting point	56-59°C
5	Boiling point	194-195°C
6	Refractive index	1.5727

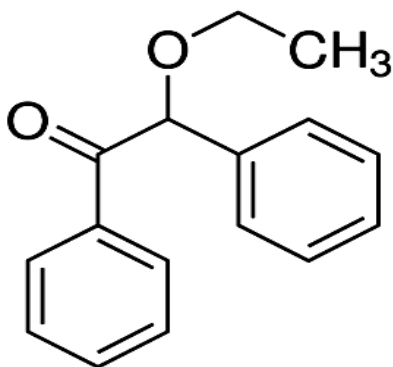


**Figure 4.4** 2D Structure of Benzoin Ethyl Ether

The monomer (4-5 ml) was placed in a round bottom flask of 25 ml size, carefully measured by using a micropipette of 0.001 least count and quickly transferred to the flask covered with aluminium foil. The precursor for photo polymerisation was prepared for different chemical proportions by varying the photo initiator concentration from 0.075% to 0.15% by weight in HDDA. The photo-curable solution was then stirred at room temperature in a dark environment created by aluminium wrap covering the flask for duration of two to three hours continuously for proper mixing of the resin.

Silicon wafer was used as a substrate material to develop structures in the present study because its surface properties are favourable to the process. DLC-coated silicon substrate and the uncoated silicon substrate were considered for the study to understand the interlayer bonding between the surface of substrate and sample. Preliminary studies show that uncoated silicon substrates showed high intra-surface

bonding between the substrate and the sample, making it difficult to remove the sample from the surface of the substrate. Also, for uncoated silicon substrate, effect of beam scattering was high in the fabricated mesh structure when observed for cured line width under confocal microscope. Effect of scattering and adhesion of fabricated layer over the surface of DLC-coated wafer were found to be negligible during processing. Hence, silicon wafer along with DLC coating of 300 nm layer thicknesses was considered to be a proper substrate material for use in the present work.

#### *Experimentation by scanning MSL*

In-house built scan-based MSL system, which works on the vector-by-vector scanning or raster scanning principle, was used for fabrication. This MSL system was not developed as a part of this research work. However, modification is carried out to fabricate microneedle. A control for AOM was introduced to vary the power of the laser. The major components are Argon ion laser, XYZ stage, acoustic optic modulator (AOM), and optics for beam expanding, directing and focusing. The schematic diagram is shown in Figure 4.5.

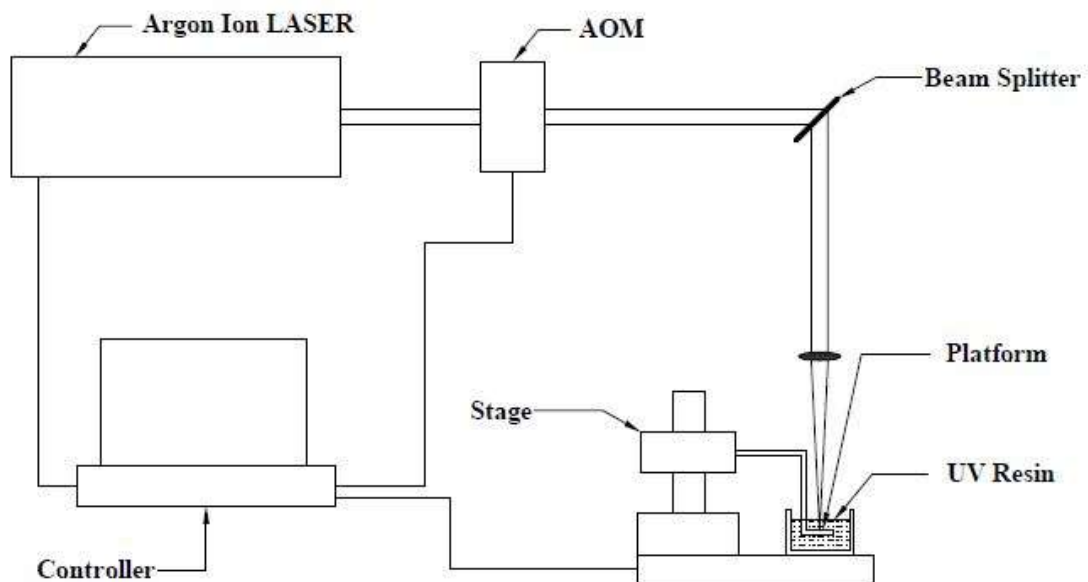


**Figure 4.5** Schematic Diagram of MSL Setup

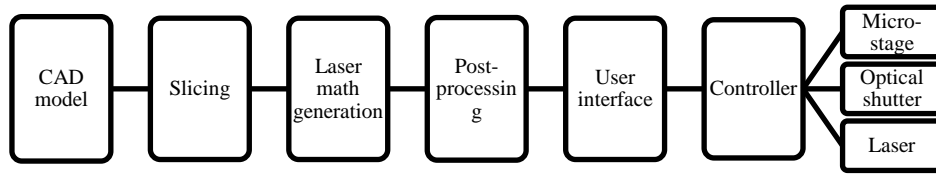


**Figure 4.6** Structure of MSL Process

Figure 4.6 shows the structure of the MSL for building up a set up for experimentation. The setup was built on a Newport isolation table as can be seen in Figure 4.7. Lab View program of National Instruments was used to control the system components. Graphic user interface (GUI) was used to interface the motion controller with numerical code generated using Unigraphics NX5 CAD software.



**Figure 4.7** MSL Setup



**Figure 4.8** Schematic Diagram of Micro-stage, Petri Dish and Focused UV Light

An argon ion laser source system operates wavelength in range 333.1-364 nm and maximum current of 60 A. However, the wavelength was set to 363 nm. Precision linear positioning stage with 0.1  $\mu\text{m}$  resolution in X-Y-Z stages (Figure 4.8) enabled precision scanning of laser beam over the photo curable monomer. Beam delivery system consisted of acoustic optic modulator, aperture, beam expander, mirrors and focusing lens. Acoustic optic modulator with system driver and crystal controlled oscillator was used as switch to control the state of beam. Focusing optics and beam expander were essential to obtain small laser spot size. A fixture assembly was attached to linear positioning stage to hold Si substrate rigidly to get uniform layer thickness in the multi-layered microstructure. CAD design tool provided 3D model design of micro-parts, slicing and NC program generation.

The CLS file was post-processed to get NC file that consists of X&Y coordinates. The post-processor developed indigenously was configured to control acoustic modulator and linear stage. The CLS file was then post-processed using the developed post-processor such that an NC file was readable by the developed Lab View interface. All NC files so generated in case of multi-slice operation were combined to form a single program and transferred to the machine through the interface created using Lab View environment.

Fabrication of individual devices can be accomplished in a few hours. A complex 3D object was separated into general 2D objects or slices. The slices were physically realised by focusing laser beam on a UV curable region. Polymerisation occurs layer by layer when beam was focused on the monomer.

#### *Step-less fabrication of microneedles by MSL*

In micro-additive manufacturing, in general, the parts are fabricated layer by layer. When the parts are fabricated layer by layer, steps form at the interface of the layers. Step height depends on layer thickness. Smaller the step height, smaller would be the step, whereas the time taken for processing would be more. Again there is a minimum limit for step height, and it depends on stage accuracy in Z direction, laser beam spot diameter and laser intensity. To get step-less features on microneedle, a novel method

has been found out and used for fabrication. The following paragraphs explain such method of fabrication.

Curing width and curing depth are two important parameters with which size and shape of microneedle could be controlled.

The formula for curing width is given by the equation (O. Dufaud and S. Corbel, 2003).

$$L_w = B \frac{C_d}{2 D_p} \quad \text{Eqn. 4.1}$$

where,

B - Spot diameter

C<sub>d</sub> - Curing Depth

D<sub>p</sub> - Penetration depth (at which the beam intensity is reduced to 1/e of its surface value)

By having control over the spot diameter, curing width was controlled apart from having control over curing depth. Cured depth for the Gaussian intensity profile laser was predicted by using classical Beer Lambert's law of light propagation in absorbing media ((Varadan et al., 2001).

$$C_d = D_p \ln \frac{E_{\max}}{E_c} \quad \text{Eqn.4.2}$$

where,

C<sub>d</sub> - Cured depth

D<sub>p</sub> - Penetration depth of the resin

E<sub>c</sub> - Critical energy of the resin

E<sub>max</sub> - Maximum energy

From the above equation, it was found that the curing depth could be controlled by varying the energy exposure. MSL set up has been modified for this purpose. By varying the voltage input to the AOM, output power of the laser is changed. 4<sup>th</sup> Axis facility available in the MSL controller is used in this experimentation. Other way is

to control the curing depth was through varying the scanning depth. Parameters used for fabrication are given in Table 4.4.

**Table 4.4** Power of the Laser Beam, Voltage and Focal Distance

Sl. No.	Voltage, V	Power, mW	Vertical distance of focal point from the base, $\mu\text{m}$
1	1	8	10
2	0.9	7	20
3	0.8	6	30
4	0.7	5	40
5	0.6	4	50
6	0.5	3	60
7	0.4	2	70
8	0.3	1	80
9	0.2	0.5	90
10	0.1	0	100

A controller controlled the Z motion of the stage and laser intensity through the acoustic optic modulator. By varying the intensity of the laser beam while the stage was lowered vertically, the beam spot was varied and proportionately the curing width and curing depth was reduced.

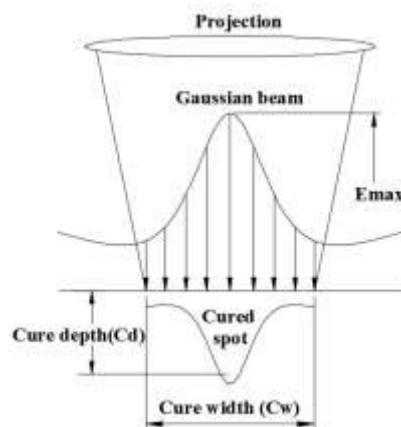


**Figure 4.9** Gaussian Beam Profile

It was demonstrated that the HDDA microneedles could be fabricated using MSL process.

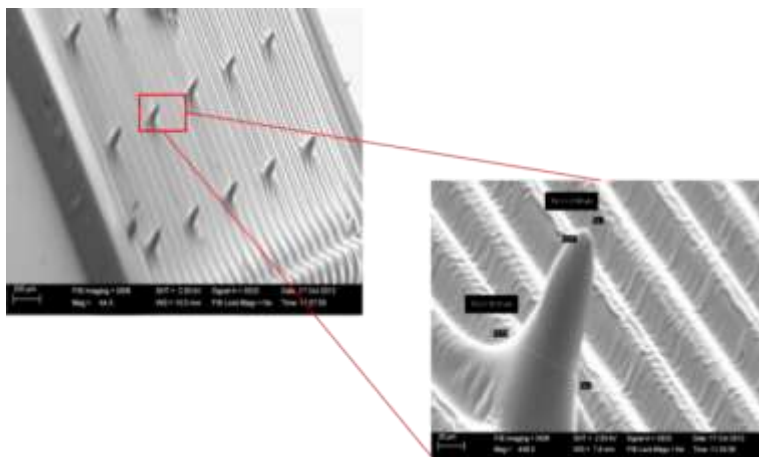


**Figure 4.10** Microneedles Fabricated by Varying the Intensity

**Table 4.5** Dimensions of Fabricated Microneedles

Sl. No.	Microneedle Parameters	Dimensions
1	Base diameter	Ø60 µm
2	Tip diameter	Ø3.75 µm
3	Height	110 µm

Microneedles have been fabricated by exposing the resin consisting of monomer, HDDA and initiator, BEE by vertically scanning and at the same time varying the laser power intensity using acoustic optic modulator. The results obtained showed novel way of achieving features of micro-size without any step. Table 4.5 gives the dimensions achieved by this process.

#### *UV curing of MMA*

Microneedles have been successfully fabricated using HDDA material. HDDA is not biocompatible and does not have the strength as that of PMMA. Whereas, PMMA is biocompatible material. Its curing aspects had to be studied.

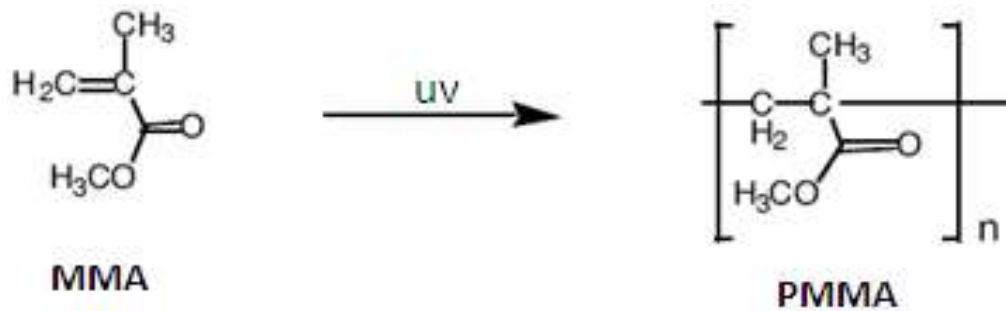


**Figure 4.11** MMA Photo Polymerisation

Percentage of initiator (BEE) required for adding to MMA monomer had to be found out by conducting experiments.

There are many photo curable resins that absorb different wavelengths. UV radiation is most widely used in photo polymerisation because it involves low temperature curing and also it is economical and simple to produce UV radiation. Photo polymerisation reaction of MMA monomer in the presence of BEE as photo initiator is illustrated in Figure 4.11.

PMMA, among polymers possesses a remarkable combination of useful properties, including versatility in forming, excellent clarity, colour stability to light and heating, and moderately high softening temperature, which makes it the best synthetic glass-like plastics. The cured photopolymers applicability is assessed by its dimensional properties such as accuracy and dimensional stability along with physical and mechanical properties. These properties mainly depend on selected photo resins, PI and process parameters.

*Experimentation to cure MMA by UV light source*

Experimental work on MMA photo polymerisation was carried out with setup comprising equipment like UV LED (Hamamatsu) light source shown in figure operating at 368 nm, 10 W power with focal length of 10 mm as shown in Figure 4.12.

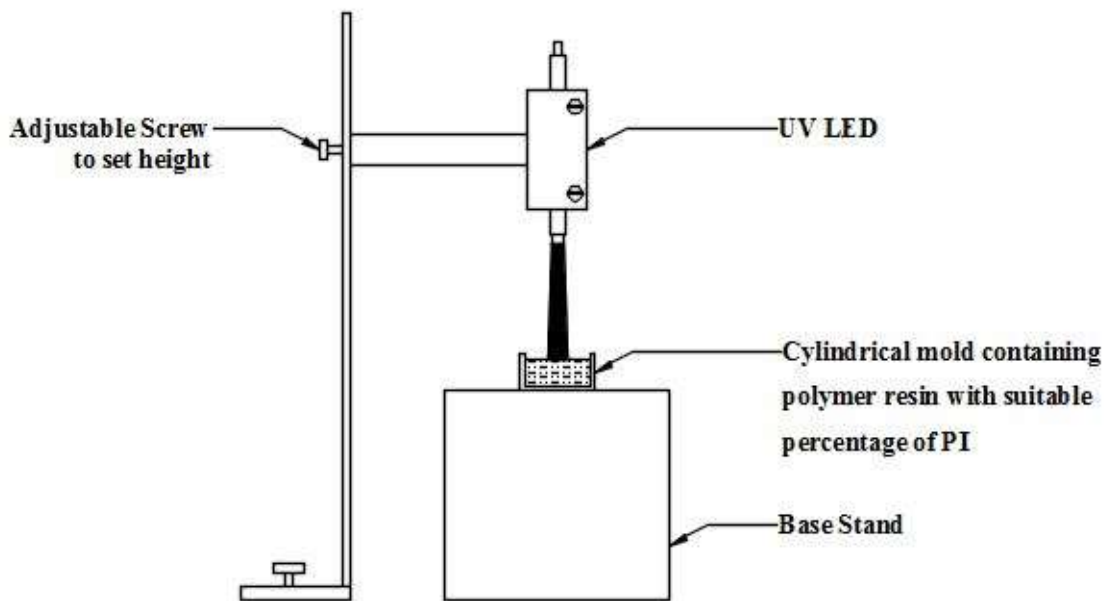


**Figure 4.12** Schematic Diagram of UV LED Lamp Setup

The experimentation involved preparation of photo resin formulation by mixing MMA monomer (Sigma Aldrich) with different concentration of Benzoin Ethyl Ether (Alfa Aesar) as PI and exposing each formulation to UV radiation for varying time duration. Mold filled with resin is cured under UV exposure for different duration.

*Experimentation to cure MMA by UV laser source*

Monomer MMA with BEE of suitable proportion was mixed, and MSL system was used to cure the mixture. Maximum power of laser was used by setting maximum voltage to acoustic optic modulator. 3D model was divided into layer by layer using Unigraphics CAD module. Laser path was generated as line by line, and same was translated into XY motion using microcontroller integrated using National Instruments (NI) interface. Polymerisation did not happen due to lack of power available with the 365 nm laser. Experiments conducted by varying intensity while moving the stage also did not yield polymerisation due to lack of power available with the UV laser.

### *Experimentation to co-polymerise 1,6 HDDA and PMMA using UV light source*

When two or more different monomers unite together to polymerise, their result is called a co-polymer and its process is called co-polymerisation. Here, two monomers HDDA and MMA are considered for co-polymerisation.

The precursor was prepared by adding optimal amount of BEE (1.5% by wt.) into mixture of 1,6 HDDA (75%) & MMA (25%), magnetic stirred at room temperature in the dark for a duration of two to three hours continuously for uniformity of the mixture.

The mixture is filled into petri dish having a work platform immersed in it. The work platform is attached to XYZ micro-stage. Intensity of the laser was set using a command in the program. Microneedle CAD model is sliced into layers and for each layer, tool path was generated using Unigraphics CAD/CAM software. The post-processed program was fed to the Lab View environment for controlling the micro-stage and acousto-optic modulator.

Simple rectangular blocks were fabricated with above-said precursor at feed rate 0.5, 1.0, 1.5 mm s<sup>-1</sup> on MSL. Later the samples were analysed using FTIR spectroscopy technique to find out MMA and HDDA in the fabricated sample.

### *FTIR spectra of standard samples*

Before carrying out experimentation on co-polymerisation, standard samples of HDDA, PMMA, BEE and co-polymerised HDDA and PMMA were characterised using FTIR to get their stretching frequencies. The results of FTIR spectra of samples are presented and discussed in Chapter 5.

#### 4.2.2 Microneedle by Micromolding

MMA (liquid monomer for PMMA-Biocompatible material) was used in MSL for microneedle array fabrication on laser-based MSL but was unsuccessful due to its process incompatibility.

Microneedles have been fabricated by combining micromachining and injection moulding with microneedle dimensions being around 500  $\mu\text{m}$  tall and 25  $\mu\text{m}$  tip diameter by Jordan (2010). The present work focused on fabrication of PDMS microneedles preferably shorter than 250  $\mu\text{m}$  after understanding the skin anatomy for ensuring minimal interaction of microneedles with nerves in dermis layer for pain-free application.

PDMS has been used to prepare microneedle mould because it has the following properties.

- Low surface energy (21.6 dyne/cm)
- Chemically inert
- Non-hygroscopic
- Good thermal stability
- Optically transparent down to wavelengths of  $\sim 300$  nm, mechanically durable
- Low cost
- Elastomer with 0.5 MPa Young's modulus
- Low adhesion to facilitate separation of microstructures from micro moulds
- Ability to conformal coating of microstructures and fill micro moulds

The fabrication methodology involved grinding custom carbide tools followed by using these micro-tools for creating micro-hole array in mould and finally PDMS casting.

Focus was to design and manufacture tungsten carbide micro-tools with the objective to reflect tool dimension on final microneedle structure to be fabricated. Two different types of tools have been ground with one for drilling and other for indenting operation. Micro-tools were ground for this purpose using conventional EWAG, Precision Tool Grinder (WS11, EWAG, Etziken, Switzerland) with built-in 40X measuring microscope (Figure 4.13). Silicon carbide cylindrical rods with 3 mm diameter shank were chosen for making micro-tools.



**Figure 4.13** Precision Tool Grinder

The tools were ground in  $24^\circ$  conical form on one end as shown in Figure 4.14 using diamond grinding wheel. Out of two types of conical tools ground, one tool is provided with additional relief for chip flow for drilling operation.



**Figure 4.14** Carbide Micro-Indenter and Micro-Drill

Tools were measured using profile projector for included angle of  $24^\circ$  and tip diameter was found to be  $\approx 21\text{-}22\ \mu\text{m}$  with grinding wheel grit size being the limitation for any further reduction in size. Tools were made by using a cutting speed of  $942\ \text{m/min}$  and depth of cut of  $20\ \mu\text{m}$  for roughing and a cutting speed of  $1143\ \text{m/min}$  and  $3\ \mu\text{m}$  for finishing.

In general, the micromolding process consists of master structure fabrication, negative mould fabrication, casting and separation. Figure 4.15 shows the sequence of process involved in micro molding.

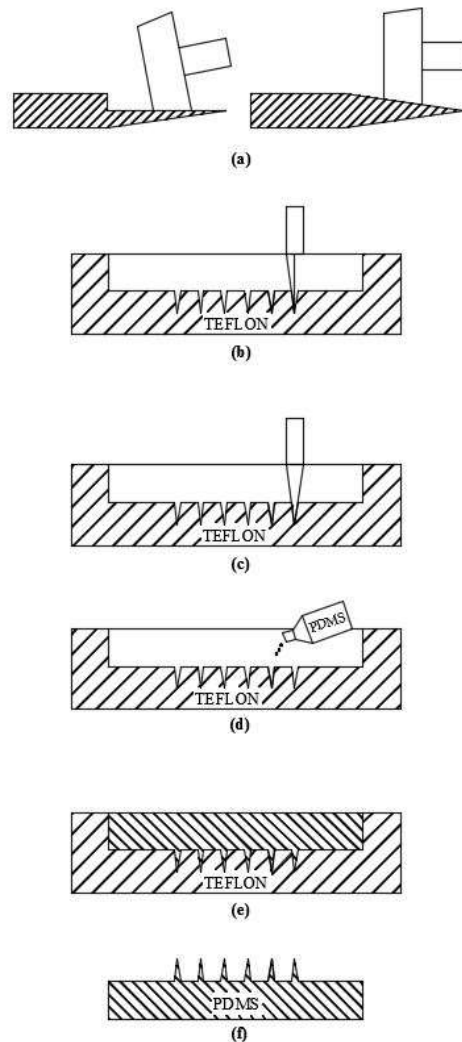


**Figure 4.15** Micromolding: a) Micro-Tool Grinding, b) Micro-Hole Drilling, c) Indentation, d) PDMS Casting, e) PDMS Curing f) PDMS Microneedle Array

In the conventional molding process, direct casting of a variety of polymers into the mould is performed to complete the process. Advances in micromolding technology and material science now make possible a range of cost-effective alternatives for components that are miniature, complex, and require high-precision tolerances.

Teflon was selected as mould material due to its softness and ease in machining. Teflon mould selected as shown in Figure 4.16 had pre-machined to 10 mm diameter and 2 mm deep slot. Micro-drilling operation was carried out using Ultra Precision Micromachining Centre (Kern Evo, Kern Microtechnik, Eshenlohe, Germany) for making 10×10 array 220  $\mu\text{m}$  deep holes in 10 mm slot in teflon mold (Figure 4.16) with distance between two adjacent microneedles being 400  $\mu\text{m}$ . The process parameters chosen for machining are presented in Table 4.6. During machining, water-soluble coolant was used particularly to reduce thermal expansion problem resulting from high spindle rotational speed.



**Figure 4.16** Micro-Holes Drilling on Micromachining Centre

PDMS was chosen as casting material since it had been widely demonstrated to replicate high aspect ratio microstructures with very good accuracy and also easy separation from mould.

**Table 4.6** Micromachining Process Parameters

Process Parameters	Drilling	Indentation
Depth of cut ( $\mu\text{m}$ )	10	220
Spindle rotational speed (rpm)	8,000	-
Feed (mm/min)	5	20

PDMS offered greater flexibility in deciding on curing temperature to suit with the functional polymer to be casted later during replication. Low viscosity curable PDMS is a commonly used silicon elastomer in micro-fabrication as demonstrated by Yu et al. (1996) and Jones et al. (2000). It is highly flexible, chemically and thermally stable, and biocompatible. It is also well-known as an excellent soft material for soft-lithography, especially in biological and medical usage, due to a number of reasons as described by McDonald et al. (2000).

For micromold casting, PDMS pre-polymer (Sylgard 184, Dow Corning) was used in mixing weight ratio 10:1. Binder and elastomer was thoroughly mixed and filled into Teflon mould, which is a negative mould of microneedle array. The mould was degreased at 20 inch of Hg vacuum in a vacuum desiccator for one hour mainly for removing entrapped air in micro-holes to facilitate proper mould filling. Subsequently, uncured PDMS-filled Teflon mould was placed in oven maintained at 100°C for one hour. PDMS-positive microneedle mould was gently demoulded from Teflon mould. Experimentation conducted to fabricate PMMA micro needle from PDMS mould. Due to adhesion of PMMA to PDMS mould material, fabrication of micro needle was not realised.

### **4.2.3 Micromilling of Microneedles**

To carry out microneedle machining, a precision micromachining centre (Kern Evo, Kern Micro and Feinwerktechnik, Germany) was considered. Microneedle was modelled using Solid Works 2014 and then imported to Unigraphics (Version NX 7.5) CAD/CAM software for generating tool path for machining microneedle. Figure

4.17 shows the flow chart of microneedle fabrication from modelling to product testing.

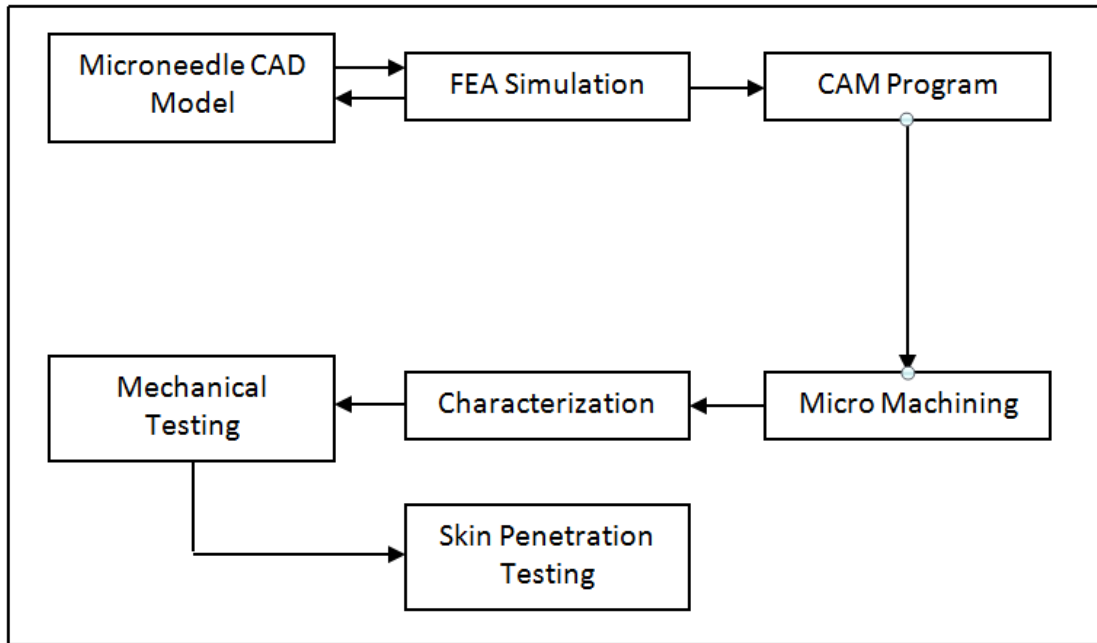


**Figure 4.17** Block Diagram for Micromachining

CAD model made using solid works is shown in Figure 4.18. Features like extrude feature, linear array were used to model the microneedle array. CAD modelling was done by drawing circle of 10 mm diameter in sketch tab, extruding sketch up to 2 mm in feature tab, drawing microneedle array using linear array option in sketch tab and then extruding microneedle sketch up to 0.2 mm with draft angle.

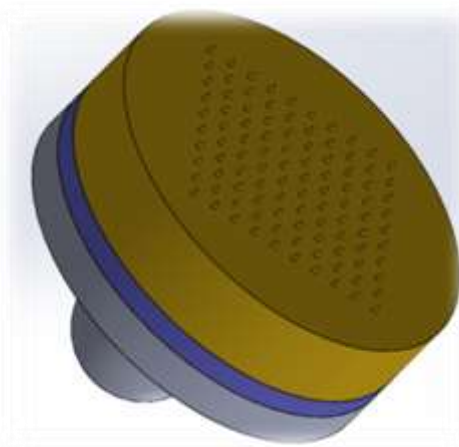


**Figure 4.18** CAD Model of Microneedle Array

PMMA raw material dimension of 10 mm diameter and 2 mm was considered as blank. Microneedles of tip diameter, 5  $\mu\text{m}$ , base diameter, 120  $\mu\text{m}$ , height of 200  $\mu\text{m}$  and pitch of 400  $\mu\text{m}$  were optimised in the previous chapter of design analysis and same were considered for machining.

Unigraphics NX 7.5 was used for generating Tool Path generation. Initially the tool path was generated to machine the top surface, so that tips of all the microneedles were made to be in same plane. Secondly, tool path was generated for machining outer area of the microneedle. Tool of 1 mm was used for face milling. Tool diameter of 0.2 mm was selected for microneedle machining, based on pitch distance of 0.4  $\mu\text{m}$  between the needles and a base diameter of 120  $\mu\text{m}$  of the microneedle. Sequence of arriving at final tool path starts with modelling the microneedle patch and importing CAD model (.SLDPRT) file to Unigraphics CAD/CAM workstation. Initially, work offset was set to make top surface to zero (for generated program) and then manufacturing module was started by assigning work co-ordinate to machine co-ordinate.

CNC tool path generation sequence involves selection of 3D model of microneedle block, cut area and face at the bottom of microneedles to indicate depth of cut. Further, tool path generation involves selection of tool path as follow part, setting of 2  $\mu\text{m}$  depth of cut for initial 10  $\mu\text{m}$  height, selecting tolerance as 1  $\mu\text{m}$  in stock option in cutting parameters and selection of plunge and clearance 3 mm in non-cutting parameters. Postprocessor of Kern Micro machining centre that is already available was used. Finally, Series of processes like face milling and end milling were performed.

Table 4.7 gives the details of cutting tools used for face milling and for micromilling of needles. Figure 4.19 shows the micro end mill used for machining.

**Table 4.7** Cutting Tool Data for Face Milling

Sl. No.	Parameter	Value
1	Tool diameter	1 mm
2	Flute length	3 mm
3	No. of flutes	2
4	Material	Tungsten carbide



**Figure 4.19** End Mill ( $\varnothing 0.2$  mm) for Micromilling

**Table 4.8** Cutting Tool Data for Micromilling of Needles

Sl. No.	Parameter	Value
1	Tool diameter	0.2 mm
2	Flute length	0.9 mm
3	No. of flutes	2
4	Material	Tungsten carbide

*Process parameters for face milling*

Face milling was required to ensure that tip of all the microneedles were in one plane.

Process parameters used for face milling are given in the following Table 4.9.

**Table 4.9** Process Parameters for Face Milling

Sl. No.	Parameter	Value
1	Feed	100 mm/min
2	Depth of cut	1 $\mu\text{m}$
3	Rotational speed	5,000 rpm
5	Coolant	Water-soluble oil
6	Profile tolerance	10 $\mu\text{m}$

*Process parameters for micromilling of needles.*

Strategy for simulation of micromilling was divided into multiple stages. As the tip diameter is small, i.e., 5  $\mu\text{m}$ , smaller depth of cut of 2  $\mu\text{m}$  was considered up to a depth of 10  $\mu\text{m}$  for milling of microneedles. 10  $\mu\text{m}$  depth cut was considered for remaining depth of 190  $\mu\text{m}$ . Process parameters used for face milling are listed in Table 4.10.

**Table 4.10** Process Parameters for Micromilling of Needles

Sl. No.	Parameter	Value
1	Feed	100 mm/min
2	Depth of cut	2 $\mu\text{m}$ for 10 $\mu\text{m}$ , 10 $\mu\text{m}$ for 190 $\mu\text{m}$
3	Rotational speed	16,000 rpm
4	MM/tooth	0.003
5	Coolant	Water-soluble oil
6	Profile tolerance	1 $\mu\text{m}$

Machining simulation of surface external of microneedle with  $\varnothing 1$  mm end mill is depicted in Figure 4.20.

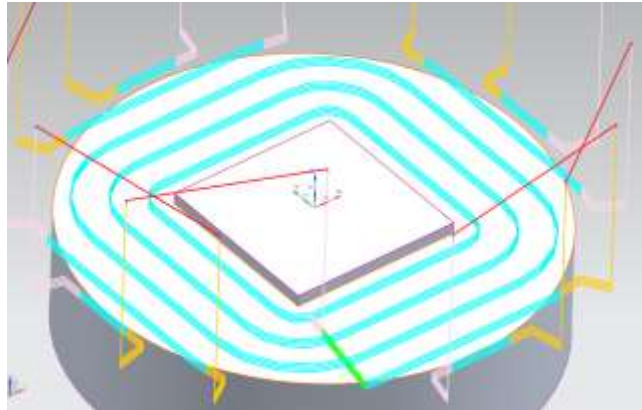


**Figure 4.20** Tool Paths for Removal of External Surface

*CAM for micromachining*

Figures 4.20 to 4.22 show simulation of tool path. Work reference was set the centre of the microneedle block before starting of simulation. Initially, face milling operation was carried out to ensure flatness.

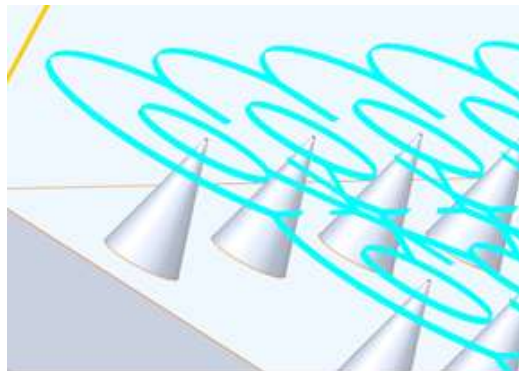


**Figure 4.21** Simulation of Tool Path

Figure 4.22 shows the tool path generated wherein the entire length of microneedle was divided into 24 layers, and each layer was machined completely before proceeding to next layer. Machining of 2  $\mu\text{m}$  layer machining initially ensured lower cutting loads on the surface of microneedle, which ensured microneedle to retain sharp tip and also the surface to be smoother.

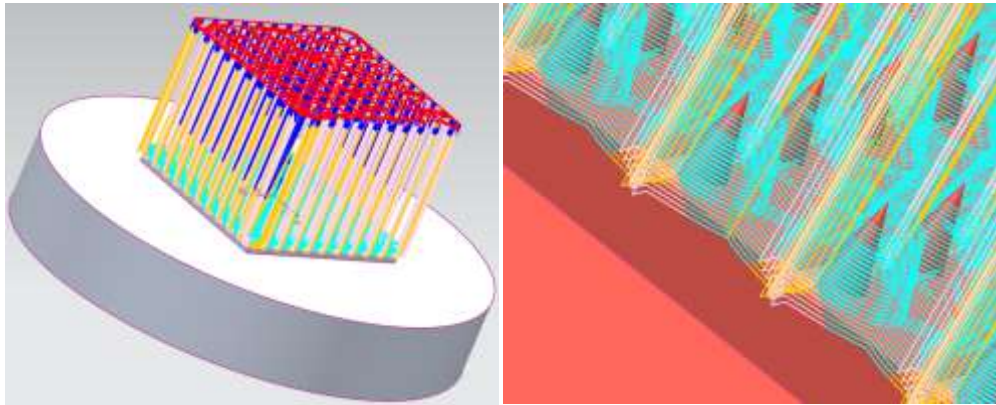


**Figure 4.22** Simulation of Tool Path for Machining Microneedle  
(Layers with 10  $\mu\text{m}$  depth of cut below fine layers)

#### *CNC program*

Cutter line (CL) data was the output from simulation. As the microneedle was planned to be machined on Kern Ultra Precision 5 Axis micromachining centre with Heidenhain control system, the post processor of this machine was used to process the CL data to get CNC program. CNC Program generated was transferred to Kern Machine controller using DNC mode available in the machine. CNC Programs thus generated for face machining and for microneedle micromachining were used.

#### *Micromilling*

Micromilling is relatively a simple, fast and cost-effective way to realise complex structures irrespective of material involved. Micromilling process requires the use of high-speed machining. Critical design parameters to be considered in micromilling machine are positioning accuracy, spindle run out, spindle rotational speed, dynamic stiffness, vibration and thermal stability. To fabricate microstructures with high aspect ratio, form accuracy, dimension tolerances, the suitability of the machine may be decided based on the above-mentioned parameters. In present work, precision micromachining centre (Make: Kern; Model: Evo) shown in Figure 4.23 was used for micromilling microneedle.

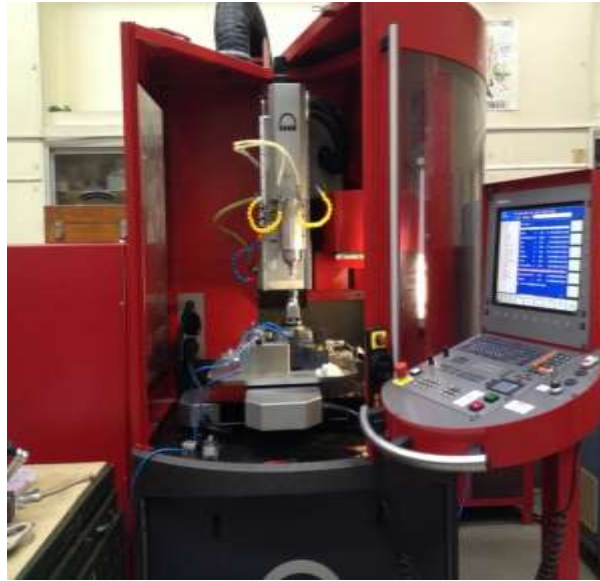


**Figure 4.23** Kern 5 Axis Micromachining Centre

The machine is fitted with direct drive to provide fast acceleration and feed rates, which are required for high-speed machining of microneedles. The machine is suitable for micro machining as it has features like very low compliance, high-speed machining capability, capability to give very low depth of cut and fast response.



**Figure 4.24** Microneedle Machining Setup With High-Speed Milling Spindle

Machine is made out of Epoxy-based composite material construction having rigidity 10 times that of cast iron. It can give a high precision of about  $\pm 0.5 \mu\text{m}$  according to VDI/DGQ 3441 on the workpiece. The micro machining centre has the features like spindle run out and repeatability less than  $1 \mu\text{m}$ .

PMMA rod of diameter 10 mm with 2 mm length was held using collet holder, which was held using pneumatically operated quick change clamping system. Tool was held using miniature collet holder having HSK taper shank to fit into Kern machine spindle taper. Tool diameter and length offsets are set by using vision-based tool setting device mounted on machine.

Micromilling is based on the mechanical removal of substrate materials. Process parameters such as spindle speed, depth of cut, feed rate and working environments affect the final surface quality of the micromilled substrate (Chen et al., 2014). Micromilling can be used to fabricate components directly or can be used to fabricate master, which can be used for replication by other processes (Chuan et al., 2014). In end milling process, the chip load varies during a single engagement of a tooth in the cut and the cutting mechanism may change from ploughing-dominated to shearing dominated and back to ploughing dominated again within a single excursion of a tooth through the cut. Furthermore, owing to the very small chip loads in micromachining, the well-known size effect plays a significant role.

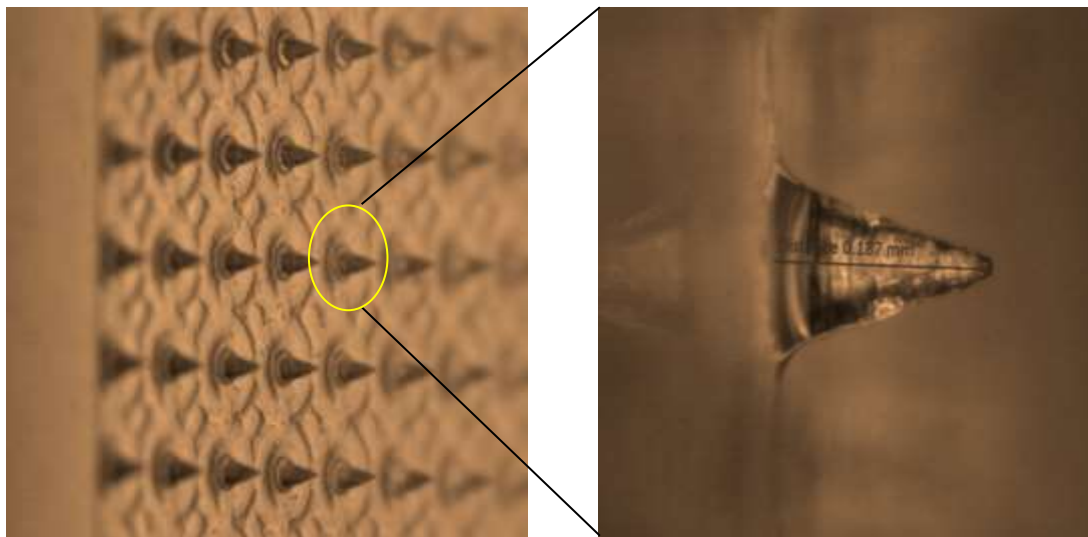


**Figure 4.25** Micromachined PMMA Microneedles

In microscale machining, where chip loads may range from submicron levels to a few microns and depths of cut may be in the range of a few microns to perhaps 100  $\mu\text{m}$ , the cut geometry and the grain sizes of the workpiece material are now comparable in size. If the chip load is of the same order or less than the edge radius of the tool, then

a chip may not be formed during each tooth passing. This phenomenon is known as the minimum chip thickness effect (Kim et al., 2002). The minimum thickness of cut might be on the order of 1/10 of the cutting edge radius (Ikawa et al., 1991). Compressed air is proven to be better coolant in delivering a better surface quality than the oil coolant, and depth of cut has the largest impact while the spindle speed has the minimised impact to the surface quality of a micromilled PMMA substrate (Chuan et al., 2014). The step over is one of the dominant factors affecting the machined surface roughness mostly (Jiao et al., 2014). The tool selection has critical role on machining accuracy and surface as the tendency of surface roughness results observed for Tungsten carbide tools is towards a lower roughness value with an increase in feed rate in comparison with single crystal diamond and CVD-coated tools (Jiao et al., 2014).

In present work, considering above reasons, Tungsten carbide micro-end mill tool with 3  $\mu\text{m}$  cutting edge radius was used to machine PMMA with 3  $\mu\text{m}$  chip load. Cutting speed used during machining was 1 m/min with 16,000 rpm. Figure 4.25 shows microneedle array fabricated by micromilling.

### **4.3 CONDUCTIVE COATING**

Microneedles need to be conductive to tap electric potential generated due to brain activity. As PMMA is electrically non-conductive, to acquire biopotential signals the surface of PMMA should be conductive; therefore, it is decided to coat a conductive layer on surface of PMMA having an optimal thickness with sufficient adhesion and surface conductivity. Coated surface needs to be characterised for adhesion and conductivity. Biopotential electrode functions as sensor that couples the ionic potentials generated inside the body to an electronic instrument. Biopotential electrode needs to conduct small current across the interface between the body and the electronic measuring circuit.

### 4.3.1 Electroless Silver Deposition

Among the many methods available for coating, electroplating method is cost-effective as the apparatus is simple and suitable for mass production. Electroless silver plating is highly conductive and biocompatible, even its oxide forms conductive unlike other metals. There are two categories.

First category, galvanic exchange deposition is suitable for metals and the second category, electroless deposition method, which uses reducing agents that could be used for depositing metals on polymer (Koura, 1990). Figure 4.26 shows Schematic representation of PMMA microneedle coated with silver (Ag).

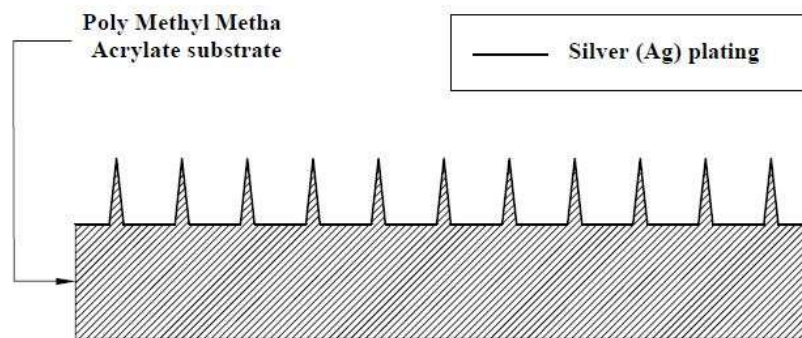


**Figure 4.26** Schematic Representation of PMMA Microneedle Coated With Silver

It is a Redox technique used to deposit a layer of silver on a solid surface. A reducing agent like aldehyde is used in the chemical process for depositing silver. The success of plating depends on pre-treatment process carried out on specimen.

PMMA sheet of thickness 10 mm was cut to 10 mm discs using CO<sub>2</sub> laser. The discs surface was ultrasonicated using distilled water. The surface was modified using 220, 500, and 1000 grade silicon carbide coated grit paper and the samples were named as a, b and c respectively. The procedure for coating of silver is by reducing ammonical silver nitrate solution using dextrose.

Figure 4.31 describes the reaction involved in silver deposition. For depositing silver, well known Tollen's Reagent is used.



Glucose (Aldehyde) + Tollen's Agent  $\rightarrow$  Carboxylic Acid + Silver + Water + Ammonia gas

#### Figure 4.27 Generic Reactions for Silver Deposition

Preparation of Tollen's Reagent: The transparent silver solution was prepared by dissolving  $\text{AgNO}_3$  (99.8%) in water with the addition of several drops of the aqueous ammonia (28-30%), then NaOH and finally several drops of aqueous ammonia were added until the solution turned to be transparent.

Reducing agent solution: The treated PMMA substrates were immersed in the aqueous solution of reducing agent, consisting of Dextrose ( $\text{C}_6\text{H}_{12}\text{O}_6$ ), and were stirred for duration of 10 minutes.

The mixture of PMMA and reducing agent was poured into the Tollen's Reagent and stirred for 60 minutes at room temperature. During the coating process, the pH was kept at 10-11. Dextrose was oxidised into its respective carboxylic acid, and Tollen's agent was reduced into silver, water and ammonia gas as shown in Figure 4.27. After washing and drying, the silver-plated PMMA substrates were obtained. The surface morphology of the substrates before and after coating of silver was studied using Carl Zeiss Stereomicroscopy (model: M2M). Powder X-ray diffraction (XRD) was used for the determination of crystal structure of the coated material over the polymer surface. XRD measurements were performed on Bruker D8 advance X ray diffractometer with Cu  $K\alpha$  radiation, ( $\lambda=1.5418\text{\AA}$ ) at a step size of  $0.033^\circ\text{s}^{-1}$  to determine the crystallinity of the sample. The variation in the surface Roughness of the sample was studied using Form Tally Surf (Taylor Hobson SGA series 2). This is a contact mode measurement where a stylus scans over the surface to measure the

surface roughness. The roughness (Ra) parameter before and after coating was also measured. The surface morphological and topography studies of the coated polymers were further studied using Carl Zeiss, FESEM (Model: Neon-40). In order to determine how well the coated silver substrates adhere to polymer, the generally used tape test based on the ASTM standard (ASTM D 3359-08) was performed by applying and removing pressure-sensitive tape over the silver coated polymer. The tape test is qualitative this will only give weather the adhesion is there are not. Though the test is qualitative but it is simple and moreover it provides rapid assessment of adhesion level.

The conductivity of the silver deposited on PMMA was measured using, four probe tester. Each tip is supported by springs on the end to minimize the damage during probing. A high impedance current source is used to supply current through the outer probes; a voltmeter measures the voltage across the inner two probes to determine the resistivity.

#### 4.4 PEEL OFF TEST FOR COATING

The peel off study was carried out using 3M scotch tape. The peel off study was done on silver-coated smooth and rough sample.

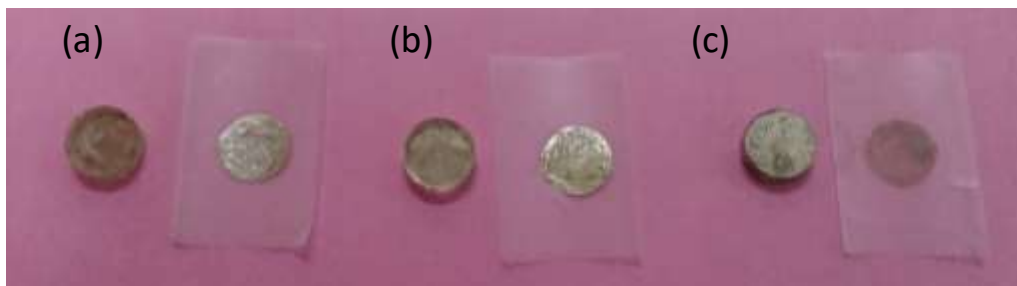


**Figure 4.28** Silver Coated Samples for Peel off Test: a), b) PMMA as Received  
c) PMMA After Roughened Out Using Abrasive Belt

The silver that was coated over the PMMA smooth sample was peeled off completely. Figure 4.28 (a) & (b) shows the peeled off samples. However, the silver coated on the rough sample adheres to the PMMA surface with the minimum peel off. Figure 4.32 (c) shows the adherence of coating on sample after the peel off test.

#### 4.5 COMPRESSION TEST FOR PMMA MICRONEEDLE

PMMA is a plastic material, and it is viscoelastic in nature. Mechanical properties depend on temperature and time (Milena, 2005). Plastics have significantly lower stiffness and much higher elastic limits compared with metals. PMMA has an elongation of 2 to 10%; ultimate strength of PMMA varies from 48 to 76 MPa, compressive strength of 80-110 MPa and hardness of 85-2015 HRM.

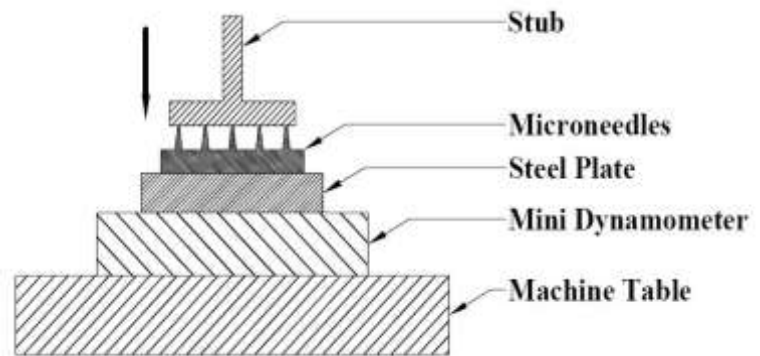


**Figure 4.29** Schematic Diagram of Compression Test of Microneedle



**Figure 4.30** Test Setup for Compression Test

Plastics have large amount of recoverable elastic strain. It can be more than 500%. In metals, the amount of recoverable elastic strain is less than 1%. Compressive strength for plastics is done using UTM. Compressive strength testing is done as per ASTM D695 and ISO 604 for plastics.

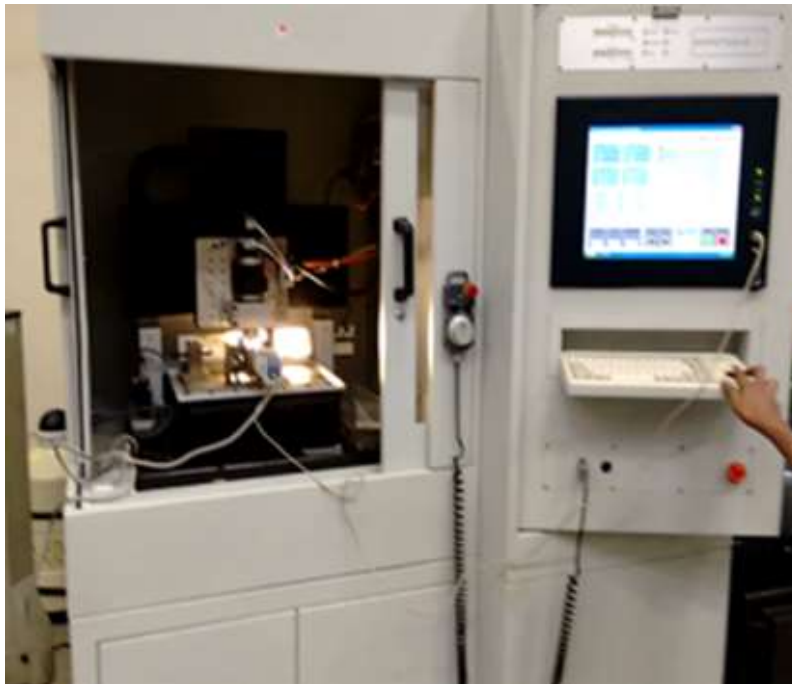


**Figure 4.31** Micro Machine Tool for Compression Test

As the minimum load that can be applied using UTM is 20 Nm and that of Micro UTM is 2 Nm, a special test setup was made on a multipurpose machine tool as shown in Figure 4.31. Camera attached to the setup (Figure 4.30) aids while doing experimentation with micro features.

The force required for fracture due to compression load was tested using multipurpose Micro machine tool (DT-110, Mikro Tools, Sg) with the aid of mini-dynamometer. Initially, patch with microneedle array was fixed using adhesives on a metal plate. Metal plate was mounted on top of mini-dynamometer (Model 9256C, Mini Dyn Multi component dynamometer, Kistler, Switzerland). Metal plate was precision ground to have a flatness value less than 5  $\mu\text{m}$  to ensure all the microneedles loaded at the same time.

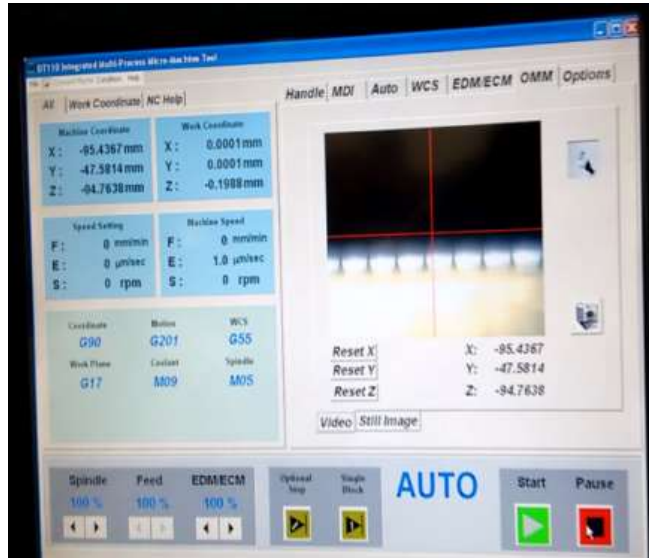


**Figure 4.32** Image of Microneedles Under Compression

Mini Dyn, a three-component dynamometer shown in Figure 4.33, was used for the dynamic and quasi-static measurement of the three orthogonal components of any force acting on the top plate ( $F_x$ ,  $F_y$  and  $F_z$ ).



**Figure 4.33** Mini Dyn Multi Component Dynamometer, Model 9256C, Kistler, Switzerland

The whole force measurement chain consists of piezoelectric-based mini-dynamometer, connecting cable, charge amplifier and a computer loaded with data acquisition and data analysis software (Dynoware).

Needle patch was aligned in such a way that its axis was in line with Z axis of the spindle of the micro machine tool. The whole setup was again fixed on a mini-dynamometer, which was again clamped on to worktable of micro machine tool. A steel stub was specially made to have provision for clamping on to the collet holder of the spindle of the micro machine tool.

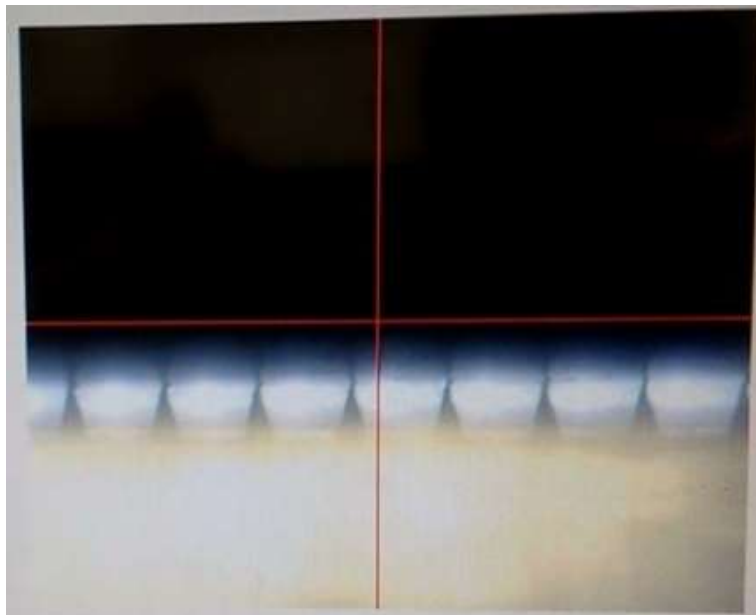


**Figure 4.34** Compression Image Captured Through Camera

Compressive load was applied by moving Z axis of the micro machine. Vertical axis was moved at the feed rate of 1  $\mu\text{m}/\text{sec}$ . The camera attached to the machine showed the deformation of the microneedle under load. Display of image captured through camera is shown in Figure 4.34, and Figure 4.35 shows the Scanning Electron Microscope (SEM) image of compressed needle. Mini-dynamometer measures the vertical force with respect to time. With the load being applied with known feed rate, needle deformation was found out based on feed rate.

As both the results were having force and deformation in time scale, a plot was correlated for load versus deformation.



**Figure 4.35** SEM Image of Compressed Microneedles

The test was done to find out the strength of the needle against the applied load by a steel stub. If the metal stub was replaced with a material similar to skin, then very less deformation can be expected.

#### **4.6 SHEAR TEST**

Microneedle array was subjected to shear load by fixing needle patch on mini-dynamometer mounted on DT-110 micro machine tool as shown in Figure 4.37 and 4.38. Needle patch was fixed in such a way that its axis was placed perpendicular to the Z axis of the spindle of the micro machine tool.

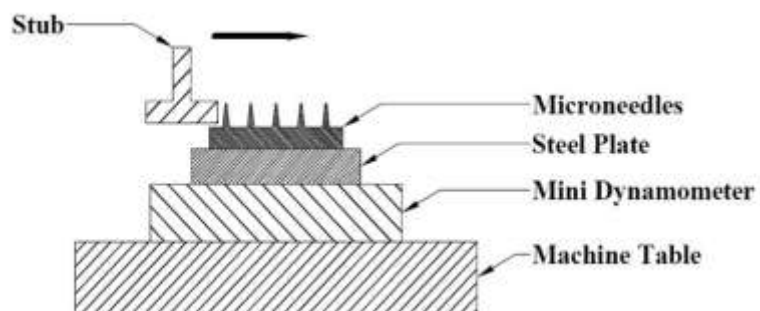


**Figure 4.36** Schematic Diagram of Shear Test of Microneedles



**Figure 4.37** Setup for Shear Test



**Figure 4.38** Needles Under Shear

Shear load was applied in the lateral direction by using stub that was moved by the X axis of the micro machine tool. Figure 4.42 shows the needles under shear. Since the needle array was  $10 \times 10$ , in the beginning, 10 microneedles of one column were subjected to shear load. Subsequent microneedles subjected to shear column-wise. Mini-dynamometer captured the resistance offered by the microneedle.

#### 4.7 INSERTION TEST

To carry out insertion test, setup is made on Mikro Machine Tool (DT-110), Mikro Tools, Sg., as shown in Figure 4.40. Figure 4.39 shows the schematic diagram of the performance of the insertion test. PMMA microneedles fabricated were inserted into PDMS and chicken skin, mimicking the micro needle insertion into the skin. Similar to human skin, chicken skin has epidermis, dermis and hypodermis layers. Outer layer of chicken has flattened, horny cell layer ([www.poultryhub.org](http://www.poultryhub.org)). However, chicken skin properties differ from human skin. Chicken skin has a Young's modulus of 4.13 MPa compared to 5 MPa for human skin. Hence, chicken skin is having higher strain than human skin. Tensile strength of the chicken skin is about 0.6 MPa (Charlotte Tsui, 2007). Tensile strength of human skin is about 0.5 MPa. As testing was done on fresh skin sample, cells are alive in the skin. Mini-dynamometer was used to measure the penetration force.

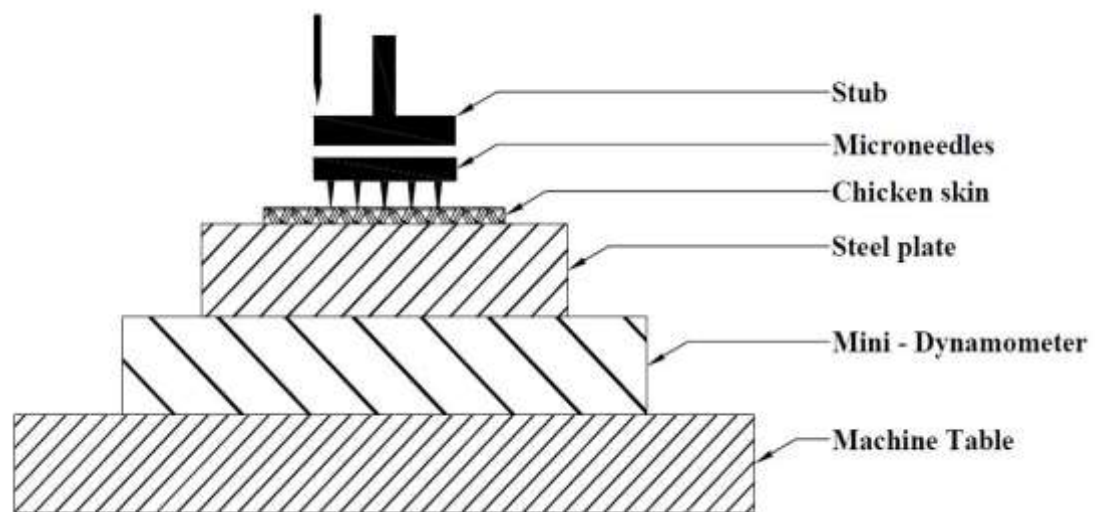


**Figure 4.39** Schematic Diagram of Test Setup for Piercing Chicken Skin Sample



**Figure 4.40** Test Setup for Piercing Chicken Skin by Microneedle

Feed for penetration was controlled by the Z axis of the micro machine tool. Needles were subjected to a load of 7.5 N for a penetration of 150  $\mu\text{m}$ .

#### **4.8 TEST FOR CONDUCTIVITY**

Satisfactory EEG signals determine the quality of the EEG electrodes. EEG electrodes are the means by which the electrical activity of the brain is communicated to the input circuit of amplifiers in the EEG machine. Fundamental requirement is that flow of ion within the brain has to become flow of electron within the electrode. In conventional cup type electrodes, electrolytes act as interface and at this interface flow ion is converted into flow of electrons.

When dry electrodes inserted into skin, push and pull of ions acting on the dry electrodes create potential difference in electrodes in contact. To measure the potential difference, the electrodes need to be electrically conductive. PMMA micro needle patch coated with silver was used for checking the conductivity. Skin-electrode contact impedance is an important parameter that will affect the quality of EEG recording ( Vanlerberghe et al., 2011). Impedance is measured by applying a small external voltage to the electrodes and then measuring the amount of current flowing in the circuit formed between the leads. Typically, the measurement is made by using a

10 to 30 Hz AC signal, which is well within the range of EEG signal frequency spectrum. Surface electrodes are expected to have an impedance value of less than 5 k Ohms.



**Figure 4.41** Electrical Resistance Measurement Using Multimeter

A simple test is carried out using multi-meter to check the resistance offered by the micro needle. Figure 4.41 shows electrical resistance measurement using Multimeter. The resistance values varied from 6.5  $\Omega$  to 11.8  $\Omega$  when tested at the top of the surface. Hegde et al., 2013 had reported variation in electrode resistance from 200  $\Omega$  to 1  $\Omega$ . It is preferred to have needles with as much as less electrical resistance.

#### **4.9 SUMMARY**

The chapter describes the various experiments conducted to realise microneedle. Experiments performed using scan-based MSL setup, micromolding and micromachining facilities are presented.

Using scan-based MSL system, microneedles are fabricated in a novel way. Innovative method of fabrication of microneedle using step-less process by MSL system is explained. Using micro stereolithography system, it has been testified that HDDA microneedle of very fine tip diameter of less than 5  $\mu\text{m}$  was achieved. Step-less fabrication is new technique and is expected to be very useful in additive manufacturing.

Experiments were conducted to optimise composition of MMA monomer and BEE initiator. Experimental results testify the use of 4 % BEE initiator for polymerisation

of MMA. This composition curing resulted in maximum hardness of 0.13 GPa and maximum Young's Modulus of 4.2 GPa

Experiments were conducted to co-polymerise HDDA and PMMA. FTIR spectroscopy shows stretching frequency of HDDA only. Co-polymerisation had not happened. This could be due to low reactivity of PMMA.

To realise microneedle by micro moulding, hybrid approach of combination of micro milling and micro moulding was attempted. PDMS master mould was taken out from positive Teflon fabricated using micro milling. However, due to adhesion of PMMA with PDMS master mould, it was not possible to realise microneedle.

Finally, micro milling method was used to machine micro needles. Micro machine tool was used to fabricate micro needle. Challenge of achieving finer tip diameter of 10  $\mu\text{m}$  was met by adopting layer by layer machining and varying the cutting conditions at each of the layer. It is observed that there is not much deviation in base diameter. Variation in length is less than 5% and the tip diameter is around 10  $\mu\text{m}$ .

Electroless silver plating was carried out to make PMMA microneedle electrically conductive. XRD results confirm the presence of silver on coated samples. Further, the samples were coated with gold by sputtering. Samples were tested for electrical resistance and it was measured to be 6.5  $\Omega$  to 11.8  $\Omega$ . A resistance value of around 10  $\Omega$  is considered to be satisfactory for acquiring EEG signals.

Compression and Shear test were conducted using micro machine tool with the aid of mini dynamometer. Experiments demonstrate that the microneedles deformed to 25  $\mu\text{m}$  for a load of 4 N. At 0.5 N shear load, needles failed. It testifies the microneedles are comparatively weak in shear.

Results of insertion tests conducted on chicken skin show that at 3 N force, the needles penetrated to a depth of 120  $\mu\text{m}$ . Results show that insertion force is sufficiently low for insertion by hand.

## CHAPTER 5

### RESULTS AND DISCUSSION

The investigations made in the previous chapters give a thorough insight into the various aspects related to development of microneedles. In there, design of microneedles, analysis and experimental studies were carried out. Experiments were carried out to develop micro needles by copolymerisation, micro molding and micro machining. In this chapter, results of FEA, experimental results of copolymerisation, compression test, shear test, chicken penetration test are presented and discussed. All the observations made during the experimentation in analysing the development of microneedle are summarised in the current chapter.

#### 5.1 RESULTS OF FEM ANALYSIS

FEM analysis was carried out to simulate PMMA microneedle skin penetration. The desired result is that penetration depth must be higher and needle strain must be lower during penetration. It is required for microneedle to penetrate more than  $120\mu\text{m}$  depth into epidermis (live skin tissue) to acquire low impedance signal. The data was analyzed for design of microneedle array to have lower strain while penetrating skin for about  $120\mu\text{m}$ . Figure 5.1 shows the simulation model before and after simulation.

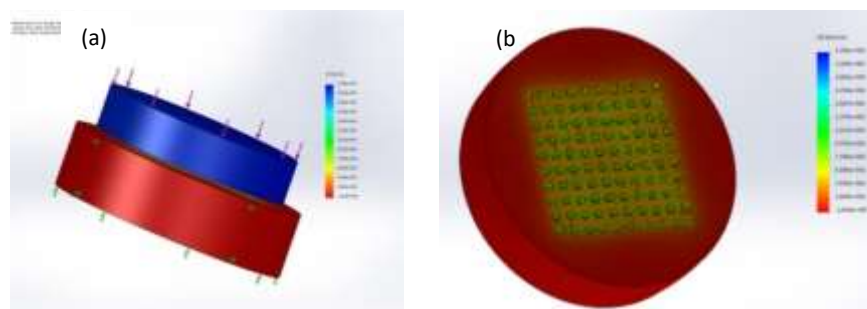


**Figure 5.1** FEM analysis-PMMA Microneedle Skin Penetration (a) Microneedle Penetrating Skin. (b) Punctured Skin After Penetration

Total number of iterations/alternatives considered in designing was 48 but only 6 alternatives mentioned in table 5.1 were shortlisted considering strain below 7%. Results of FEM analysis of skin penetration and needle strain for various other alternatives are given in Appendix I and II.

**Table 5.1** FEA Input Parameters and The Results

Sl. No.	Load(N)	Base Dia (mm)	Needle Pitch (mm)	Penetration (mm)	Strain
1	6	0.12	0.4	0.116	0.051
2	6	0.12	0.6	0.118	0.068
3	8	0.12	0.4	0.154	0.068
4	9	0.06	0.4	0.115	0.068
5	9	0.06	0.6	0.165	0.070
6	10	0.12	0.4	0.129	0.062

In the simulation study, it was observed that increase in load leads to increase in strain and penetration of the microneedle array.

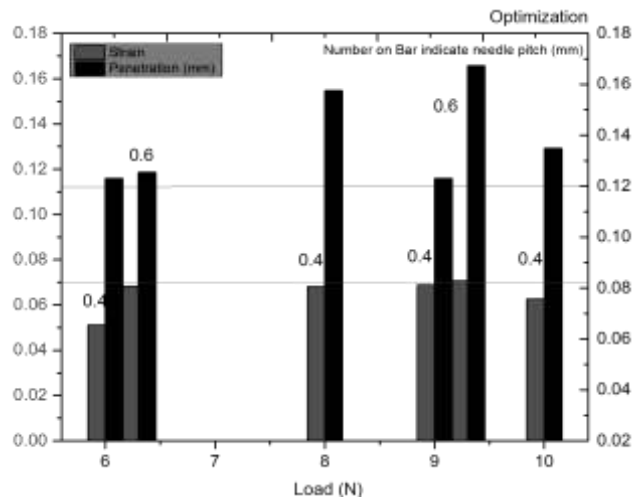


**Figure 5.2** Load Vs. Strain & Penetration

As the base diameter increased, strain was found to be less with a reduction in needle penetration. Beyond certain value, the penetration of the needle increases, due to

increase in compressive strength of the needle. Figure 5.2 shows the selected results for pitches for which the penetration is more and the strain is less. Among the selected results, for a pitch of 0.4 mm, a minimum strain and penetration value more than 120  $\mu\text{m}$  was observed.

## **5.2 OPTIMISATION OF PARAMETERS FOR PMMA CURING**

In the current investigation, mechanical characterisation of UV LED photo cured PMMA was carried out and optimum values of photo initiator concentration and cure time was obtained for achieving higher elastic modulus and hardness.

Results of experimentation carried out to optimise the parameters for curing PMMA are summarised in Table 5.2. Also, Figure 5.3 shows the effect of varying PI concentration on Young's modulus and hardness for the given curing time. Hence, from the nano-indentation test results shown in Figure 5.4, it was evident that initially hardness and Young's modulus increased with increase in cure time due to increase in degree of polymerisation. However, after reaching a threshold value, the hardness and Young's modulus decreased due to photolysis and degradation effect. Overcuring of PMMA results in decomposition of radical end and chain termination as described in literature (Fox et al., 1964).

In the current investigation, hardness and Young's modulus was considered for mechanical characterisation of UV cured PMMA alone. The sample No. 5 with 4% PI concentration and 45 minutes cure time was found to be the optimum value for photo polymerisation of MMA with hardness and Young's modulus values as 0.13 GPa and 4.2 GPa, respectively.

**Table 5.2** Mechanical Properties for Varied PI Concentration and Curing Depth

Sample No.	PI (%)	Curing time (min)	Hardness (GPa)	Young's modulus (GPa)
1	3	75	0.07	2.7
2	3	90	0.08	3.2
3	4	25	0.04	1.8
4	4	35	0.06	2.6
5	4	45	0.13	4.2
6	4	60	0.07	1.6
7	5	25	0.02	0.9
8	5	35	0.08	3.2
9	5	45	0.11	3.5
10	5	60	0.09	2.3

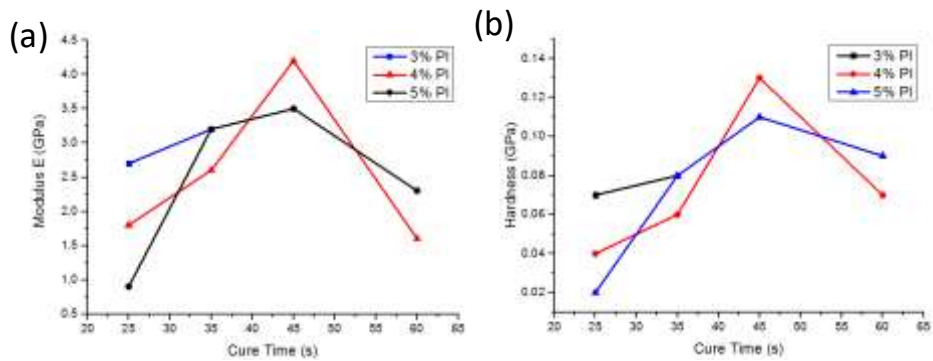


**Figure 5.3** (a) Influence of Cure Time on Elastic Modulus of PMMA (b) Influence of PI Concentration on Hardness of PMMA

From the experimental investigation, the significance of PI concentration in photo resin and curing time on the mechanical strength of cured PMMA was studied. Nano-indentation test was carried out by assigning an input of 2.5  $\mu\text{m}$  indenter displacement into the sample. The indentation plot for sample no. 5 (having maximum mechanical properties) is shown in Figure 5.4. It can be observed from the Figure 5.3 that hardness is lower within the surface. This was the result of lower degree of curing in comparison to surface having lower transmissibility of top layers after initial photo polymerisation.

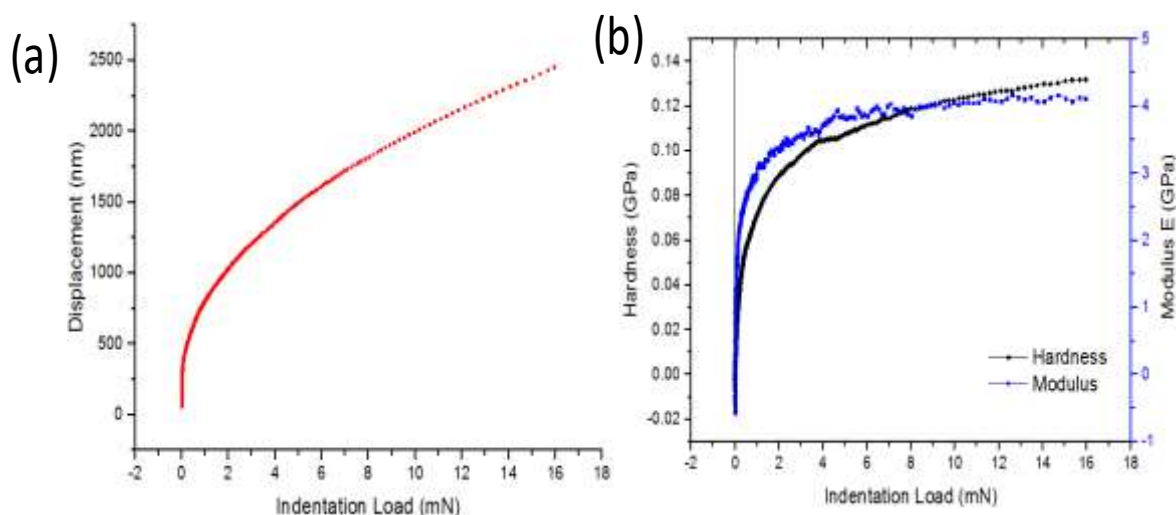


**Figure 5.4** (a) Nano-Indentation Plot for Sample 5 (b) Hardness & Modulus Variation With Indentation Load

### 5.3 RESULTS OF CO-POLYMERISATION

Initially, HDDA alone was experimented for photo polymerisation and characterised to get its FTIR spectrum. Table 5.3 shows the stretching frequencies of HDDA alone and Figure 5.5 shows the FTIR spectrum of the HDDA alone. Stretching frequencies match with the FTIR spectrum and confirms that the sample is HDDA. This result would be useful for characterising copolymerised HDDA and PMMA.

Co-polymerisation is attempted using HDDA and PMMA using micro stereolithography setup. Simple rectangular blocks were fabricated with HDDA and

PMMA precursor at feed rate 0.5, 1.0, 1.5 mm s<sup>-1</sup> on MSL. Later the samples were analysed using FTIR spectroscopy technique to find out the amount of presence of MMA and HDDA in the fabricated sample.

*HDDA standard*

**Table 5.3** Stretching Frequencies of HDDA

Sl. No.	Wave number (cm <sup>-1</sup> )	Groups
1	1,168	C-O Stretching
2	1,620	C=C Stretching
3	1,718	C=O Stretching
4	2,861 and 2,941	C-H aliphatic stretch

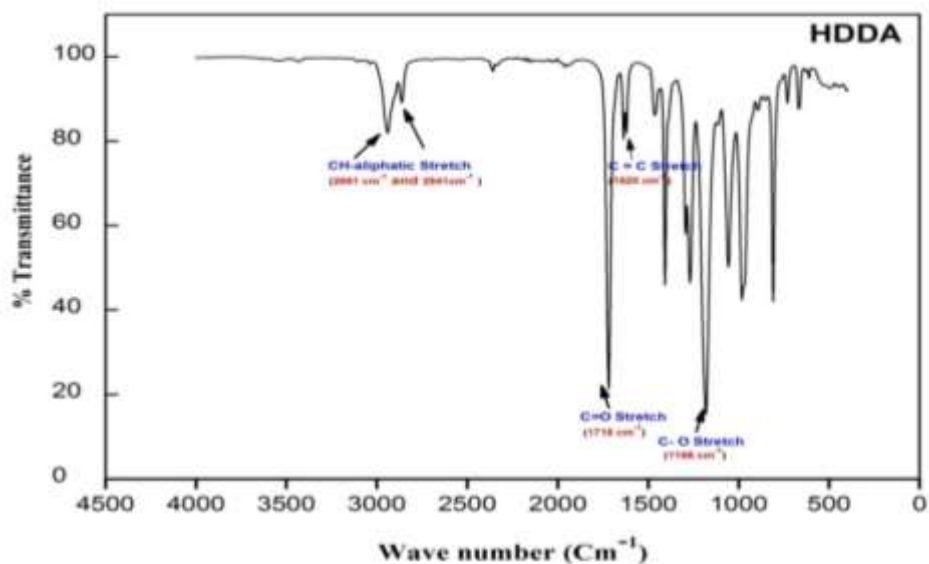


**Figure 5.5** FTIR Spectrum of HDDA

BEE standard

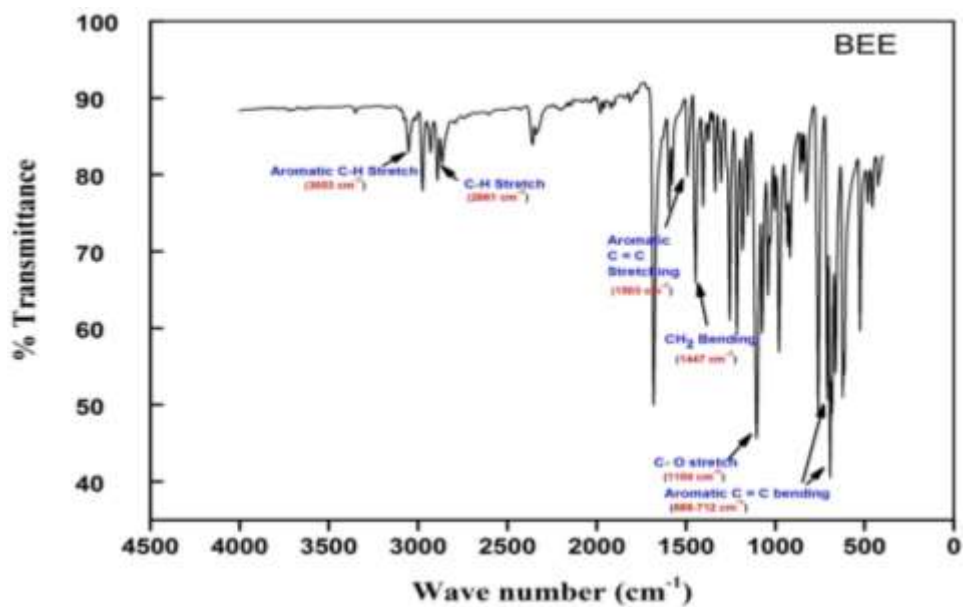


Figure 5.6 FTIR Spectrum of BEE

Table 5.4 Stretching Frequencies of BEE

Sl. No.	Wave number (cm <sup>-1</sup> )	Groups
1	688-712	Aromatic C=C bending
2	1,104	C-O Stretching
3	1,168	CH <sub>2</sub> Bending
4	1,449	Aromatic C=C stretching
5	1,679	C=O stretching
6	2,869	Aliphatic C-H stretching
7	3,069	Aromatic C-H stretching

MMA standard

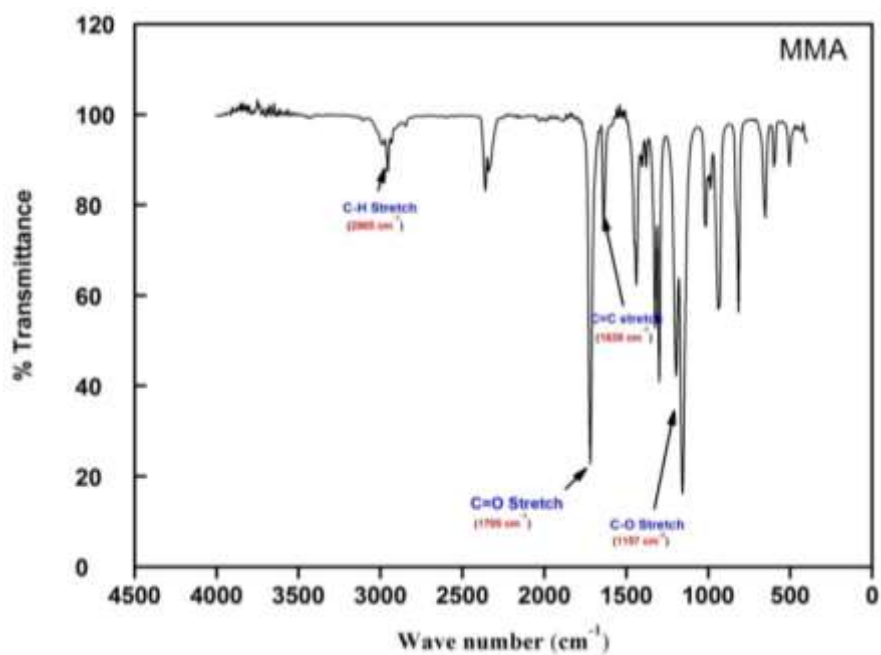
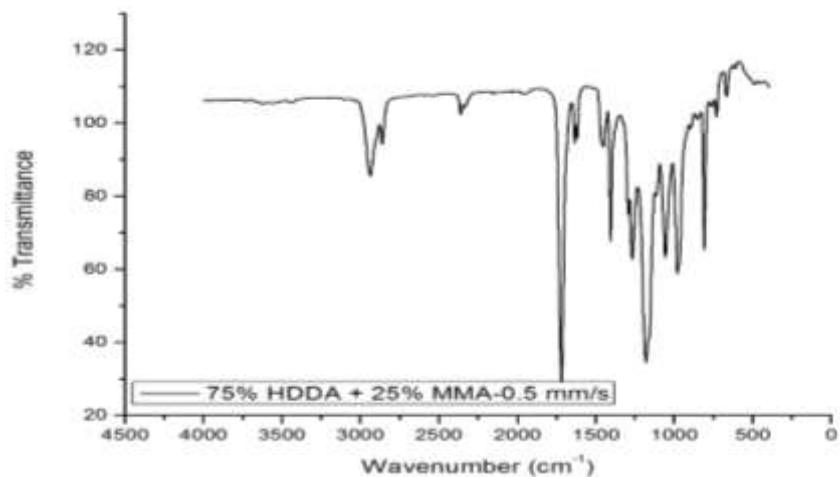


Figure 5.7 FTIR Spectrum of MMA

Table 5.5 Stretching Frequencies of MMA

Sl. No.	Wave number (cm <sup>-1</sup> )	Groups
1	1,157	C-O Stretching
2	1,639	C=C Stretching
3	1,700	C=O Stretching
4	2,965	C-H stretch

*FTIR spectra of fabricated (co-polymerised) samples*



**Figure 5.8** FTIR Results Sample Fabricated at 0.5 mm/s

The FTIR spectrum of the sample fabricated with above-said precursor (feed rate of 0.5 mm/s) in Figure 5.8 matches with the stretching frequencies of HDDA alone (both intensity and wave number). No stretching frequencies corresponding to BEE and PMMA were observed.

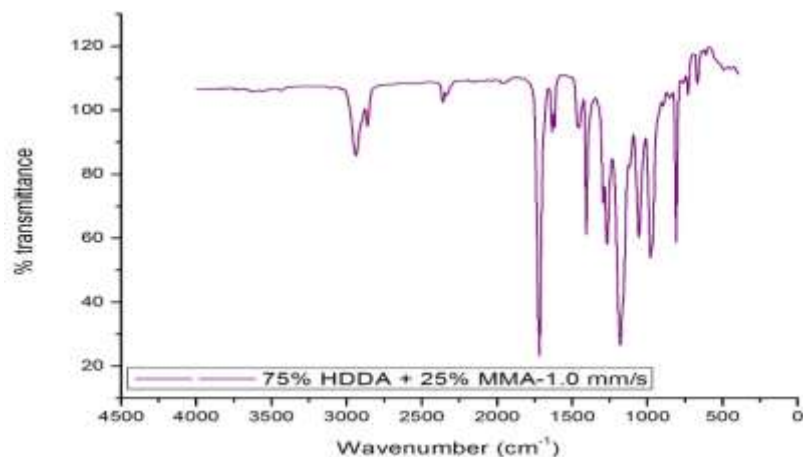


**Figure 5.9** FTIR Spectrum of Sample Fabricated at 1.0 mm/s

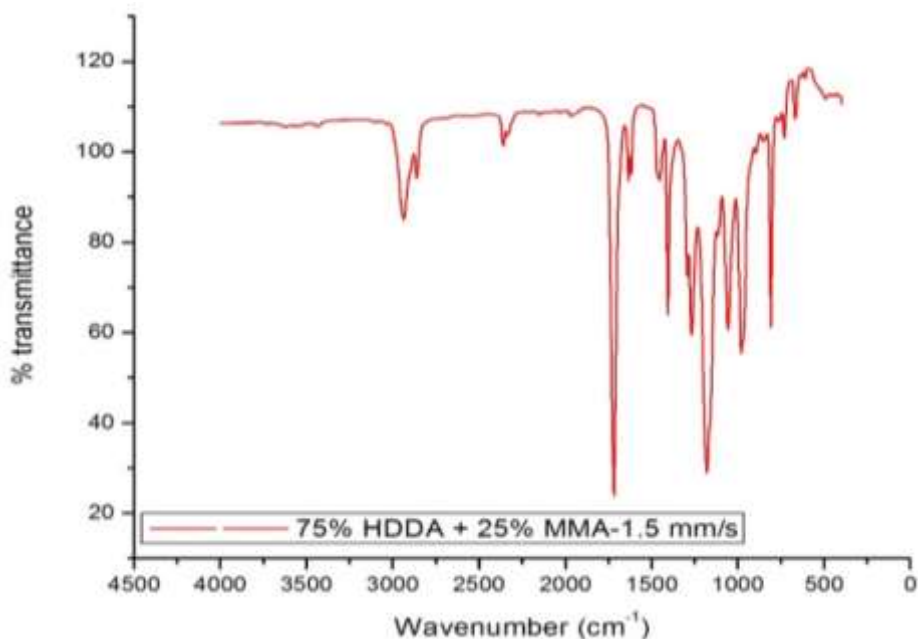


**Figure 5.10** FTIR Spectrum of Sample Fabricated at 1.5 mm/s

No stretching frequencies corresponding to BEE and PMMA were observed from samples fabricated with scan speed of 1.0 mm/s and 1.5 mm/s. Similar was the case with these two samples that were fabricated (Figure 5.9 and 5.10).

Even though vertical shift is observed, it might be due to various reasons such as difference in crystal cleaning, improper sample clamping on the diamond crystal, absorption of light by air molecules, etc. It was found that the required structure of PMMA has not formed.

#### **5.4 EXPERIMENTATION ON MICRONEEDLE MOLD FABRICATION**

In order to evaluate the fabricated microneedle structure and dimension, characterisation was done using SEM. Figure 5.11 shows the actual image and SEM image of PDMS microneedle array. From SEM characterisation, it was found that the height of needle and tip diameter measured between 210-220  $\mu\text{m}$  and 31-35  $\mu\text{m}$  respectively, whereas the micro-tools used in mould fabrication had tip diameter between 20-22  $\mu\text{m}$ . With this, it was observed that a close replication between the final fabricated structure and micro-tool dimensions exists. This minimal deviation of

final fabricated structure was the resultant of mould fabrication and final casting process.

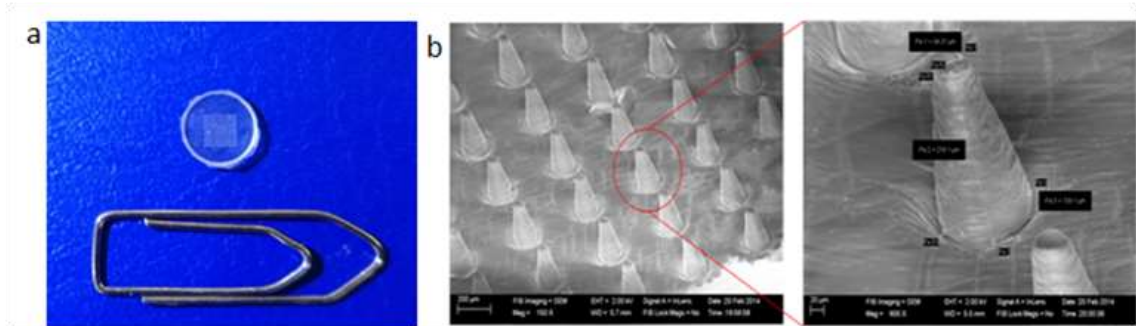


**Figure 5.11** (a) PDMS Microneedle Array, (b) SEM Image of PDMS Microneedle Array

A simple hybrid approach combining micromachining and micromolding processes for fabrication of solid polymeric microneedle was studied. The PDMS microneedle array so fabricated was used as master mould for fabrication and reproduction of microneedles by several methods. Experimentation conducted to fabricate PMMA micro needle from PDMS mould had not yielded desired results due to adhesion of PMMA material to PDMS.

## 5.5 RESULTS OF MICROMACHINING

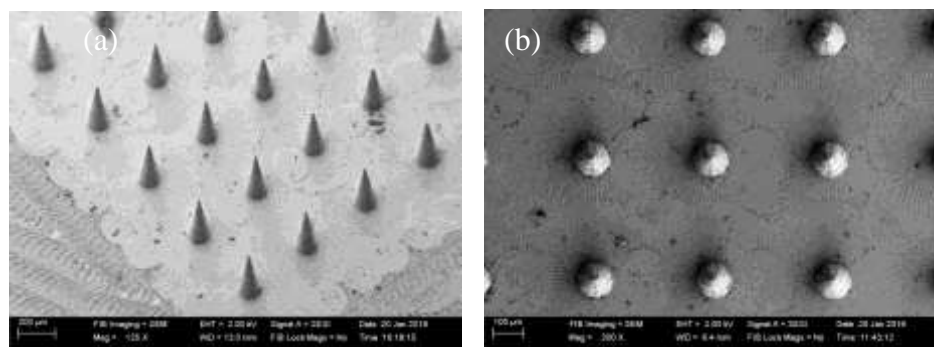


**Figure 5.12** (a) SEM Image of Microneedle Arrays (b) Top View of Needles

Confocal image of fabricated microneedle is shown in Figure 5.12 with tip diameter around  $7.5 \mu\text{m}$  and height  $225 \mu\text{m}$ . SEM image of single microneedle is shown in

Figure 5.13. The microneedle was found to be sharp and retaining its shape well. Against the programmed value of 200  $\mu\text{m}$ , the height values are around 200-230  $\mu\text{m}$ . Whereas the tip diameter was around 5-15  $\mu\text{m}$  against the programmed value of 5  $\mu\text{m}$ .

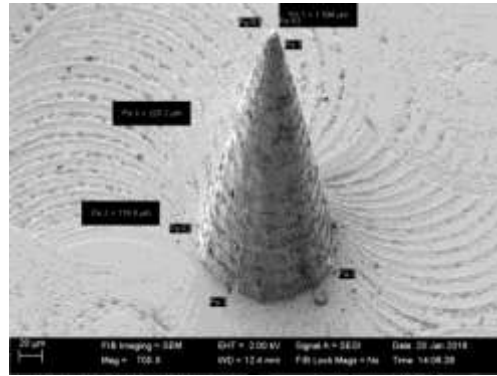


**Figure 5.13** SEM Image of Single Microneedle

Base diameter of 120  $\mu\text{m}$  more remained constant for all needles throughout the development process. When measured using SEM, whose details are provided in Appendix III, it was observed that all the microneedles are of uniform size (<5% variation).

## 5.6 ELECTROLESS SILVER PLATING

### *Stereo Microscopic Studies*

The stereomicroscopic images before coating clearly indicate that the surface was roughened which is as shown in figure 5.14. Figure 5.15 represents surfaces coated with silver.

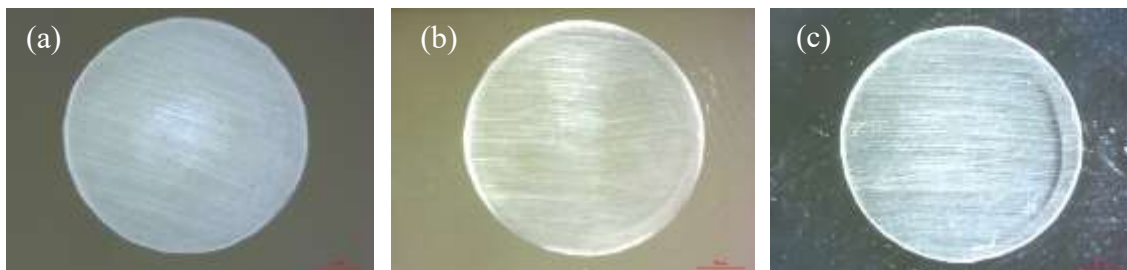


**Figure 5.14** Images of Roughened Surface With Different Grit Papers (220, 500, and 1000) before coating



**Figure 5.15** Images of Roughened Surface With Different Grit papers (220, 500, and 1000) after coating

*X-ray diffraction (XRD) study*

The X ray diffraction studies of the different silver coated PMMA discs are represented in Figure 5.16. The XRD analysis clearly indicated the formation of silver over PMMA. The sharp peaks at  $2\theta$  values of 38.11, 44.38, 64.54, 77.54 and 81.56 which agree well with literature values of silver. These peaks can be indexed to (111), (200), (311) and (222) planes respectively and indicates a face centered cubic lattice. One can also notice that apart from the silver peaks, other peaks were absent indicates that, the so formed coating is free from impurities.

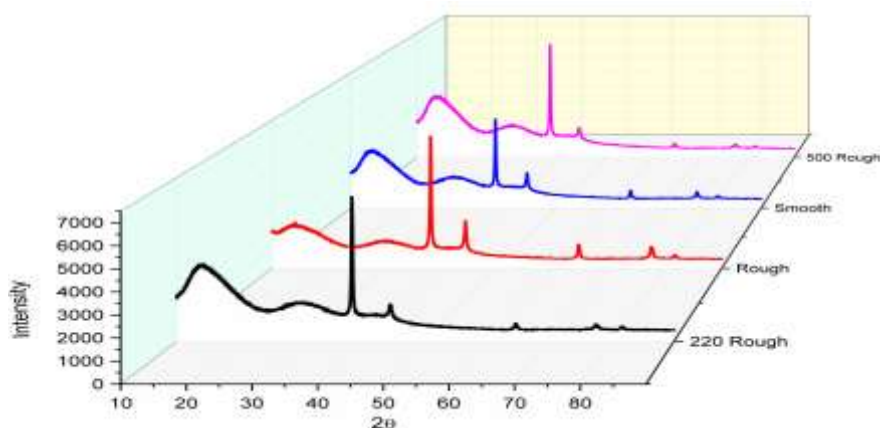


**Figure 5.16** Stacked XRD Spectrum of silver coated polymer

*Roughness measurement*

The surface roughness studies before and after coating reveals that, the surface roughness plays a major role in deposition of silver. As the surface roughness increases which increase sites for silver deposition. As a result one can observe that

there is a huge variation in the surface roughness values before and after coating for sample a1. But in the case of sample b1 and sample c1 the surface roughness is relatively less, therefore one can found that there is a marginal difference in the surface roughness values. Thus surface roughness studies were clearly states that the surface roughness decreases which may be due to the coating of silver over the roughened track. The surface roughness studies were given in figure 5.17.

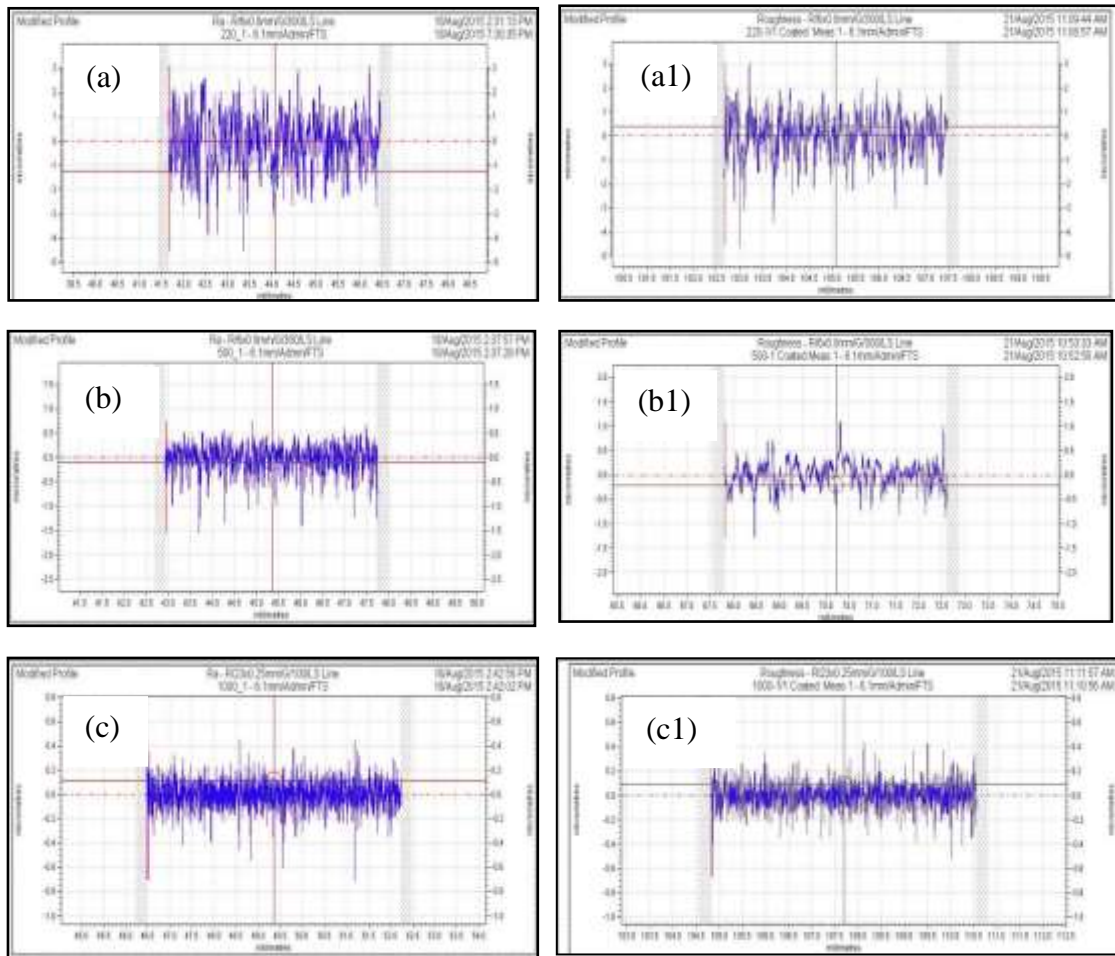


**Figure 5.17.** (a), (b), (c) Surface Roughness Before Coating Using Different Grit Papers (220, 500, and 1000) and (a1), (b1), (c1) Surface Roughness After Coating

The measured surface roughness values are given in the table 5.6

**Table 5.6** Surface Roughness Values Before and After Coating

Sl. No.	Sample	Ra before coating ( $\mu\text{m}$ )	Ra after coating ( $\mu\text{m}$ )
1.	Modified with 220 grit paper	0.83	0.70
2.	Modified with 500 grit paper	0.19	0.20
3.	Modified with 1000 grit paper	0.07	0.07

*Field Emission Scanning Electron Microscopic (FESEM) studies*

The FESEM of images (Figure a1, b1 & c1) clearly show that the coating happened over the surface, one can also observe the tracks along with the coating, and these tracks are because of the roughness created over the polymer surface before coating by grit paper.

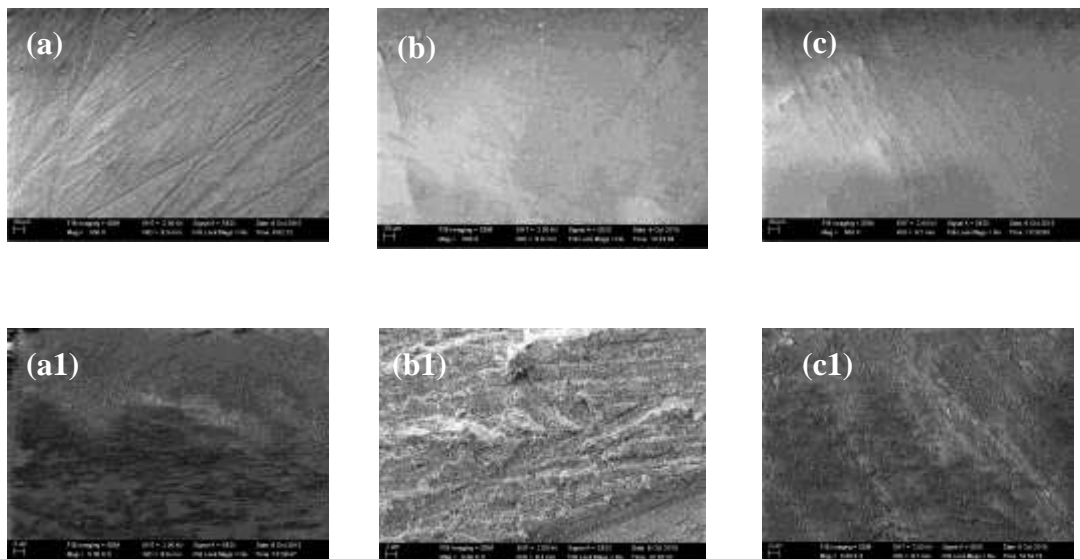


**Figure 5.18** FESEM Images of Coated Samples

Figure 5.18 represents the surface morphology studies using FESEM. Figures 5.18 a, b and c represent the roughened surface with different grit papers (220,500 and 100) and Figures 5.18 a1, b1 and c1 represent the roughened surface with different grit papers (220,500 and 100) after coating. Surface charging effect was not observed in FESEM images which clearly represents that the Surface is coated with metallic silver. The sample which is having higher roughness shows higher amount of coating this may due to the fact that the higher surface roughness samples gives more area of tracks which will help the particles to accumulate in these tracks. As the roughness decreases, this will decrease the amount of coating also.

#### *Peel-Off Studies*

It is evident from the figure 5.19 (a1) that only minimal amount of silver was peeled off from the high rough substrate. The increase in adhesion can be attributed to the greater mechanical interlocking due to the increase in surface roughness of the substrate. Figure 5.19 shows the results of the adhesion test.

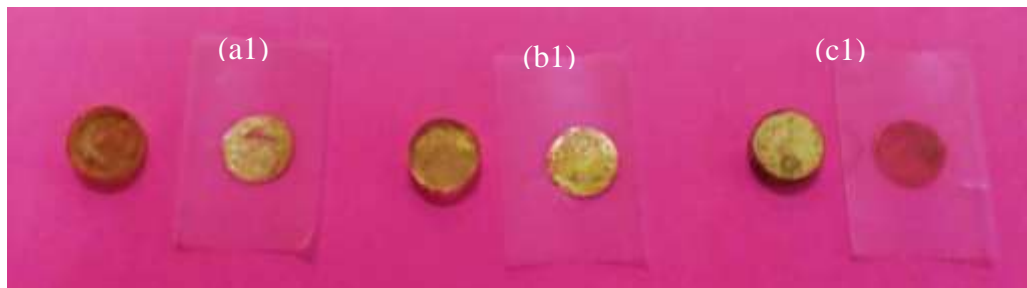


**Figure 5.19** Peel Off Test After Electroless Deposition of Silver Over Smooth And Rough PMMA Surface

#### *Resistivity Measurement*

The resistivity study of the sample c1 was carried out using four probe tester. The resistivity of the sample was measured at different areas with two different source current. The results obtained are tabulated in table 5.7.

**Table 5.7** Resistivity of the Sample

Sample ID	Source Current	VAB mv		VAD mv		Resistivity mΩ-cm
c 1	1 mA	1.42	1.44	6.13	6.04	1.534
	2 mA	2.89	2.85	12.23	12.32	1.546

The resistivity at different areas of the sample was found to be 1.534 and 1.546 mΩ-cm, which indicates uniform coating over the surface. It was also observed that the coating of silver and adhesion was found to be better, as the roughness increased, the electrical conductivity is expected to be higher than the sample c1. But the roughness of the other two samples was found to be very high and the four probe tester was unable to detect the current flowing through the coating on the sample. This may be due to the formation of peaks and valleys by surface modification resulting in discontinuous deposition of silver.

The resistance of microneedle array due to electroless deposition with silver and sputter coating with gold was tested using a multi-meter.



**Figure 5.20** Resistance Measurement

The resistance values varied from 6.5 Ω to 11.8 Ω when tested at the top of the surface as shown in Figure 5.20. Resistance of less than 10 Ω had been reported (Hedge et al., 2013) with the micro needles. As the resistance values obtained are comparable and microneedles coated with silver and gold are expected provide satisfactory biopotential signals.

## 5.7 Skin-Electrode Impedance Measurement

Micro needle patch was mounted using silver oxide on to commercially available stubs. Both wet electrodes and dry electrodes are fixed on forehead using self-adhesive tape. Skin electrode impedance for dry electrode and wet electrode are measured using the measurement set up available at DEBEL, Bangalore. Experiments were carried out with scholar as subject (Fig. 5.21)



**Figure 5.21** Impedance Measurement

**Table 5.8** Skin Electrode Impedance Values (with wet electrode as reference and ground)

Position	Skin Electrode Impedance	Position	Skin Electrode Impedance
FP1 Dry Electrode	40 k $\Omega$	F4 Wet Electrode	46 k $\Omega$
FP2 Dry Electrode	47 k $\Omega$	F3 Wet Electrode	31 k $\Omega$
		C3 Wet Electrode	48 k $\Omega$

**Table 5.9** Skin Electrode Impedance Values (with dry electrode as reference and ground)

Position	Skin Electrode Impedance	Position	Skin Electrode Impedance
FP1 Dry Electrode	26 k $\Omega$	C3 Dry Electrode	37 k $\Omega$
FP2 Dry Electrode	17 k $\Omega$		

Table 5.8 & Table 5.9 shows the impedance values for dry electrode and wet electrodes. It can be observed that the impedance values for micro needle based dry electrode are comparable to wet electrode. Micro needles overcome electrical and mechanical SC barrier and provide improved conductivity and reduction in contact impedance.

## 5.8 EEG Signal Acquisition

To find out the correlation between microneedle based dry electrode and conventional wet electrode, EEG signals were acquired using the 4 channel signal acquisition set up (Fig. 5.22) available in house.



**Figure 5.22** EEG Signal Acquisition Setup

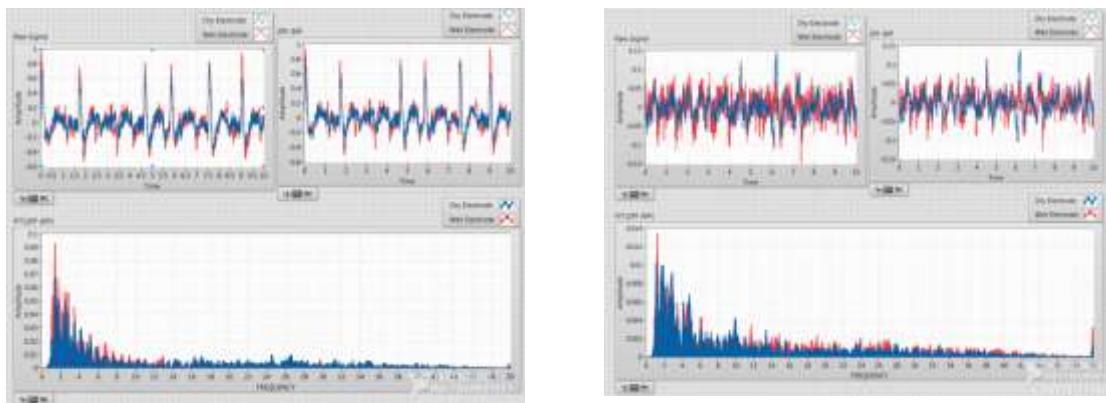


**Figure 5.23** Signal Acquired at (a) Subject in Active State (Eyes Open) (b) Subject in Inactive State (Eyes Closed)

EEG signal acquired (Fig. 5.23) using dry and wet electrode were analysed for correlation and it was found that the correlation obtained was about 94%. Signals from dry electrodes are almost analogous to wet electrodes. This testifies the good

performance of micro needle based dry electrode for EEG signal acquisition under static conditions.

## 5.9 COMPRESSION TEST RESULTS

Compression test was mainly performed to assess the PMMA microneedle for its strength when it was subjected to loading by non-deformable object. Compressive load was done on 10x10 PMMA microneedle array which was micro machined. The needles were getting compressed gradually as the load was being applied. From Figure 5.25, it is observed that up to duration of 90 seconds, there was no contact between the needle tip and the loading stub. After 90 seconds, loading of needle started due to contact and reaction forces started acting.

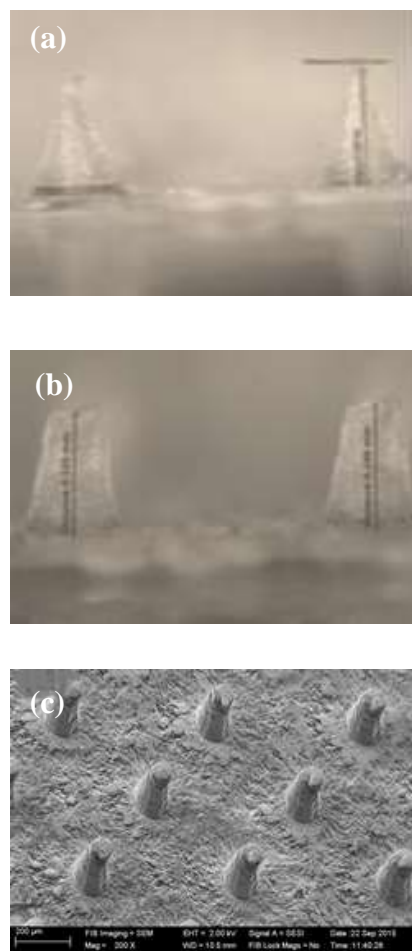


**Figure 5.24** Compression Test on microneedle array (a) Needles before the Test (b) & (c) Needles after the Application of Compressive Load

Reaction forces were continuously measured using mini-dynamometer. Figure 5.24 shows the needle before and after compression. From the graph 5.25, load vs deformation, it is observed that the reaction force was less initially. This was due to the reason that the needle was weak at the tip. Later the reaction force was increasing linearly with respect to compression in axial direction.

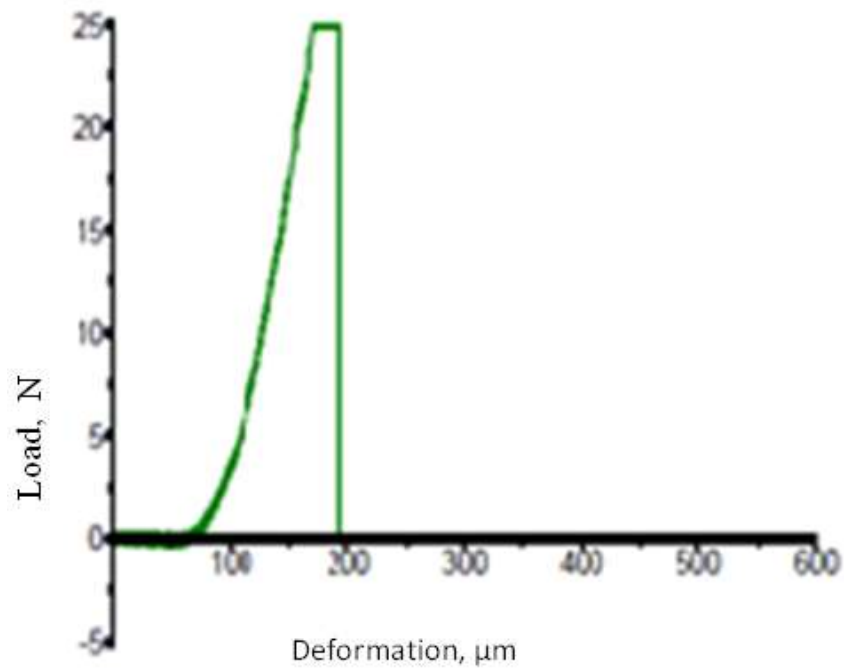


**Figure 5.25** Compressive Load vs. Deformation

The test was carried out until the deformation was observed to be 150  $\mu\text{m}$ . It can also be found from the figure that the needles have deformed from 240  $\mu\text{m}$  to 145  $\mu\text{m}$ . Microneedle could withstand a load of 4 N for a deformation of 25  $\mu\text{m}$ , which is around 10% strain.

## 5.10 SHEAR TEST RESULTS

Microneedles are usually subjected to axial load. It may also be subjected to transverse load during some situations. It is necessary to know the load at which the needles fail. Figure 5.26 (a) shows the needle before shear test and the 5.26 (b) shows the needle after shear. It is observed that needle has not fractured due to shear but only has got yielded. This is one of the main advantages of going for polymer as there will not be any trace of material in skin if the needle fails.

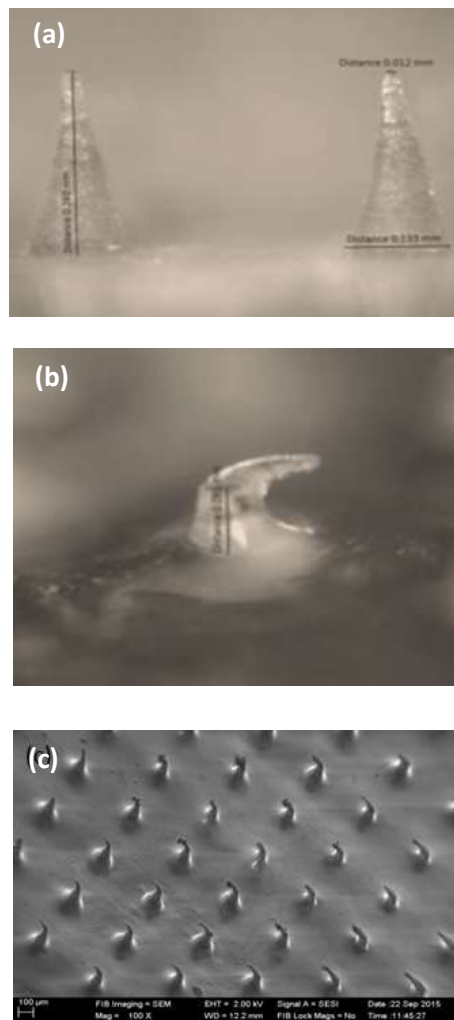


**Figure 5.26** Shear Test Images (a) Needle Before Shear (b) & (c) Needle After the Application of Shear Load

Yusuf et al. (2013) had conducted testing of poly (lactic-co-glycolic acid) (PLGA) and sodium alginate (SA) microneedles and found that SA needles failed at 0.05 N load when the load was acting on single microneedle.

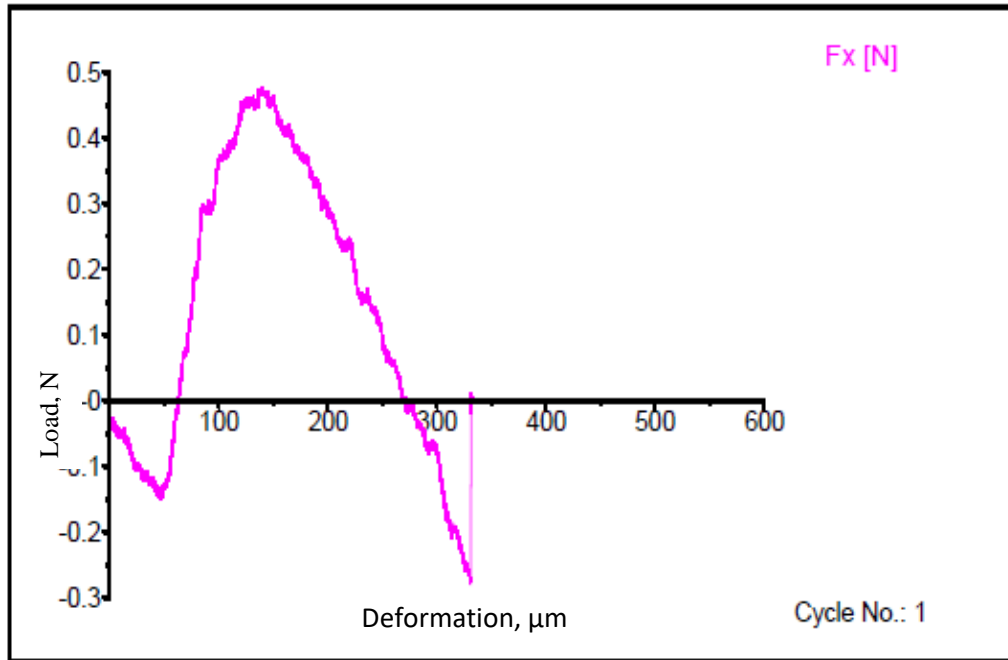


**Figure 5.27** Results from Shear Test (a) Shear Load vs. Deformation of the Needle Array

From the results of shear test it was observed that first row of 10 needles withstood loads greater than 0.5 N before completely shearing and for complete array of needles it will be understandably much higher. Microneedle array is considerably weaker in shear, which is attributed to aspect ratio of the structure and fabrication material (PMMA). However, during insertion care must be taken to ensure that the microneedles are mostly subjected to compressive loads by controlled insertion.

## 5.11 INSERTION TEST RESULTS

PMMA microneedles were inserted into Chicken Skin mimicking the mechanical property of skin. Mini-dynamometer was used to measure the load applied.

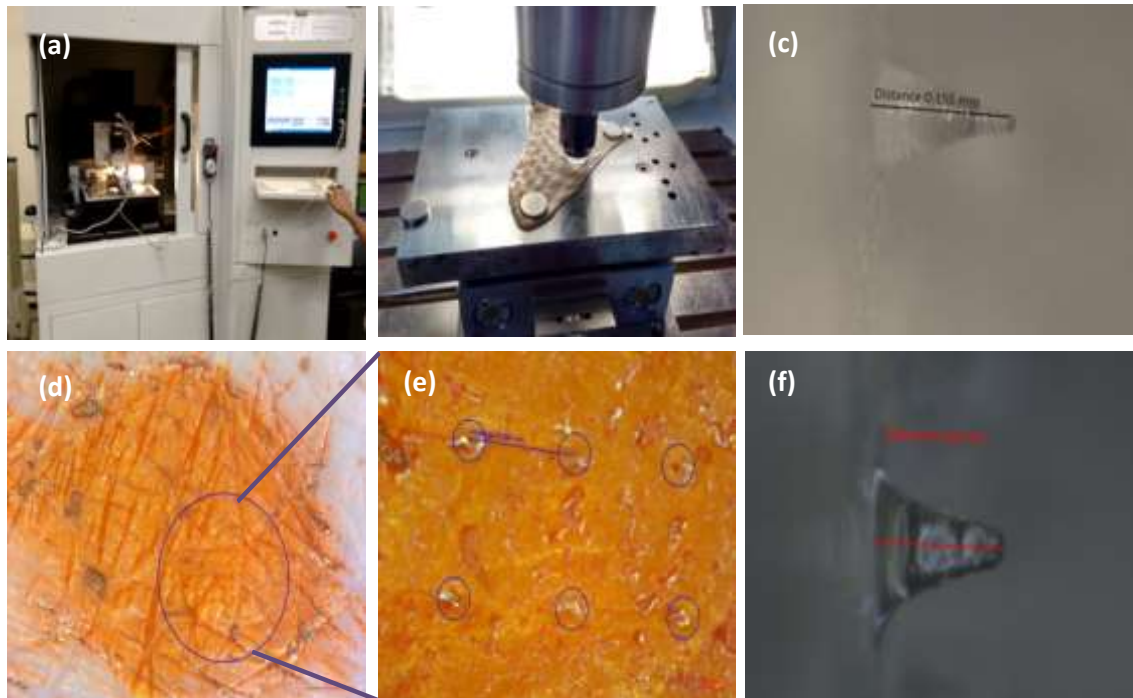


**Figure 5.28** Insertion Test (a) Test Rig (b) Chicken Skin Under Insertion (c) & Needle Before Insertion (f) Needle After Insertion (d) & (e) Chicken Skin After Insertion

Figure 5.28 (a) shows the test rig for PMMA microneedle insertion into chicken skin. The feed for penetration was controlled by the Z Axis of the micro machine tool (DT-110, Mikro Tools, Sg). Needles were subjected to a load of 7.5 N for a penetration of 150  $\mu\text{m}$ . Figure 5.28 (c) shows needle before insertion of needle into chicken skin and Figure 5.28 (f) shows needle before insertion of needle into chicken skin. Image under figure 5.28 (e) confirms the needles penetration into the chicken skin.

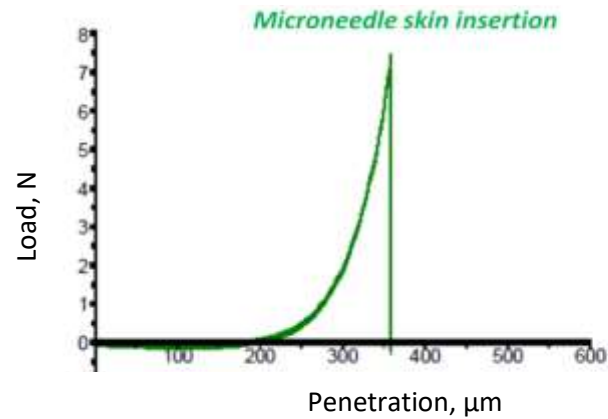


**Figure 5.29** Load vs. Penetration Plot (Skin Insertion)

By comparing microneedle height, it was observed that the microneedle deformation was 10  $\mu\text{m}$  and maximum load that microneedle array could withstand was 7.5 N (Figure 5.26). Also, buckling of needle was not observed. Though the needles can withstand beyond 150  $\mu\text{m}$ , the experiment was stopped at this point as this meets minimum requirement of 120  $\mu\text{m}$  penetration. It was observed that 3 N force only required for insertion to a depth of 120  $\mu\text{m}$ .



## CHAPTER 6

### CONCLUSIONS AND SCOPE FOR FUTURE WORK

#### 6.1 CONCLUSIONS

- PMMA is compatible with human tissue. It is commonly used to manufacture intraocular lenses that are implanted in eyes. To reduce wrinkles and scars, PMMA microspheres are suspended in biological fluid and injected under the skin for reducing wrinkles and scars. PMMA is durable and safe. Hence, PMMA was selected as a material for fabrication of microneedle.
- Force required to pierce the skin is about 0.06 mN for the tip diameter of 5  $\mu\text{m}$  and 2.0 mN for tip diameter 30  $\mu\text{m}$ , whereas failure force of needle due to compression was 1 mN and 36 mN for tip diameter of 5  $\mu\text{m}$  and base diameters of 50  $\mu\text{m}$  and 120  $\mu\text{m}$ , respectively. Theoretical calculations show the force required to pierce the skin is much less than the force required for microneedle failure.
- As per theoretical calculation, deformation of the needle was about 6.6  $\mu\text{m}$  for the needle tip diameter of 5  $\mu\text{m}$ , base diameter of 120  $\mu\text{m}$  and length of 200  $\mu\text{m}$ . The deformation of the needle was less than 5%.
- FEM simulation of microneedles insertion into skin for various loads (5 N-10 N) base diameters (50  $\mu\text{m}$ -120  $\mu\text{m}$ ) and pitches (0.3 mm-0.7 mm) shows the behavioural properties of PMMA microneedle. As expected, increase in base diameter of needles strengthen the needles. Increase in base diameter of needle at the same time reduced the penetration and strain up to a certain point. Beyond this beyond, penetration increases, strain continues to reduce. For a base diameter of 120  $\mu\text{m}$  and pitch of 0.4 mm, penetration is more and the strain is less. Based on this, optimum values pitch of 0.4 mm and base diameter of 120  $\mu\text{m}$  was arrived for microneedle geometry.
- The research activity came out with a novel method of microneedle fabrication using MSL process with HDDA material. It turned out to be a step-less unique

fabrication process. Challenge of making PMMA microneedle using this process still persists due to low reactivity of PMMA material.

- FTIR spectrum of HDDA and PMMA co-polymerisation experiment shows the stretching frequencies HDDA only. Absence of PMMA stretching frequency shows the poor co-polymerisation.
- Negative micro mold was successfully fabricated using PDMS mould through micromachining and micro molding route with the aid of UV LED curing. Adhesiveness problem associated with PMMA sticking to the Teflon and PDMS mould still needs to be addressed.
- Direct micromachining of PMMA using micromachining centre yielded needles of required structure. Strategies like layer-by-layer machining, varying depth of cut and cutting conditions enabled realising the microneedle to the required size. SEM image of single microneedle shows the geometrical integrity of fabricated microneedle. Microneedles were found to be sharp and retaining their shape well. Against the programmed value of 200  $\mu\text{m}$ , the height values are around 200-230  $\mu\text{m}$ . Whereas the tip diameter was around 5-15  $\mu\text{m}$  against the programmed value of 5  $\mu\text{m}$ . Base diameter of 120  $\mu\text{m}$  more or less remained constant for all needles throughout the development process. When measured using SEM, it was observed that all the microneedles are uniform (<5% variation).
- Initial compression testing of microneedle showed that the micro milled needles penetrated the skin with less deformation. Microneedle withstood a load of 4 N for a deformation of 25  $\mu\text{m}$ , which is less than 10% strain. [0.1 N-3 N is sufficient for piercing skin (Shawn P. Davis et al., 2003)].
- From the results of shear test it was observed that first row of 10 needles withstood loads greater than 0.5 N before completely shearing and for complete array of needles it will be understandably much higher. Microneedle array is considerably weaker in shear, which is attributed to aspect ratio of the structure and fabrication material (PMMA). Care must be taken to ensure microneedles are mostly subjected to compressive load by controlled insertion.

- Insertion of microneedles on chicken skin shows that the microneedle deformation was as less as 10  $\mu\text{m}$  and maximum load that microneedle array could withstand was as high as 7.5 N.
- Electroless coating has been tried for coating silver on PMMA. Surface roughness of the substrate is an important factor in adhesiveness of the silver onto PMMA. XRD results of PMMA coated with silver showed the formation of silver.
- The resistance of microneedle array due to electroless deposit with silver and sputter coating with gold was tested using a multi-meter. The resistance values varied from 6.5  $\Omega$  to 11.8  $\Omega$  when tested at the top of the surface. Results show that the needles offer less electrical resistance and could be used for biopotential measurement after a protective coating on needles to avoid oxidation of silver
- Correlation of EEG signals acquired from dry and wet electrodes was about 94%. Signals from dry electrodes are almost analogous to wet electrodes. This testifies the good performance of micro needle based dry electrode for EEG signal acquisition under static conditions.

Results show that the designed microneedle patch could be fabricated using micro machining. With the conductive coating on it, the microneedle patch could be used for biopotential measurement with less pain and without much deformation to microneedle.

## 6.2 SCOPE FOR FUTURE WORK

Although microneedles were fabricated by micromachining and characterisation of microneedles were carried out, following future work may be undertaken for further improvisation.

- Performance of microneedles when used for longer duration.
- Performance of microneedles under dynamic conditions.
- Polymerisation of PMMA with higher power laser/light source using MSL.
- Nano-imprint lithography and micro-injection moulding as an option for volume production of microneedle arrays.
- Biocompatible, UV curable and conductive polymer as a potential material for microneedles.
- Biocompatibility tests: Microneedles made of PMMA are directly in contact with human tissue. Hence, biocompatibility test is essential. There are three tests essentially required to show that the material is biocompatible. The tests needed are cytotoxicity as per ISO 10993-5, Skin Sensitization Study as per ISO 10993-10 and acute irritation/intracutaneous reactivity as per ISO 10993-10.

## REFERENCES

- Aisling Ni Annaidha, et al. (2012) Characterization of the anisotropic mechanical properties of excised human skin. *J Mech Behav Biomed Mater.* 27:139–148.
- M. W. Ashraf *et al.*, (2010). Design, analysis and fabrication of MEMS-based silicon microneedles for bio-medical applications," Int. Conf. On *Electrical Engineering/Electronics Computer Telecommunications and Information Technology (ECTI-CON)*, pp. 950-953.
- Ali Bulent Usakli, (2010). Improvement of EEG Signal Acquisition: An Electrical Aspect for State of the Art of Front End. Hindawi Publishing Corporation, *Computational Intelligence and Neuroscience*. Vol. 2010, Article ID 630649, 7 pages doi:10.1155/2010/630649.
- Ankur Goswami, Arindam Phani, Ankit Krishna, Balashanmugam, N., Giridhar Madras, and A.M.Umarji, (2011) Poly-HDDA microstructure fabrication using Micro stereo lithography for Micro-cantilever based sensor technology. *Proceedings of SPIE* Vol. 7926, doi:10.1117/12.888045.
- Anfeng Wang, Paul, G., Finlayson, Jie Li, Kelley Brabant, Carolyn, A. Black., James McAllister, P., Ting Cao, Haiying Tang, Xuemei Liang, Steven O. Salley, Gregory W. Auner, and K. Y. Simon Ng. (2005). Is Silicon Suitable for Making Implantable Biomedical Devices? <https://aiche.confex.com/aiche/2005/techprogram/P15420.HTM>.
- Boehm, R D and Miller, P R and Hayes, S L and Monteiro-Riviere, N A and Narayan, R. J. (2011). Modification of microneedles using inkjet printing, *AIP Advances*, 1, 022139. DOI:<http://dx.doi.org/10.1063/1.3602461>.
- Boyer G, Molimard J, Ben Tkaya M, Zahouani H, Pericoi M, and Avril S. (2013) Assessment of the in-plane biomechanical properties of human skin using a finite element model updating approach combined with an optical full-field measurement on a new tensile device. *J Mech Behav Biomed Mater.* 2013;27:273–282.

- Charlotte Tsui. (2007). Instron Tensile Testing: Structural and Material Properties of Chicken Skin Regions. <https://www.google.co.in/#q=properties+of+chicken++chicken+charlotte+tsui>
- Chen, B. Jiashen Wei, Francis E.H. Tay, Yee Ting Wong, Ciprian Ilescu. (2007). Silicon microneedles array with biodegradable tips for transdermal drug delivery. *DTIP of MEMS & MOEMS (2007)*. ISBN: 978-2-35500-000-3.
- Chen Pin-Chuan, Chang-Wei Pan and Kuan-Ming Li. (2014) 'An experimental study of micro milling parameters to manufacture micro channels on a PMMA substrate. *Int J Adv Manufacturing Technology*. 2014; 71:1623–1630.
- Choi, S.-O., Kim, Y.-C., Lee, J. W., Park, J.-H., Prausnitz, M. R. and Allen, M. G. (2012), Intracellular Protein Delivery and Gene Transfection by Electroporation Using a Microneedle Electrode Array. *Small*, 8: 1081–1091. doi:10.1002/sml.201101747.
- Chu LY, Choi SO, Prausnitz MR.(2010). Fabrication of dissolving polymer microneedles for controlled drug encapsulation and delivery: Bubble and pedestal microneedle designs. *J Pharm Sci*. Oct;99(10):4228-38. doi: 10.1002/jps.22140.
- Conor O'Mahony, Francesco Pinia and Kevin G. M. (2013). Microneedle-based electrodes with integrated through-silicon via for bio potential recording. *Sensors and Actuators*, 130-136; <http://dx.doi.org/10.1016/j.sna.2012.04.037>.
- Dufaud, O., Corbel, S. (2003). Oxygen diffusion in ceramic suspensions for stereolithography. *Chem Eng J*. 92:55–62.
- Donnelly, R. F., Garland, M.J., Morrow, D.I., Migalska K, Singh, T.R., Majithiya, R., Woolfson, A.D. (2010). Optical coherence tomography is a valuable tool in the study of the effects of microneedle geometry on skin penetration characteristics and in-skin dissolution. *J Control Release*. 147(3):333–341.
- Donnelly R. F., Raj Singh, T. R., Woolfson AD. (2010). Microneedle-based drug delivery systems: Micro fabrication, drug delivery, and safety. *Drug Deliv*. 17(4):187–207. doi:10.3109/10717541003667798.

Donald Garlotta. (2011). A Literature Review of Poly (Lactic Acid). *J Polym Environ.* Volume 9, Issue 2, pp 63-84.

Elena Forvi, Marzia Bedoni, Roberta Carabalona, Monica Soncini, Paolo Mazzoleni, Francesco Rizzo, Conor O'Mahony, Carlo Morasso, Domenico Giorgio Cassarà, Furio Gramatica. (2012). Preliminary technological assessment of microneedles-based dry electrodes, for biopotential monitoring in clinical examinations. *Sensors and Actuators A* 180 177– 186.

Elias, C. N., J.H.C. Lima, R. Valiev, and M.A. Meyers. (2008). Biomedical Applications of Titanium and its Alloys, *JOM*, Volume 60, Issue 3, pp 46-49.

Ferdinand Walther and Marc Hennemeyer, Sandra Kerstan, Polina Davidovskaya, Katrin Schürzinger, Alexander M. Gigler, Steffen Maßberg and Robert W. Stark. (2007). Enhancement of cell growth on SU-8 by O<sub>2</sub> Plasma activation. *Eur Cell Mater.* 14(3):101.

Fiedler, P., S. Brodkorb, C. Fonseca, F. Vaz, F. Zanow and J. Haueisen. (2010). Novel TiN-based dry EEG electrodes: Influence of electrode shape and number on contact impedance and signal quality. *IFMBE Proceedings.* Vol. 29 pp418-421.

Feifei Jiao and Kai Cheng. (2014). An experimental investigation on micro-milling of polymethylmethacrylate components with nanometric surface roughness. *J Eng Manufact.* 228:790–796.

Fox RB, et al. (1964). Photo degradation of poly(methyl methacrylate). *J Polym Sci.* 1964; A2(5):2085–2092.

Gargiulo G., Calvo, R.A.Bifulco, P.Cesarelli., M.; Jin, C.; Mohamed, A.; Van Schaik, A. (2010). A new EEG recording system for passive dry electrodes. *Clin Neurophysiol.*;121:686–693.

Hegde et al., Microneedle electrode. 2013 Patent No.: US 8,588,884 B2.

Griffiths, M., J. P. Grainger, M.V. Cox, A.W. Preece. (2005). Recent Advances in EEG Monitoring for General Anaesthesia, Altered States of Consciousness and Sports Performance Science. *3rd IEE International Seminar on Medical Applications of Signal Processing.* ISBN 0-86341-570-9/9-78086341-415708.

Heather Brannon. (2014). Skin Anatomy, <http://dermatology.about.com/cs/skin/anatomy/a/anatomy.htm>.

Henry S. (1998). Micro fabricated micro needles: A novel approach to transdermal drug delivery. *J Pharm Sci.* 87(8):922–925.

Henry S., McAllister DV, Allen MG, Prausnitz MR. (1998). Micro fabricated micro needles: a novel approach to transdermal drug delivery. *J Pharm Sci.* 87(8):922–925.

Ikawa N, et al. (1991). Atomistic analysis of nanometric chip removal as affected by tool-work interaction in diamond turning. *CIRP Annals.* 40:551–554.

Ikawa N, et al. (1991). Ultra precision metal cutting, the past, and the future. *CIRP Annals.* 40:587–594.

James Birchall. (2006). Microneedle array technology: The time is right but is the science ready? *Expert Rev Med Devices.* 3(1):1–4.

Kim CJ, M Bono and J Ni. (2002). Experimental analysis of chip formation in micro-milling. *Transactions of NAMRE/SME.* 30:1–8.

Jacobs, P. F. (1992). Fundamentals of Stereolithography.

Jee T, et al. (2014). In vitro measurement of the mechanical properties of skin by nano/micro indentation methods. *J Biomech.* 47:1186–1192.

Jones, R.G.,W. Ando, Julian Chojnowski. ( 2001 ). Silicon-Containing Polymers: The science and technology of their synthesis and applications. ISBN: 140200348X, 9781402003486.

Jordan David Hamilton. (2010). Fabrication and Analysis of Injection Molded Plastic Microneedle Arrays. *MS Thesis.* Georgia Institute of Technology.

Kabseog Kim, Daniel S Park, Hong M Lu, Wooseong Che, Kyunghwan Kim, Jeong-Bong Lee and Chong H Ahn. (2004). A tapered hollow metallic microneedle array using backside exposure of SU-8. *J Micromech Micro eng.* 14:597–603.

Koura N. (1990). Electro less Plating of Silver. William Andrew Publishing/Noyes from Knovel.com.

Leonard Y, Chu., Seong-O Choi, Mark R. Prausnit. (2010). Fabrication of Dissolving Polymer Microneedles For Controlled Drug Encapsulation And Delivery: Bubble And Pedestal Microneedle Designs. *J Pharm Sci.* 99(10):4228-38.

Lifeng Kang, Sui Yung Chan, Jaspreet Singh, Kochhar, Wei Jiang GOH. (2013). A novel method to fabricate polymeric micro needles. Patent: WO 2013137831 A1.

Lin C-T, Liao, L.D., Liu, Y.-H. Wang, I.-J., Lin, B.-S.; Chang, J.-Y. (2011). Novel Dry Polymer Foam Electrodes for Long-Term EEG Measurement. *IEEE Trans Biomed Eng.* 58:1200–1207.

Li-Sheng Hsu, Shu-Wei Tung, Che-HsiKuo and Yao-Joe Yang (2014) Developing Barbed Microtip-Based Electrode Arrays for Biopotential Measurement. *Sensors.* 14: 12370–12386; doi:10.3390/s140712370.

Laurence Knott. ((2014) Tungsten Poisoning. *Patient.* <http://patient.info/doctor/tungsten-poisoning>.

Liu XX, DeVor RE, Kapoor SG, Ehmann KF. (2005). The Mechanics of Machining at the Microscale: Assessment of the Current State of the Science. ASME. *J. Manuf. Sci. Eng.* 126(4):666-678. doi:10.1115/1.1813469.

Lopez-Gordo MA, D. Sanchez-Morillo and F. Pelayo Valle, (2014). Dry EEG Electrodes *Sensors.* 14:12847–12870; doi: 10.3390/s140712847.

Lun-De Liao, I-Jan Wang, Sheng-Fu Chen, Jyh-Yeong Chang and Chin-Teng Lin. (2011). Design, Fabrication and Experimental Validation of a Novel Dry-Contact Sensor for Measuring Electroencephalography Signals without Skin Preparation. *Sensors.* 11: 5819–5834; doi:10.3390/s110605819, sensors, ISSN 1424-8220.

Luttge L, S.N Bystrova, M.J.A.M Van Putten. (2008). Microneedle array electrode for human EEG recording. ECIFMBE 2008. IFMBE Proceedings 22, pp.1246-1249.

Lyle Hood R, Mehmet A. Kosoglu, Matthew Parker and Christopher G. Rylander. (2011). Effects of Microneedle Design Parameters on Hydraulic Resistance. *J Med Device.*; 5(3):031012–031016. doi:10.1115/1.4004833.

Minjae Kim, Taewan Kim, Dong Sung Kim and Wan Kyun Chung. (2015). Curved Microneedle Array-Based sEMG Electrode for Robust, Long-Term Measurements and High Selectivity. *Sensors*. 15:16265–16280; doi:10.3390/s150716265.

Miyako Arai, Yuya Nishinaka and Norihisa Miki. (2015). Electroencephalogram measurement using polymer-based dry micro needle electrode. *Jpn J Appl Phys*. 2015;54:06FP14 (2015).

Nemani KV, Moodie KL, Brennick JB, Su A, Gimi B. (2013). In vitro and in vivo evaluation of SU-8 biocompatibility. *Mater Sci Eng C Mater Biol Appl*. 33(7):4453-9. doi: 10.1016/j.msec.2013.07.001.

Nitish V. Thakor. (2000) Biopotentials and Electrophysiology Measurement. Copyright 2000 CRC Press LLC. <http://www.engnetbase.com>

Mahoney R, J. E. Cannon, and J. R. Woodworth. (1993). Accelerated UV-aging of acrylic materials used in PV concentrator systems. *Proc. IEEE PVSC* 1216–1221.

McDonald JC, Duffy DC, Anderson JR, Chiu DT, Wu H, Schueller OJ, Whitesides GM. (2000). Fabrication of micro fluidic systems in Poly(dimethoxysiloxane). *Electrophoresis*. 21:27–40.

Mcgrath, J. E., Shultz, A. R., Wightma, J. P., Dimethacrylates, K. (1998). Synthesis and photo polymerization of novel dimethacrylates, M.Sc. Thesis, Balcksburg Univeristy.

Milena Koleva, (200). Poly (methyl methacrylate) (PMMA)  
[webhotel2.tut.fi/projects/cae\\_ds/tekstit/plastics/plastics\\_PMMA.pdf](http://webhotel2.tut.fi/projects/cae_ds/tekstit/plastics/plastics_PMMA.pdf) (May, 05. 2016).

Muhammad Waseem Ashraf, Shahzadi Tayyaba and Nitin Afzulpurkar. (2011). Micro Electromechanical Systems (MEMS) Based Microfluidic Devices for Biomedical Applications. *Int J Mol Sci*. 12(6):3648–3704; doi:10.3390/ijms12063648.

Muhammad Waseem Ashraf, ShahzadiTayyaba, NitinAfzulpurkar, Asim Nisar, Tanom Lomas, Adisorn Tuantranont (2011). Design, Simulation and Fabrication of Silicon Microneedles for Bio-Medical Applications. *CTI Transactions on Electrical Eng., Electronics, and Communications*. Volume 9, No.1 83-91.

- Park JH, Allen MG, Prausnitz, M.R. (2005). Biodegradable polymer micro needles: fabrication, mechanics and transdermal drug delivery. *J Control Release*. 104(1):51–66.
- Park JH, Yong-Kyu Yoon, Seong-O Choi, Mark R Prausnitz, Mark G Allen. (2007). Tapered conical polymer micro needles fabricated using an integrated lens technique for transdermal drug delivery. *IEEE Trans Biomed Eng*. 54(5):903–913 17518288.
- Park JH, Allen MG, Prausnitz MR. (2004). Biodegradable polymer micro needles: fabrication, mechanics and transdermal drug delivery. *Conf Proc IEEE Eng Med Biol Soc*. 4:2654–2657.
- Paillet-Mattei C, et al. (2008). In vivo measurements of the elastic mechanical properties of human skin by indentation tests. *Med Eng Phys*. 30:599–606.
- Patrick Griss, Peter Enoksson, Heli K. Tolvanen-Laakso, Pekka Meriläinen, Stig Ollmar. (2001). Micro machined Electrodes for Biopotential Measurements. *J Microelectro mech Syst*. 10(1). Vol. 10, No. 1, pp. 10-16, Mar 2001.doi: 10.1109/84.911086.
- Patrick Griss. (2002). Characterization of Micro machined Spiked Biopotential Electrodes. *IEEE Trans Biomed Eng*. 49(6):597-604.
- Patrique Fiedler, Jens Haueisen, Dunja Jannek, Stefan Griebel, Lena Zentner, Filipe Vaz and Carlos Fonseca. (2014). Comparison of three types of dry electrodes for Electroencephalography. *Acta Imeko*. Vol. 3, No. 3, pp. 33 – 37.
- Peter Grainge. (2009). Brain-Waves and Altered States of Consciousness, Energy medicine, Issue 165. <http://www.positivehealth.com/article/energy-medicine/brain-waves-and-altered-states-of-consciousness>.
- Pin-Chuan, et al. (2014). An experimental study of micro milling parameters to manufacture micro channels on a PMMA substrate. *Int J Adv Manufact Technol*. 71:1623–1630.

Prasanna Gandhi and Kiran Bhole. (2011) 3D Micro fabrication using bulk lithography, *Proceedings of the ASME 2011*. Paper No. IMECE2011-62473, pp. 393-399; doi:10.1115/IMECE2011-62473.

Puneet Khanna, Kevin Luongo, Joel A. Strom, Shekhar Bhansali. (2010). Axial and shear fracture strength evaluation of silicon micro needles. *Micro Syst. Technol.* 16:973–978, DOI 10.1007/s00542-010-1070-4.

Priyanka Aggarwal and Johnston CR. (2004). Geometrical Effects in Mechanical Characterizing of Microneedle for Biomedical Applications, *NSTI-Nanotech 2004*, www.nsti.org, ISBN 0-9728422-7-6 Vol. 1.

Ragavendra, Prasad Krishna, Mohan Kumar G.C, Balashanmugam. (2014). Effect of Temperature variations on Dimensional stability of bench mark structure fabricated by Scan based Micro stereo lithography. *Int J Adv Inform Sci Technol.* 2014;28:55–60.

Ramasubramanian MK, O M Barham and V Swaminathan. (2008). Mechanics of a mosquito bite with applications to microneedle design. *Bioinspiration & Biomimetics*, IOP Publishing, 3(2008) 046001 (10pp).

Sabbatini, M.E. Renato. (1997). Mapping the Brain.  
<http://www.cerebromente.org.br/n03/tecnologia/eeg.htm> (May, 5, 2016).

Salvo PR, Raedt, E. Carrette, D. Schaubroeck, J. Vanfleteren, L. Cardon (2012). A 3D printed dry electrode for ECG/EEG recording. *Sensors and Actuator. A* 174 (2012) 96–102.

Seong-O Choi<sup>1</sup>, Yeu Chun Kim, Jung-Hwan Park, Joshua Hutcheson, Harvinder S. Gill, Yong-Kyu Yoon, Mark R. Prausnitz, and Mark G. Allen. (2010). An electrically active microneedle array for electroporation. *Biomed Micro Devices.* 12(2):263–273. DOI: 10.1007/s10544-009-9381-x.

Shaun D, Gittard, B.S., Aleksandr Ovsianikov, D.Sc., Nancy A. Monteiro-Riviere, Ph.D., Jason Lusk, M.S., Pierre Morel, M.S., Paola Minghetti, Ph.D., Cristina Lenardi, Ph.D., Boris N. Chichkov, D.Sc., and Roger J. Narayan, M.D., Ph.D.,

(2009). Fabrication of Polymer Microneedles Using a Two-Photon Polymerization and Micromolding Process. *J Diabetes Sci Technol* 3(2):304–311.

Shaun D. Gittard, Philip R. Miller, Chunming Jin, Timothy N. Martin, Ryan D. Boehm, Bret J. Chisholm, Shane J. Stafslie, Justin W. Daniels, Nicholas Cilz, Nancy A. Monteiro-Riviere, Adnan Nasir, and Roger J. Narayan. (2011). Deposition of antimicrobial coatings on microstereolithography-fabricated microneedle, *JOM: the journal of the Minerals, Metals & Materials Society*. Volume 63, Issue 6, pp 59-68.

Shawn P. Davis, Benjamin, J., Landisa, Zachary H. Adamsa, Mark G. Allen, Mark R. Prausnitz. (2004). Insertion of micro needles into skin: measurement and prediction of insertion force and needle fracture force. *J Biomech.* 37:1155–1163.

Sung-Hoon Cho, Hong Meng Lu ; Cauller, L. Romero-Ortega, M.I. ; Jeong-Bong Lee ; Hughes, G. (2008). Biocompatible SU-8-Based microprobes for recording neural Spike signals from regenerated peripheral nerve fibers. *IEEE Sensors Journal*, Vol. 8, No. 11.

Takhs, E. & Wojnarovits. (1997), Kinteic study on radiation-induced polymerisation of HDDA and HDDMA, *Nuclear Instruments and Methods in Physics Research*, 131, 295-299.

Teemu Rämö, 2006, Biopotentials and Electrophysiology Measurement *metrology*, [tkk.fi/courses/S-108.4010/2006/Biopotentials.ppt](http://tkk.fi/courses/S-108.4010/2006/Biopotentials.ppt) (May, 05 2016).

Teplan M. (2002). Fundamentals of EEG Measurement, *Measurement Science Review*, Vol.2, Section 2, 2002.

Victoria L, Finkenstadt, LinShu Liu, J. L. Willett. (2007). Evaluation of Poly(lactic acid) and Sugar Beet Pulp Green Composites. *J Polym Environ.* 15:1–6.

Varadan, V. K., Jiang, X., Varadan, V., V. (2001). *Microstereolithography and other fabrication Techniques for 3D MEMS*, John Wiley & Sons Inc., Chichester.

Vanlerberghe F, M. De Volder, M. Op de Beeck, J. Penders, D. Reynaerts, R. Puers, C. Van Hoof (2011). 2-Scale Topography Dry Electrode for Biopotential Measurements *Proc. IEEE EMBS*.2011:1892-5. DOI: 10.1109/IEMBS.2011.6090536.

Wilke N, A. Mulcahy, S.-R. Ye, A. Morrissey. (2005). Process optimization and characterization of silicon micro needles fabricated by wet etch technology. *Microelectron J.* 36:650–656.

Yu LM, Francis E. H. Tay, D. G. Guo, L. Xu, M. N. Nyan, F. W. Chong, K. L. Yap, B. Xu. (2008). A MEMS-based Bio electrode for ECG measurement. *Proc. IEEE Sensors 2008 Conference.* 1068-71. DOI: 10.1109/ICSENS.2008.4716627.

Yu Mike Chi. (2010). Dry-Contact and Noncontact Biopotential Electrodes Methodological Review/ IEEE Reviews In Biomedical Engineering, Vol. 3, pp 106-119.

Yuli Lin and C-H Kuo. (2007). Adhesion Strength Measurement of Ni Coating on PMMA and PU Substrate. *Micro sc Microanal.* 13(2).

Yusuf K, Demir1, Akan Z, Kerimoglu O. (2013). Characterization of Polymeric Microneedle Arrays for Transdermal Drug Delivery. *PLoS ONE.* 8(10): e77289.doi:10.1371/journal.pone.0077289.

Zahn D. Jeffrey, Neil H. Talbot, Dorian Liepmann, and Albert P. Pisano. 2000. Micro fabricated Polysilicon Microneedles for Minimally Invasive Biomedical Devices, *Biomedical Micro devices* 2:4, 295-303.

## LIST OF PUBLICATIONS

Sl. No.	Title of the Paper	Authors (In the same order as in the paper, underline the Research Scholar's name)	Name of the Journal / Conference / Symposium, Vol., No., Pages	Month & Year of Publication	Category *
1.	System and Method for making micro needles using micro stereolithography	K.Ankit, N.Balashanmugam, R.S.Suresh, L.Sudha, A.D. Gandhi, B.R.Satyan, P.V.Shashikumar, Prasad Krishna, G.C.Mohankumar	Patent Application No.: 660/CHE/2015	Patent Filed date: 11.2.15	Patent
2.	Fabrication of Polymeric Micro needle Array by Micro machining & Micro molding	N.Balashanmugam, K.Naveen, Prasad Krishna, G.C.Mohan Kumar,	Int. of Engineering and Innovative Technology (IJEIT)	Volume 5, Issue 6, December 2015	Journal
3.	Design and development of microneedle array based	<u>N Balashanmugama</u> , Naveen K, Prasad Krishna, G C Mohan Kumar	Int. Journal of Nano Mfg.	In Press	Journal

	electrode for bio potential measurement				
4.	Mechanical Characterisation of UV Photo-Polymerised PMMA with different Photo-Initiator Concentration.	<u>N.Balashanmugam</u> , K.Naveen, A.D.Gandhi, P.V.Shashikumar, Prasad Krishna, G.C.Mohan Kumar	International Conference on Polymer Composites, NITK Surathkal,	Dec-19-20, 2014	Conference
5.	STL-less based CAD/CAM approach for Laser Scanning in Micro Stereo Lithography	N.Balashanmugam, Ankit. K, Narashimalu, Prasad Krishna, Arun M.Umarji, P.V.Shashikumar	ICAMME 2014, NITK Surathkal,	March 26-29, 2014.	Conference

\* Category: 1 : Journal paper, full paper reviewed  
2 : Journal paper, Abstract reviewed  
3 : Conference/Symposium paper, full paper reviewed  
4 : Conference/Symposium paper, abstract reviewed  
5 : others (including papers in Workshops, NITK Research Bulletins, Short notes etc.)  
(If the paper has been accepted for publication but yet to be published, the supporting documents must be attached.)

**Research Scholar**  
Name & Signature, with Date

**Research Guide/s**  
Name & Signature, with Date

## BIO DATA

1. Name: Balashanmugam. N
2. Father's Name: K. Natchimuthu
3. Date of Birth: 24-07-1961
4. Nationality: Indian
5. Marital Status: Married
6. Present Position: Joint Director, CMTI, Tumkur Road, Bangalore-560022
7. Address:  
Permanent Address  
Tuscany, 824, 8<sup>th</sup> Cross, 26<sup>th</sup> Main,  
I Sector, HSR Layout, Bangalore-560102  
Present Address  
Tuscany, 824, 8<sup>th</sup> Cross, 26<sup>th</sup> Mn, I Sector  
I Sector, HSR Layout, Bangalore-560102
8. Mobile Number: +91-9449842676
9. E-mail id.: balashanmugam.cmti@nic.in
10. Educational Qualification

Qualification	College/school	University/Board	Year of Passing	Performance
Ph.D. in Mechanical Engineering	National Institute of Technology Karnataka	National Institute of Technology Karnataka	Pursuing	8.5
M.E. in Production Engineering	P.S.G. College of Technology, Coimbatore	Madras University	1985	85%
B. E (Hons) in Mechanical Engineering	P.S.G. College of Technology, Coimbatore	Bharathiar University	1983	75%

I declare that above information is true and correct to best of my knowledge.

*(N.Balashanmugam)*



## APPENDIX I

Results of FEM analysis: Skin Penetration and Needle Strain for a Load of 2N

Load 2N										
Pitch	0.3 mm		0.4 mm		0.5 mm		0.6 mm		0.7 mm	
Base Dia. (mm)	Skin Penetration (mm)	Needle Strain								
<b>0.05</b>	0.05521	0.039203	0.039541	0.02280	0.034209	0.02299	0.027108	0.01529	0.027168	0.018418
<b>0.06</b>	0.05442	0.037571	0.039241	0.02193	0.033435	0.02141	0.026433	0.01511	0.026656	0.017701
<b>0.07</b>	0.0544	0.038204	0.038788	0.02161	0.03344	0.02190	0.026193	0.01514	0.026108	0.017531
<b>0.08</b>	0.052276	0.033979	0.037751	0.01993	0.03236	0.01958	0.025347	0.01429	0.025059	0.015758
<b>0.09</b>	0.051867	0.032604	0.037236	0.01984	0.031335	0.02029	0.02494	0.01429	0.024811	0.016133
<b>0.10</b>	0.051772	0.032451	0.0374	0.02007	0.03115	0.02023	0.024832	0.01423	0.024741	0.016346
<b>0.11</b>	0.054103	0.029682	0.038643	0.01725	0.031595	0.03159	0.025386	0.01286	0.025042	0.015667
<b>0.12</b>	0.054362	0.029977	0.03868	0.01703	0.031592	0.01835	0.025886	0.01252	0.024772	0.015189

Results of FEM analysis: Skin Penetration and Needle Strain for a Load of 3N

Pitch	0.3 mm		0.4 mm		0.5 mm		0.6 mm		0.7 mm	
Base Diameter (mm)	Skin Penetration (mm)	Needle Strain								
0.05	0.082333	0.05733	0.059311	0.03420	0.051441	0.03439	0.040662	0.02294	0.040752	0.02762
0.06	0.081942	0.05611	0.058862	0.03289	0.050223	0.03202	0.039649	0.02267	0.039984	0.02655
0.07	0.082052	0.05691	0.058182	0.03241	0.05021	0.03279	0.039289	0.02271	0.039162	0.02629
0.08	0.077716	0.05015	0.056626	0.02989	0.048747	0.02914	0.038021	0.02144	0.037588	0.02363
0.09	0.077944	0.04864	0.055854	0.02976	0.046905	0.03050	0.03741	0.02143	0.037216	0.0242
0.10	0.077747	0.04856	0.0561	0.03011	0.046726	0.03035	0.037249	0.02134	0.037111	0.02451
0.11	0.081721	0.04580	0.057965	0.02587	0.047392	0.02843	0.037978	0.01936	0.037562	0.02350
0.12	0.081662	0.04483	0.05802	0.02554	0.047388	0.02752	0.038764	0.01883	0.037157	0.02278

Results of FEM analysis: Skin Penetration and Needle Strain for a Load of 4 N

Pitch	0.3 mm		0.4 mm		0.5 mm		0.6 mm		0.7 mm	
Base Dia. (mm)	Skin Penetration (mm)	Needle Strain								
0.05	0.109769	0.07646	0.079083	0.04560	0.068588	0.04585	0.054216	0.03059	0.054337	0.03683
0.06	0.10918	0.07501	0.078483	0.04386	0.066869	0.04283	0.052865	0.03022	0.053311	0.03540
0.07	0.107982	0.07422	0.077576	0.04322	0.066117	0.04454	0.052386	0.03029	0.052215	0.03506
0.08	0.103619	0.06687	0.075502	0.03985	0.065008	0.03892	0.050694	0.02859	0.050117	0.03151
0.09	0.103733	0.06520	0.074471	0.03968	0.062539	0.04067	0.049879	0.02858	0.049622	0.03226
0.10	0.104088	0.06503	0.0748	0.04015	0.062301	0.04047	0.049664	0.02846	0.049481	0.03269
0.11	0.108965	0.06106	0.077285	0.03449	0.063189	0.03790	0.050639	0.02581	0.050083	0.03133
0.12	0.108882	0.05978	0.077359	0.03406	0.063185	0.03670	0.051684	0.02510	0.049543	0.03037

Results of FEM analysis: Skin Penetration and Needle Strain for a Load of 5 N

Pitch (mm)	0.3 mm		0.4 mm		0.5 mm		0.6 mm		0.7 mm	
Base Diameter (mm)	Skin Penetrati on (mm )	Needle Strain								
0.05	0.13721	0.0955	0.09885	0.05700	0.08552	0.05749	0.06777	0.03824	0.06792	0.04604
0.06	0.13632	0.0937	0.0981	0.05483	0.08359	0.0535	0.06608	0.03778	0.06664	0.04425
0.07	0.13639	0.0951	0.09697	0.05402	0.0836	0.05476	0.06548	0.03786	0.06506	0.04395
0.08	0.13069	0.0849	0.09438	0.04982	0.08128	0.04857	0.06337	0.03574	0.06265	0.03939
0.09	0.13083	0.0816	0.09309	0.0496	0.07817	0.05084	0.06235	0.03573	0.06203	0.04033
0.1	0.12958	0.0809	0.0935	0.05019	0.07785	0.05056	0.06208	0.03558	0.06185	0.04086
0.11	0.13489	0.0746	0.09661	0.04312	0.07899	0.04738	0.06346	0.03217	0.0626	0.03916
0.12	0.1359	0.0749	0.0967	0.04257	0.07898	0.04588	0.06461	0.03138	0.06193	0.03797

Results of FEM analysis: Skin Penetration and Needle Strain for a Load of 6 N

Pitch	0.3 mm		0.4 mm		0.5 mm		0.6 mm		0.7 mm	
Base Diameter (mm)	Skin Penetration (mm)	Needle Strain								
0.05	0.16467	0.11467	0.11862	0.06841	0.10262	0.06900	0.08132	0.0458	0.0815	0.05525
0.06	0.16358	0.11246	0.11772	0.06579	0.10051	0.06395	0.0793	0.0453	0.07997	0.0531
0.07	0.16367	0.11415	0.11636	0.06483	0.09891	0.06701	0.07858	0.0454	0.07832	0.05259
0.08	0.15543	0.10031	0.11325	0.05978	0.09753	0.05829	0.07604	0.0428	0.07518	0.04727
0.09	0.15698	0.09802	0.11171	0.05952	0.09381	0.06101	0.07482	0.0428	0.07443	0.0484
0.1	0.15613	0.09756	0.1122	0.06023	0.09342	0.06067	0.0745	0.0426	0.07422	0.04903
0.11	0.16327	0.09189	0.11593	0.05174	0.09478	0.05686	0.07596	0.0387	0.07512	0.04700
0.12	0.16333	0.08972	0.11604	0.05109	0.09478	0.05505	0.07766	0.0375	0.07431	0.04556

Results of FEM analysis: Skin Penetration and Needle Strain for a Load of 7 N

Pitch	0.3 mm		0.4 mm		0.5 mm		0.6 mm		0.7 mm	
Base Diameter (mm)	Skin Penetration (mm)	Needle Strain								
0.05	0.19320	0.13383	0.13355	0.07428	0.11531	0.08294	0.09228	0.05784	0.08967	0.06202
0.06	0.19065	0.12905	0.13087	0.07072	0.11432	0.08111	0.09020	0.05353	0.08782	0.06018
0.07	0.18995	0.12663	0.13045	0.06847	0.1143	0.07755	0.08839	0.05306	0.08752	0.05921
0.08	0.18238	0.11540	0.12711	0.06429	0.10908	0.06879	0.08611	0.05059	0.08641	0.05258
0.09	0.18288	0.11090	0.12609	0.06285	0.11129	0.06805	0.08637	0.04925	0.08518	0.05337
0.1	0.1815	0.10994	0.12778	0.06322	0.11015	0.06512	0.08692	0.04965	0.08576	0.05212
0.11	0.18836	0.09991	0.13032	0.05738	0.11147	0.06367	0.08852	0.04655	0.08709	0.04993
0.12	0.1909	0.10253	0.12892	0.05499	0.10468	0.07110	0.08848	0.04602	0.08606	0.04893

Results of FEM analysis: Skin Penetration and Needle Strain for a Load of 8 N

Pitch	0.3 mm		0.4 mm		0.5 mm		0.6 mm		0.7 mm	
Base Diameter (mm)	Skin Penetration (mm)	Needle Strain								
0.05	0.21954	0.15292	0.15817	0.09120	0.13718	0.09170	0.10843	0.0611	0.10936	0.07306
0.06	0.21846	0.14979	0.15697	0.08772	0.13374	0.08566	0.10573	0.0604	0.10662	0.07080
0.07	0.21881	0.15177	0.15515	0.08644	0.13376	0.08761	0.10477	0.0605	0.10409	0.07033
0.08	0.20773	0.13333	0.151	0.07971	0.12966	0.07822	0.10139	0.0571	0.10023	0.06303
0.09	0.20932	0.13067	0.14894	0.07936	0.12508	0.08135	0.09976	0.0571	0.09924	0.06453
0.1	0.20946	0.12877	0.1496	0.08031	0.1246	0.08095	0.09933	0.0569	0.09896	0.06538
0.11	0.21769	0.12253	0.15457	0.06899	0.12638	0.07581	0.10154	0.0514	0.10017	0.06266
0.12	0.21776	0.11956	0.15472	0.06812	0.12637	0.07340	0.10337	0.0502	0.09909	0.06075

Results of FEM analysis: Skin Penetration and Needle Strain for a Load of 9 N

Pitch	0.3 mm		0.4 mm		0.5 mm		0.6 mm		0.7 mm	
Base Diameter (mm)	Skin Penetration (mm)	Needle Strain								
0.05	0.24841	0.17206	0.1717	0.0955	0.14854	0.1066	0.11864	0.07437	0.11522	0.0796
0.06	0.24512	0.16593	0.16826	0.0909	0.14698	0.1042	0.11597	0.06884	0.11292	0.0773
0.07	0.24423	0.16279	0.16772	0.0880	0.14696	0.0997	0.11366	0.06797	0.11255	0.0761
0.08	0.23451	0.1483	0.16347	0.0825	0.14006	0.0907	0.11081	0.06499	0.11127	0.0675
0.09	0.23513	0.14261	0.16184	0.0810	0.14267	0.0871	0.11142	0.06306	0.10929	0.0687
0.1	0.23335	0.14135	0.16298	0.0821	0.14151	0.0862	0.11159	0.06386	0.11027	0.0669
0.11	0.24218	0.12845	0.16715	0.0741	0.14332	0.0818	0.11382	0.05985	0.11198	0.0642
0.12	0.24544	0.13183	0.16576	0.0707	0.13458	0.0914	0.11376	0.05917	0.11094	0.0626

Results of FEM analysis: Skin Penetration and Needle Strain for a Load of 10 N

Pitch	0.3 mm		0.4 mm		0.5 mm		0.6 mm		0.7 mm	
Base Diameter (mm)	Skin Penetration (mm)	Needle Strain								
0.05	0.27442	0.19115	0.19771	0.11401	0.17104	0.11499	0.13554	0.07649	0.1367	0.09133
0.06	0.27263	0.18745	0.1962	0.10966	0.16688	0.10739	0.13217	0.07557	0.13328	0.08850
0.07	0.27277	0.19028	0.19394	0.10805	0.16737	0.10932	0.13096	0.07572	0.13012	0.08791
0.08	0.25966	0.16667	0.18876	0.09964	0.16259	0.09714	0.12674	0.07149	0.12529	0.07879
0.09	0.26165	0.16333	0.18618	0.09920	0.15667	0.10145	0.12470	0.07146	0.12405	0.08066
0.1	0.26183	0.16096	0.187	0.10039	0.1557	0.10112	0.12416	0.07116	0.1237	0.08172
0.11	0.27241	0.15266	0.19322	0.08624	0.15797	0.09476	0.12693	0.06433	0.12521	0.07833
0.12	0.27221	0.14954	0.19340	0.08515	0.15796	0.09176	0.12921	0.06277	0.12386	0.07594



## APPENDIX II

### PLOTS ON PENETRATION, STRAIN VS. BASE DIAMETER FOR APPLIED LOADS OF 2 N TO 10 N

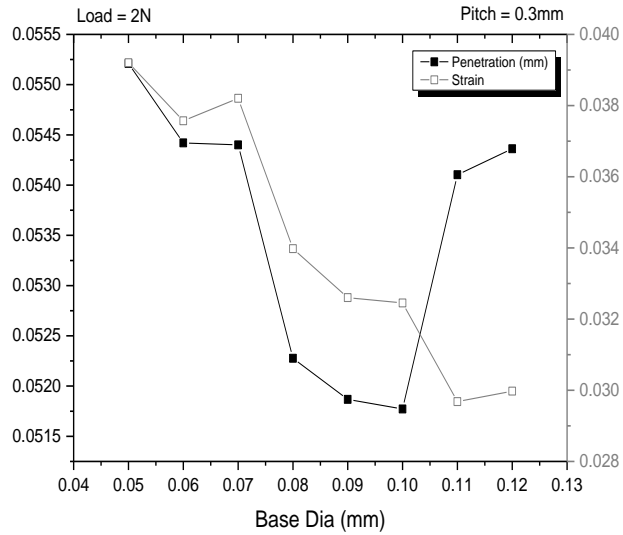


**Figure 10.1** Plot on Penetration, Strain vs. Base Diameter at 2 N Load for a Pitch 0.3 mm

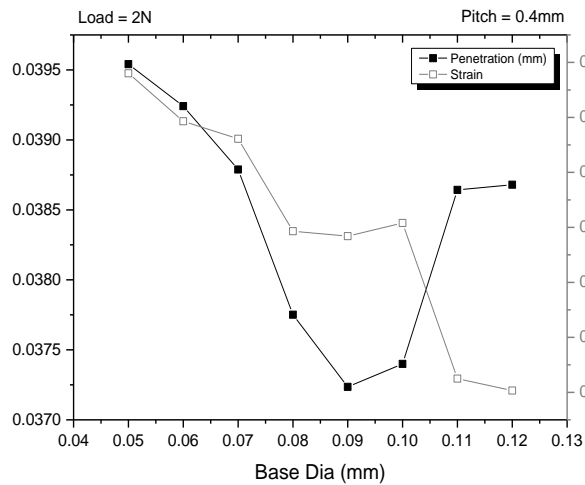


**Figure 10.2** Plot on Penetration, Strain vs. Base Diameter at 2 N Load for a Pitch 0.4 mm

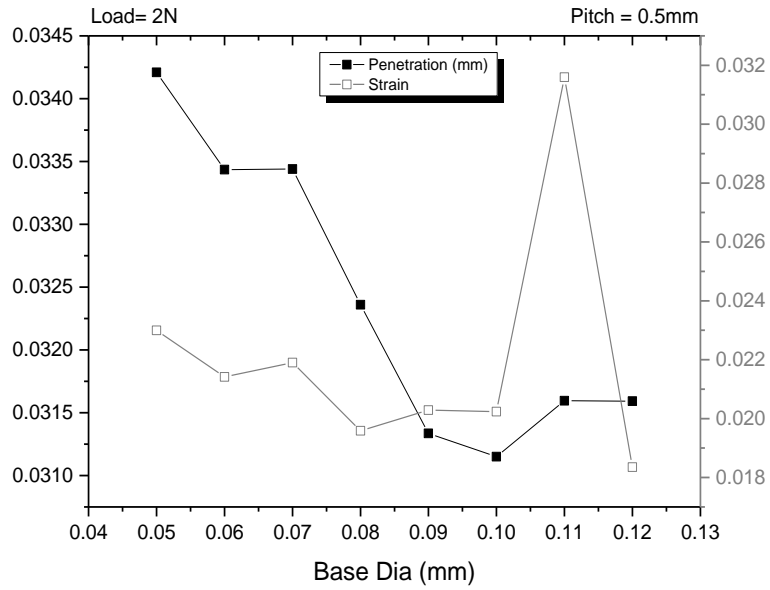


**Figure 10.3** Plot on Penetration, Strain vs. Base Dia. at 2 N Load for a Pitch 0.5 mm

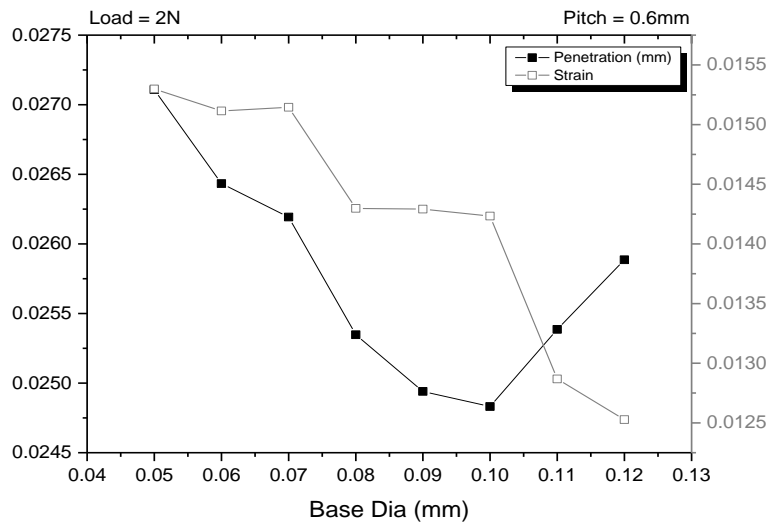


**Figure 10.4** Plot on Penetration, Strain vs. Base Dia. at 2 N Load for a Pitch 0.6 mm

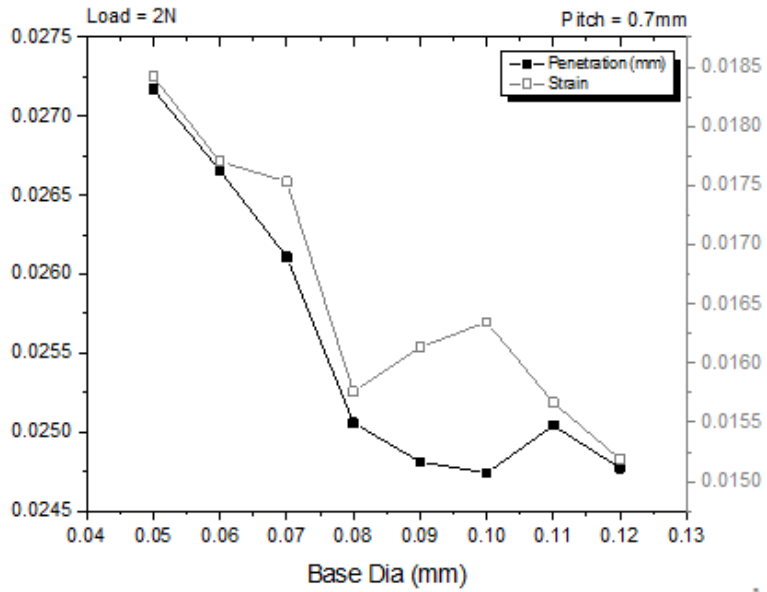


**Figure 10.5** Plot on Penetration, Strain vs. Base Dia. at 2 N Load for a Pitch 0.7 mm

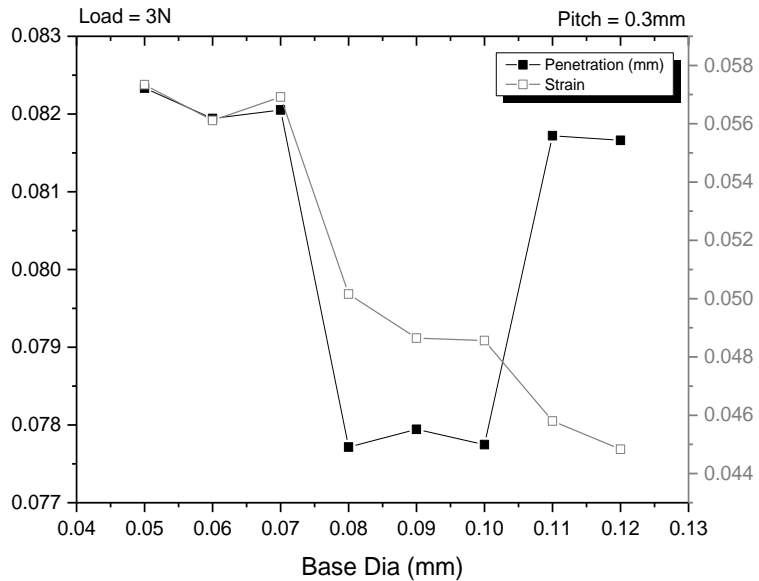


**Figure 10.6** Plot on Penetration, Strain vs. Base Dia. at 3 N Load for a Pitch 0.3 mm

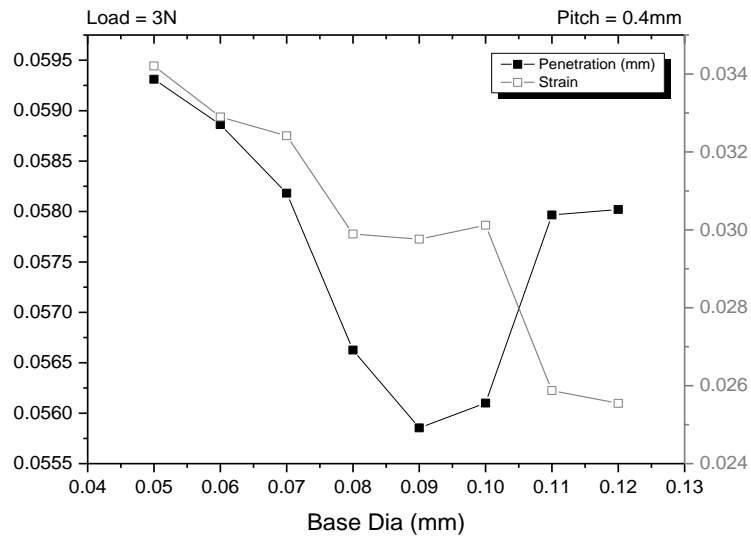


**Figure 10.7** Plot on Penetration, Strain vs. Base Dia. at 3 N Load for a Pitch 0.4 mm

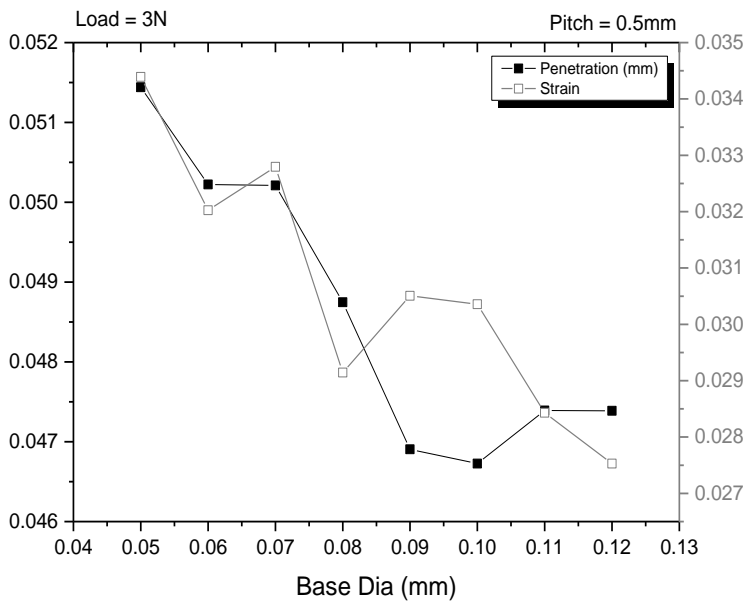


**Figure 10.8** Plot on Penetration, Strain vs. Base Dia. at 3 N Load for a Pitch 0.5 mm

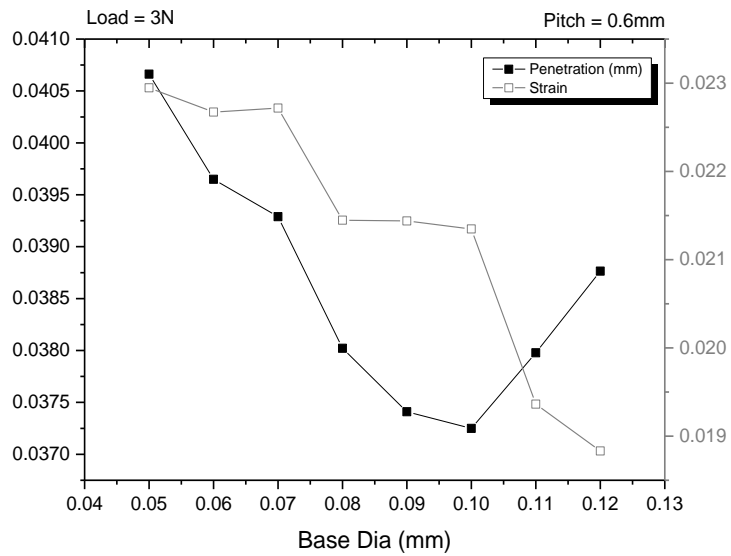


**Figure 10.9** Plot on Penetration, Strain vs. Base Dia. at 3 N Load for a Pitch 0.6 mm

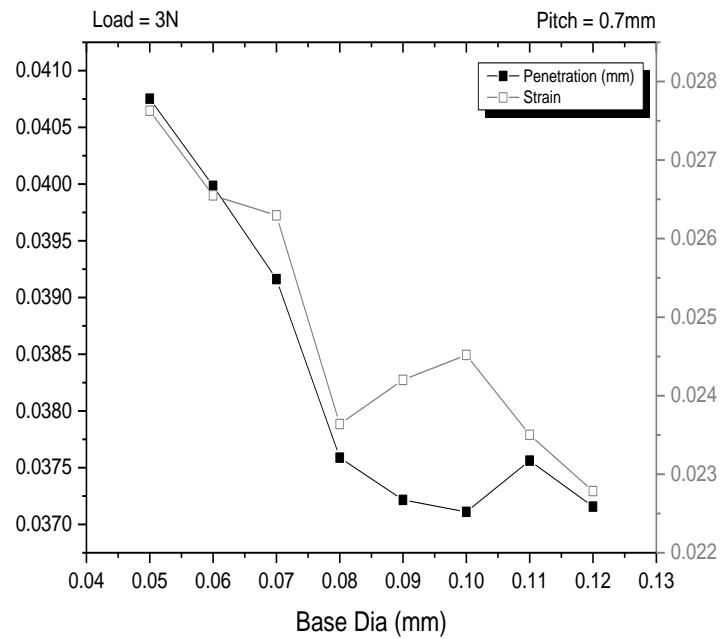


**Figure 10.10** Plot on Penetration, Strain vs. Base Dia. at 3 N Load for a Pitch 0.7 mm

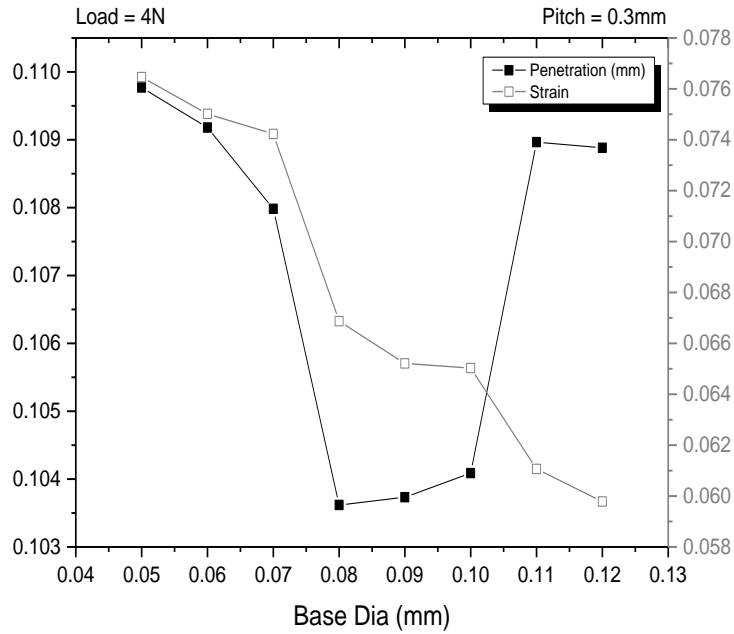


**Figure 10.411** Plot on Penetration, Strain vs. Base Dia. at 4 N Load for a Pitch 0.3 mm

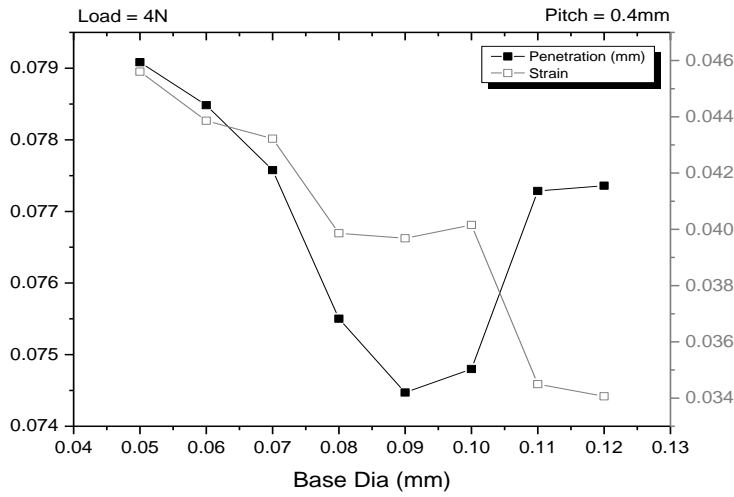


**Figure 10.12** Plot on Penetration, Strain vs. Base Dia. at 4 N Load for a Pitch 0.4 mm

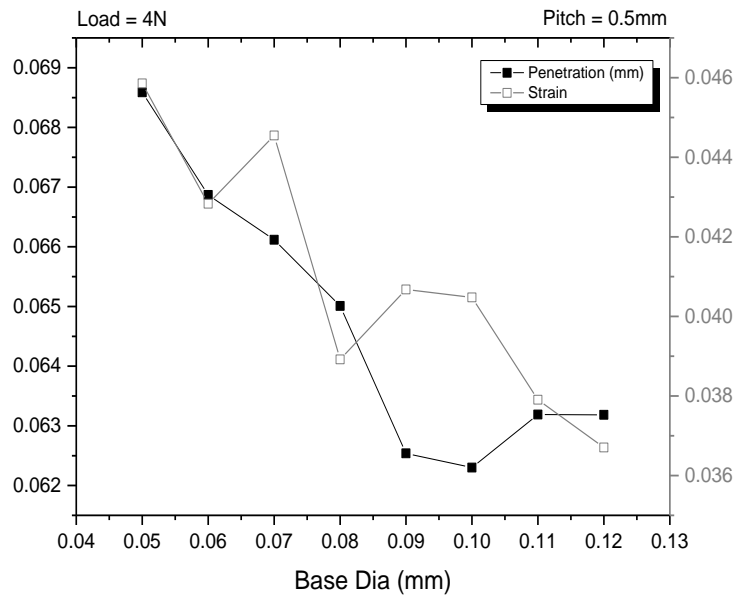


**Figure 10.13** Plot on Penetration, Strain vs. Base Dia. at 4 N Load for a Pitch 0.5 mm

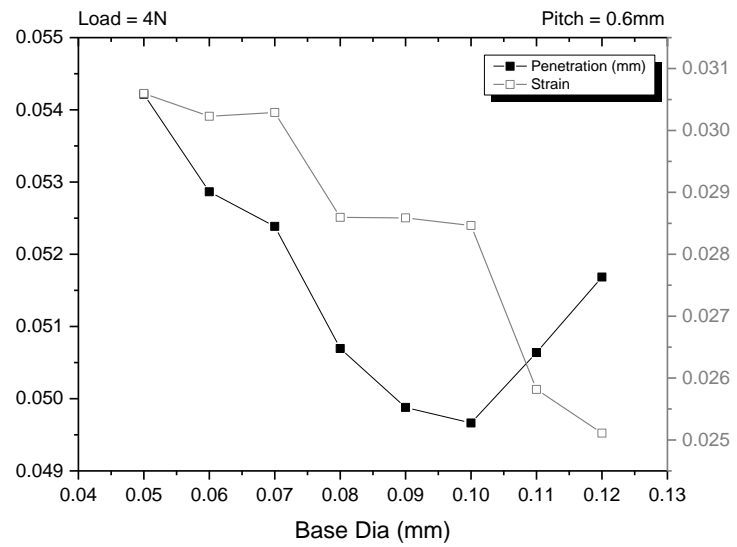


**Figure 10.14** Plot on Penetration, Strain vs. Base Dia. at 4 N Load for a Pitch 0.6 mm

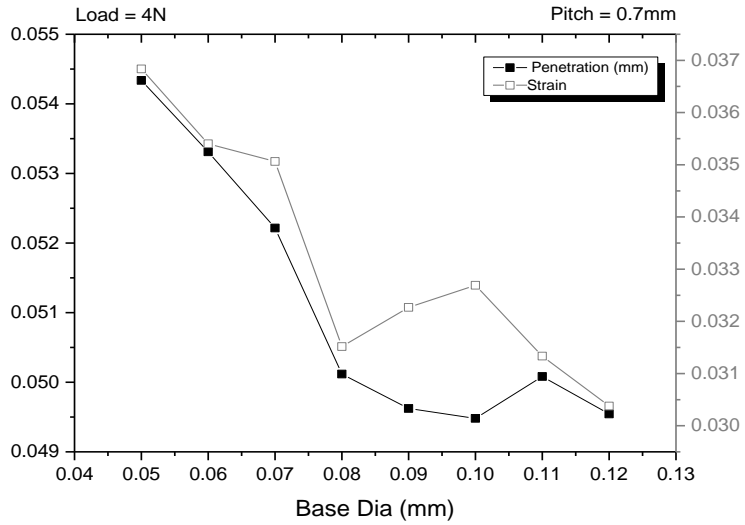


**Figure 10.15** Plot on Penetration, Strain vs. Base Dia. at 4 N Load for a Pitch 0.7 mm

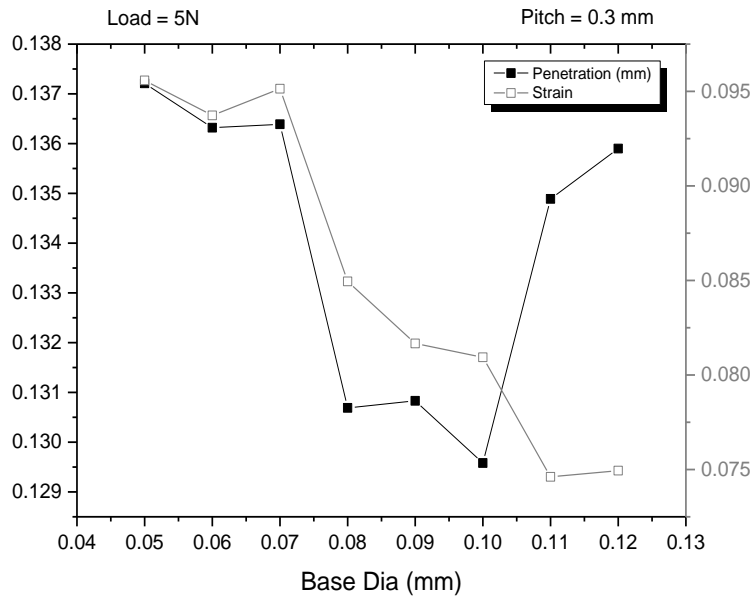


**Figure 10.16** Plot on Penetration, Strain vs. Base Dia. at 5 N Load for a Pitch 0.3 mm

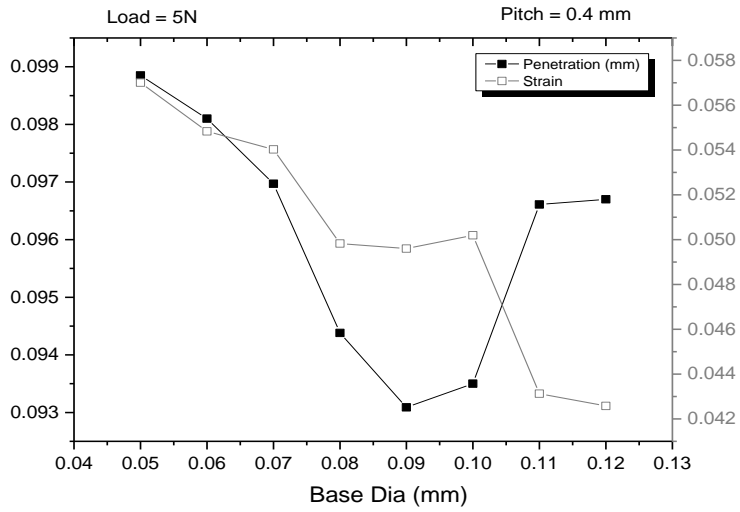


**Figure 10.17** Plot on Penetration, Strain vs. Base Dia. at 5 N Load for a Pitch 0.4 mm

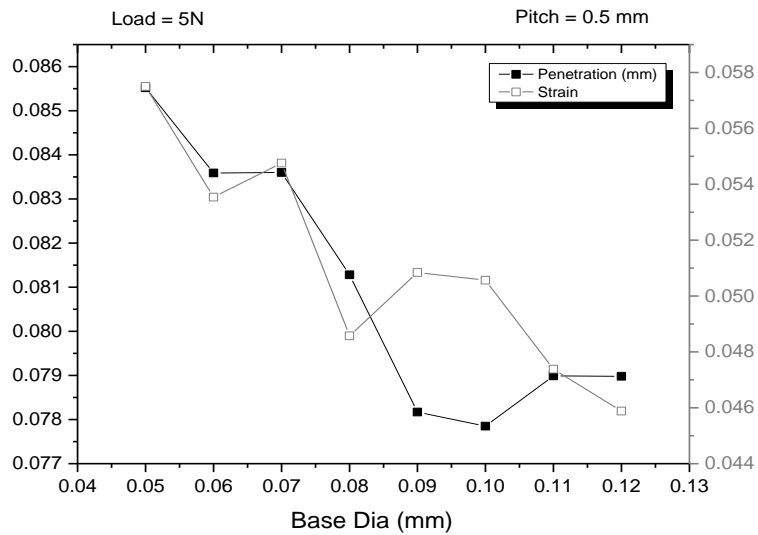


**Figure 10.18** Plot on Penetration, Strain vs. Base Dia. at 5 N Load for a Pitch 0.5 mm

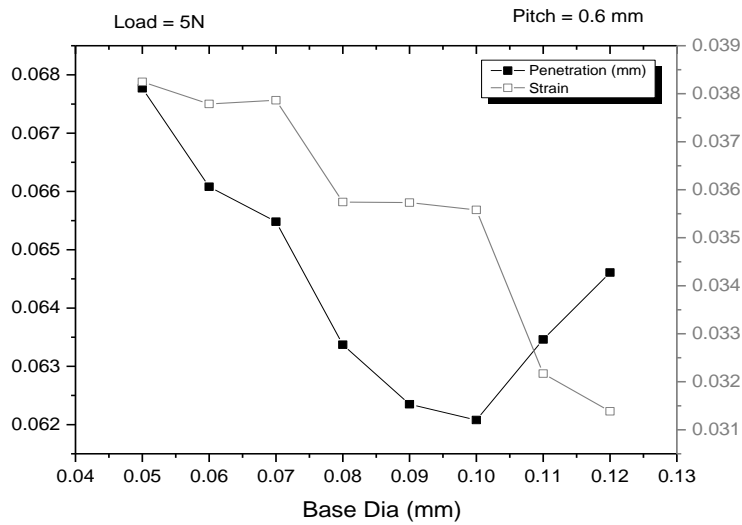


**Figure 10.19** Plot on Penetration, Strain vs. Base Dia. at 5 N Load for a Pitch 0.6 mm

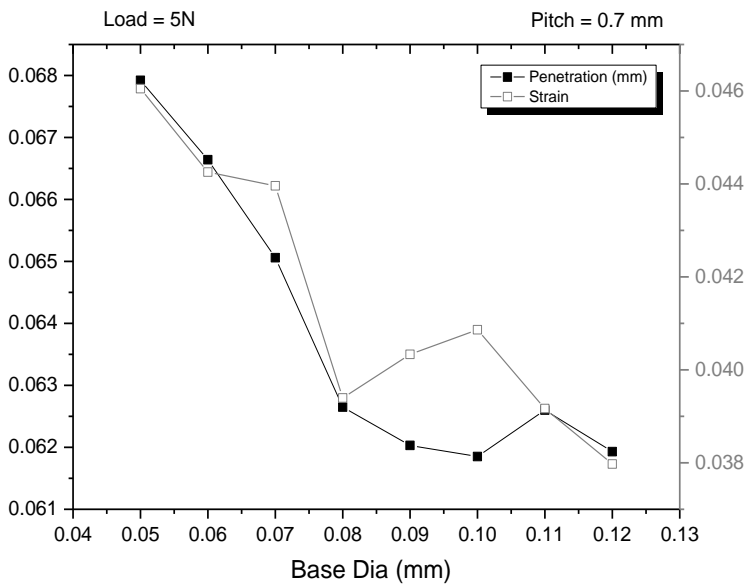


**Figure 10.20** Plot on Penetration, Strain vs. Base Dia. at 5 N Load for a Pitch 0.7 mm

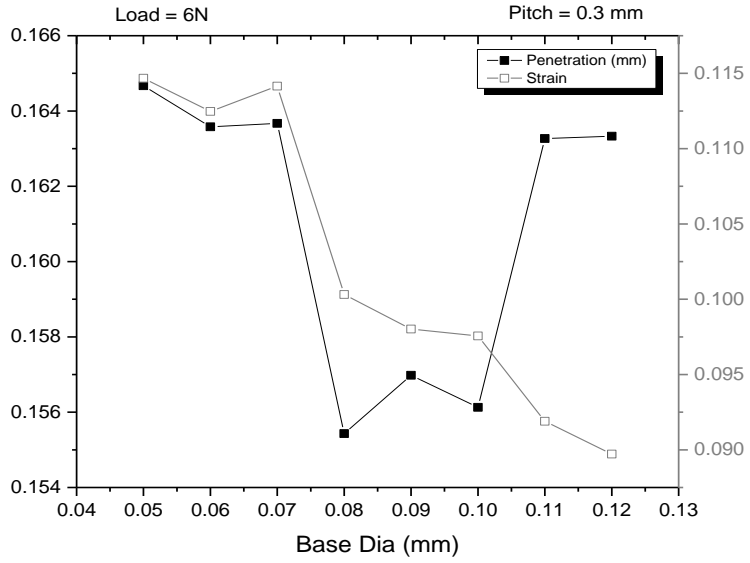


**Figure 10.21** Plot on Penetration, Strain vs. Base Dia. at 6 N Load for a Pitch 0.3 mm

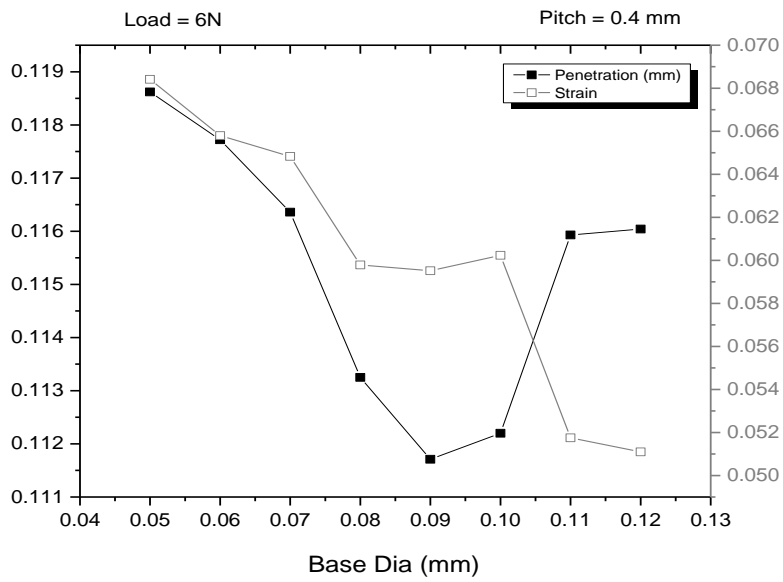


**Figure 10.22** Plot on Penetration, Strain vs. Base Dia. at 6 N Load for a Pitch 0.4 mm

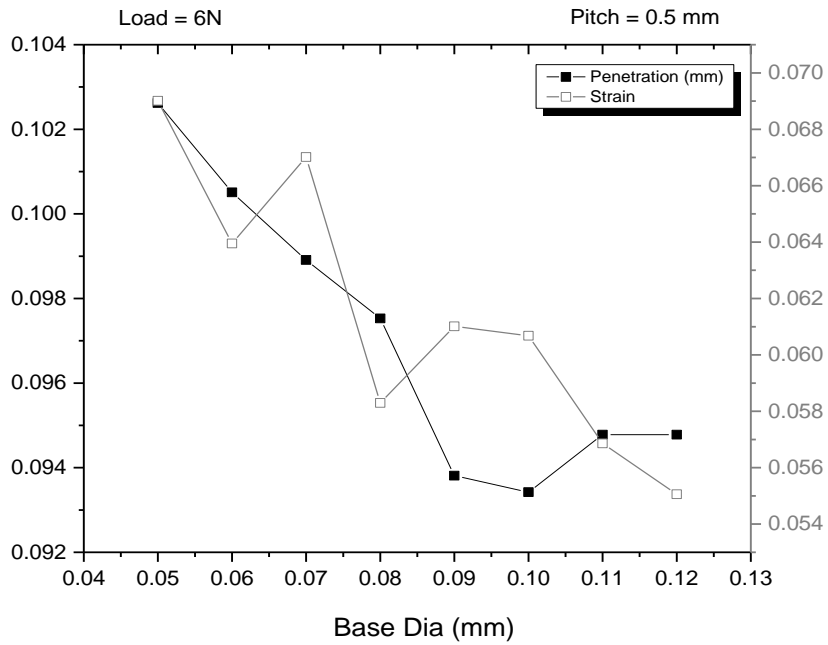


**Figure 10.23** Plot on Penetration, Strain vs. Base Dia. at 6 N Load for a Pitch 0.5 mm

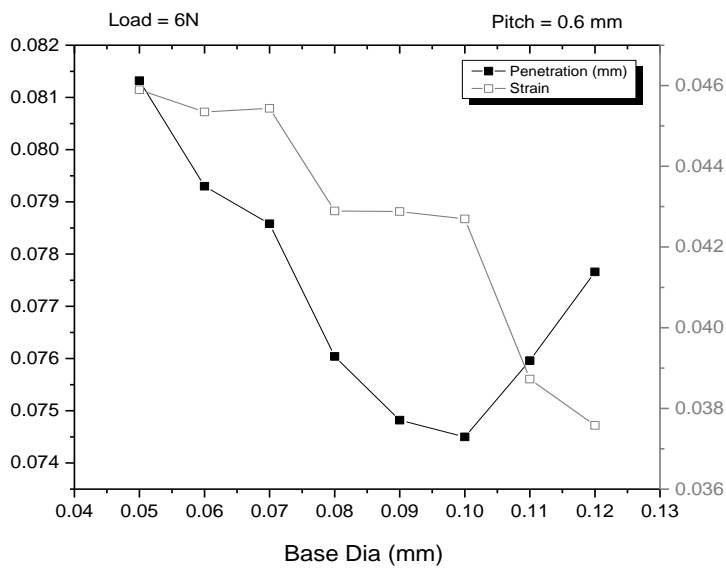


**Figure 10.24** Plot on Penetration, Strain vs. Base Dia. at 6 N Load for a Pitch 0.6 mm

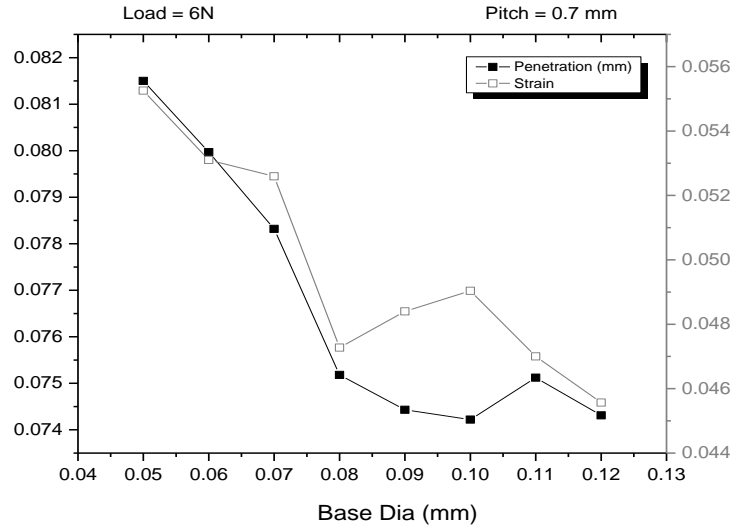


**Figure 10.25** Plot on Penetration, Strain vs. Base Dia. at 6 N Load for a Pitch 0.7 mm

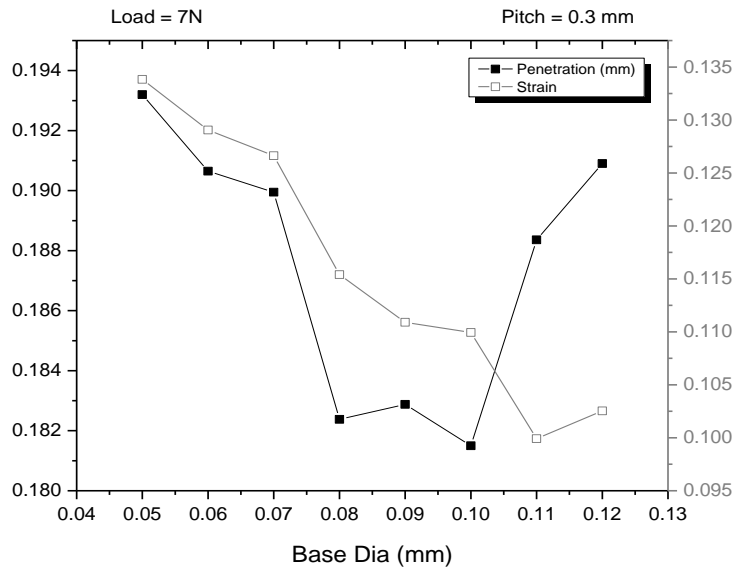


**Figure 10.26** Plot on Penetration, Strain vs. Base Dia. at 7 N Load for a Pitch 0.3 mm

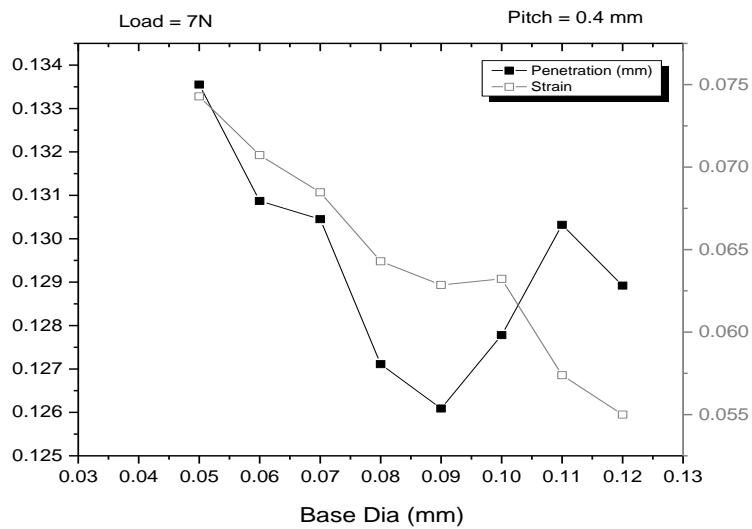


**Figure 10.27** Plot on Penetration, Strain vs. Base Dia. at 7 N Load for a Pitch 0.4 mm

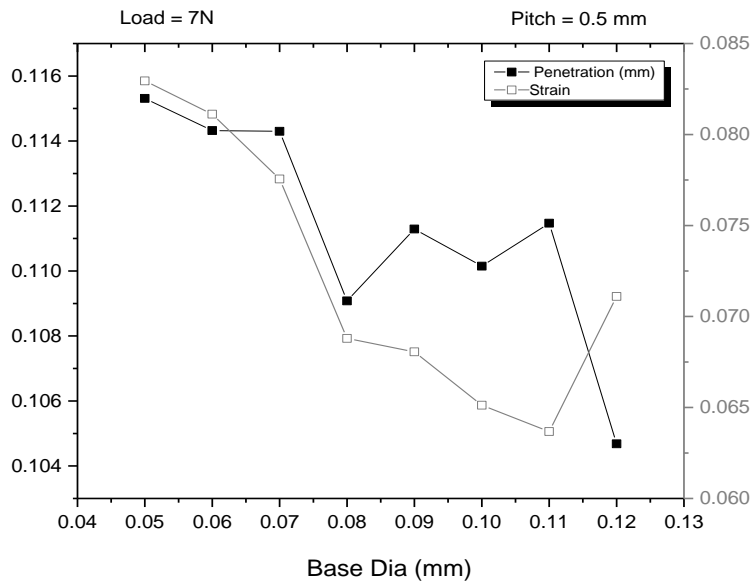


**Figure 10.28** Plot on Penetration, Strain vs. Base Dia. at 7 N Load for a Pitch 0.5 mm

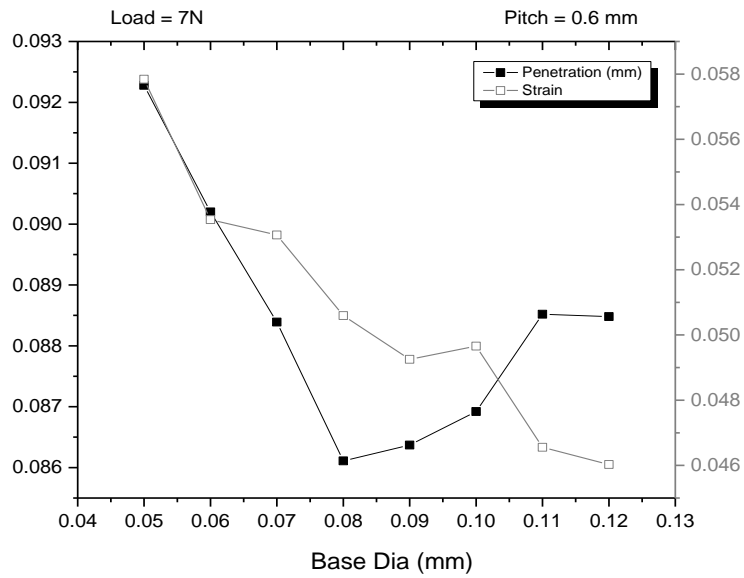


**Figure 10.29** Plot on Penetration, Strain vs. Base Dia. at 7 N Load for a Pitch 0.6 mm

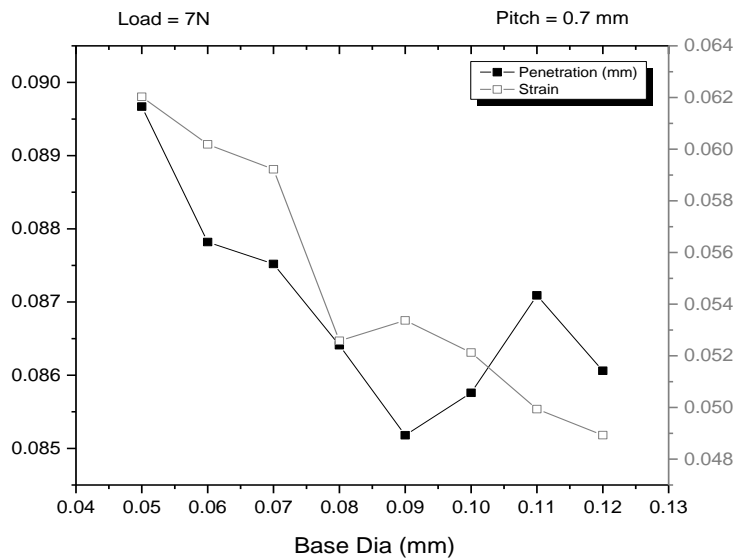


**Figure 10.30** Plot on Penetration, Strain vs. Base Dia. at 7 N Load for a Pitch 0.7 mm

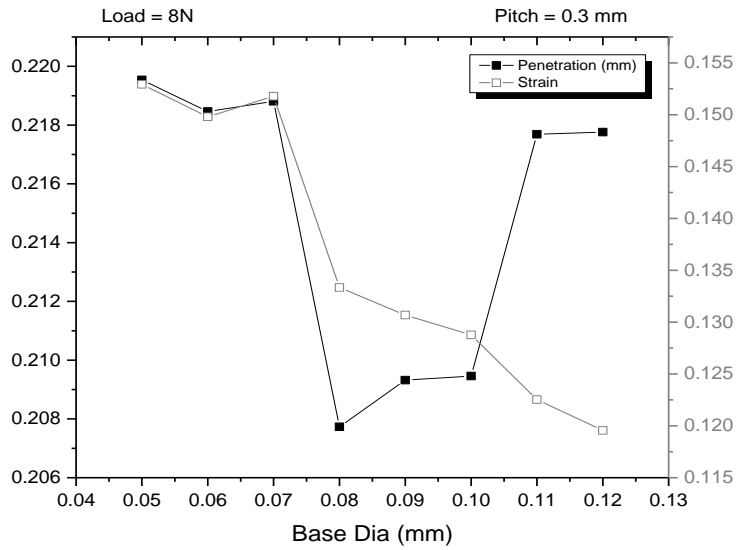


**Figure 10.31** Plot on Penetration, Strain vs. Base Dia. at 8 N Load for a Pitch 0.3 mm

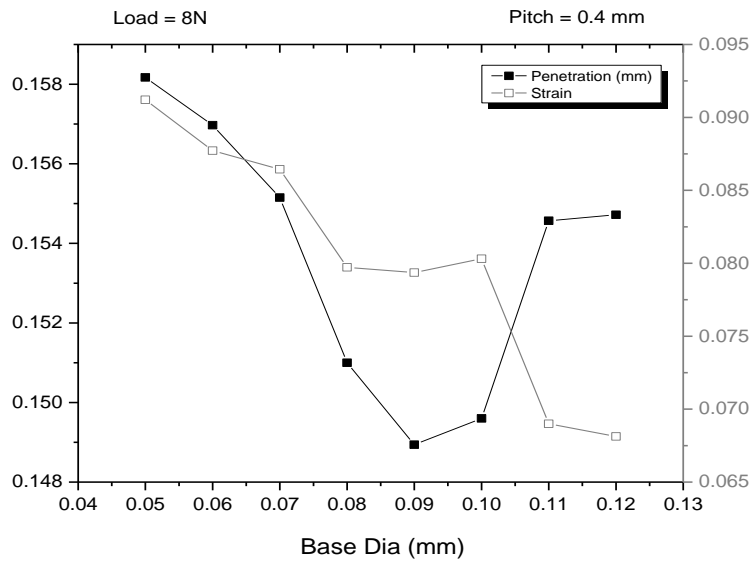


**Figure 10.32** Plot on Penetration, Strain vs. Base Dia. at 8 N Load for a Pitch 0.4 mm

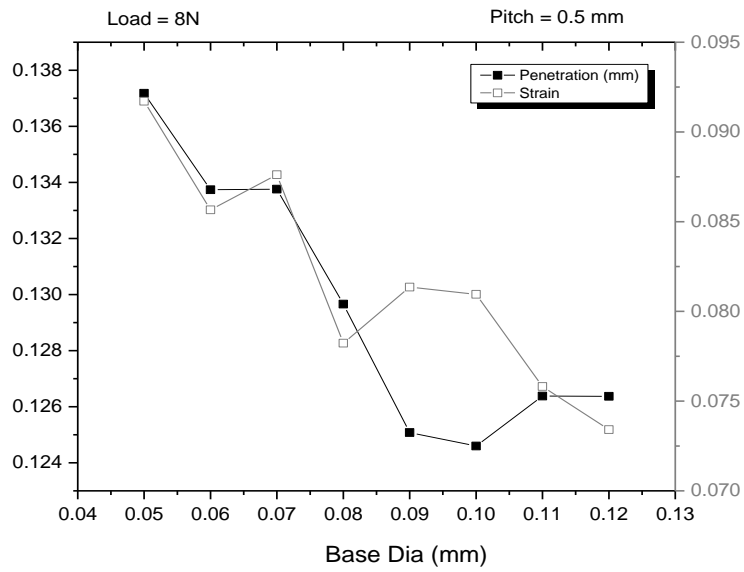


**Figure 10.33** Plot on Penetration, Strain vs. Base Dia. at 8 N Load for a Pitch 0.5 mm

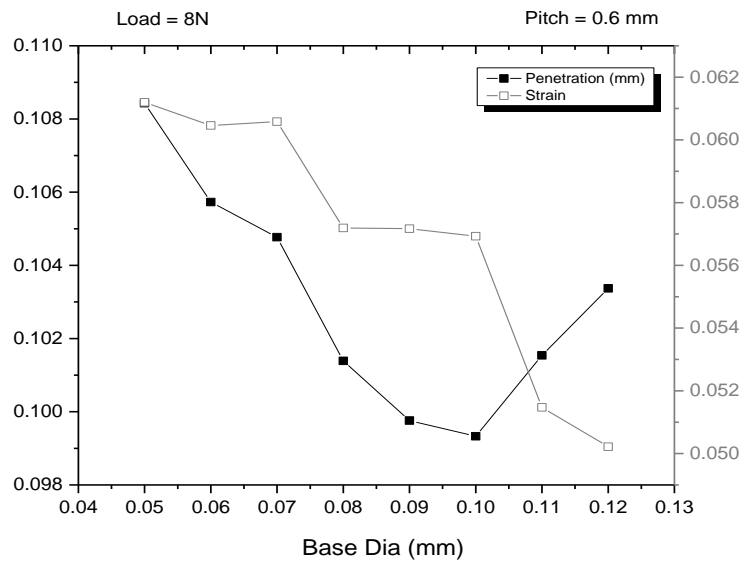


**Figure 10.34** Plot on Penetration, Strain vs. Base Dia. at 8 N Load for a Pitch 0.6 mm

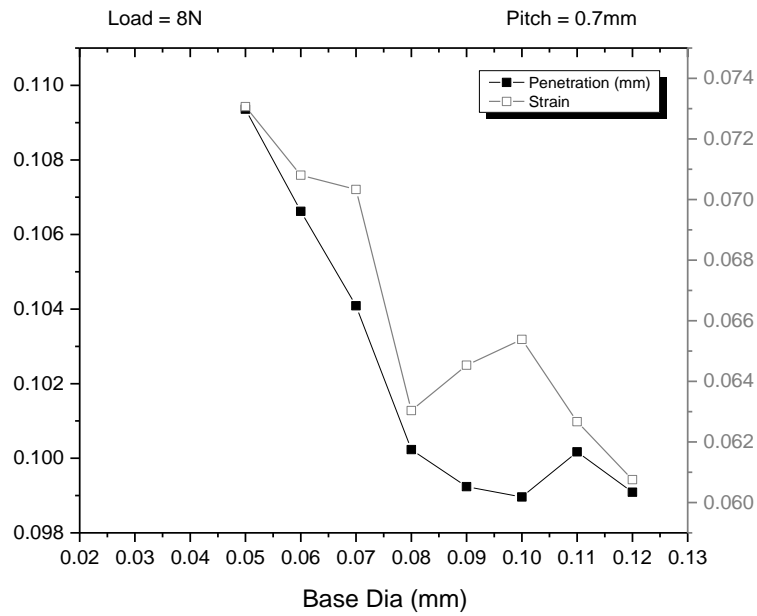


**Figure 10.35** Plot on Penetration, Strain vs. Base Dia. at 8 N Load for a Pitch 0.7 mm

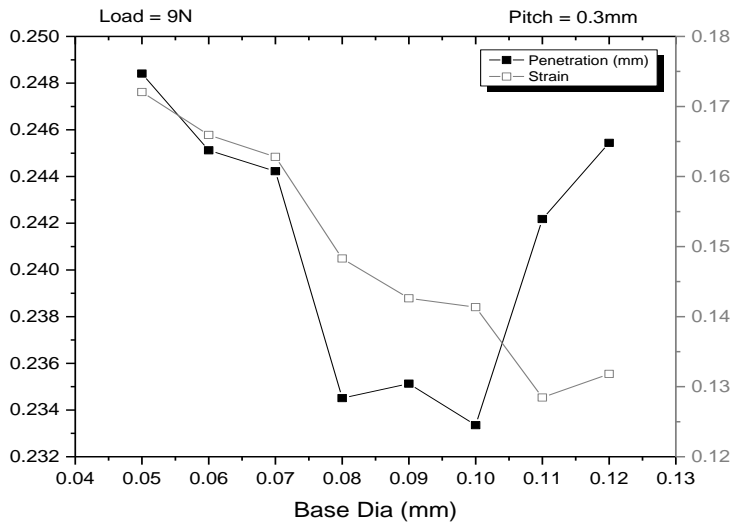


**Figure 10.36** Plot on Penetration, Strain vs. Base Dia. at 9 N Load for a Pitch 0.3 mm

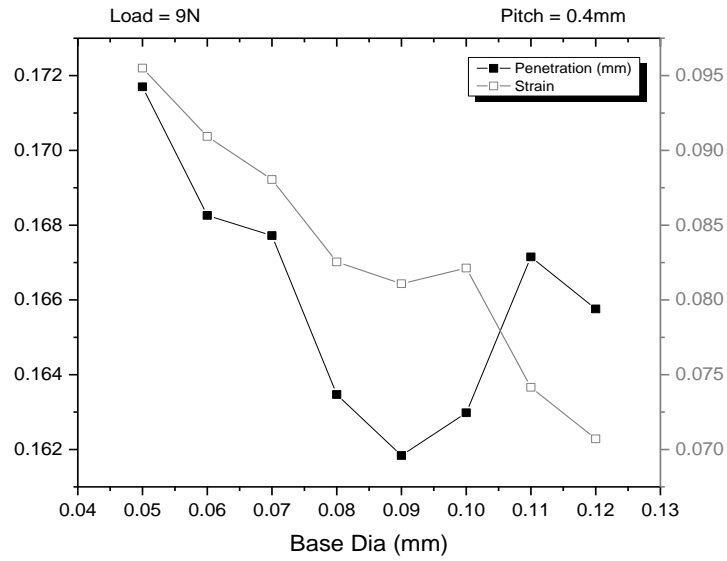


**Figure 10.37** Plot on Penetration, Strain vs. Base Dia. at 9 N Load for a Pitch 0.4 mm

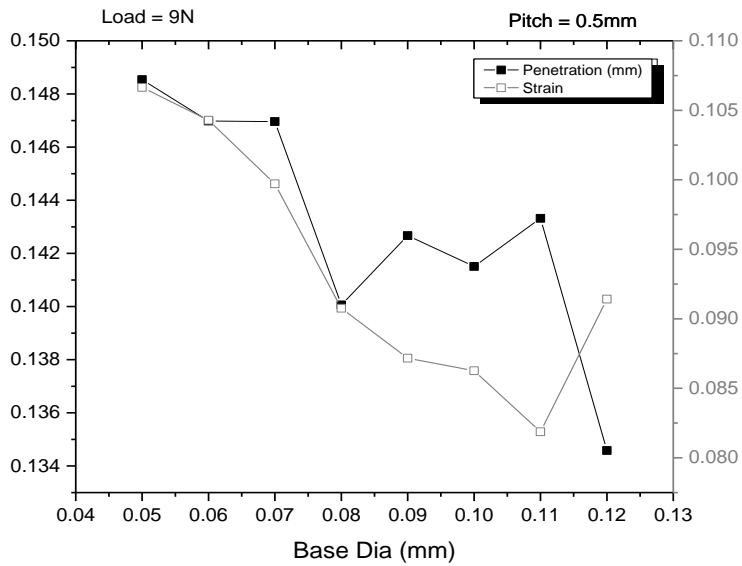


**Figure 10.38** Plot on Penetration, Strain vs. Base Dia. at 9 N Load for a Pitch 0.5 mm

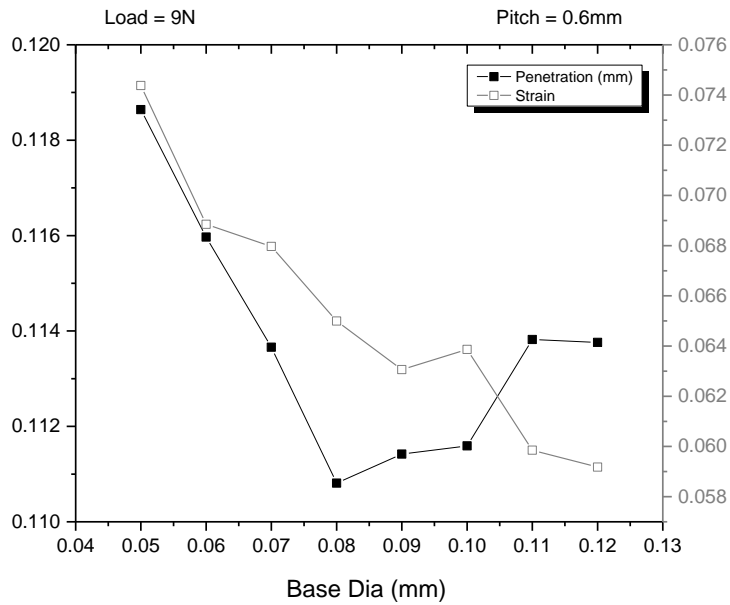


**Figure 10.39** Plot on Penetration, Strain vs. Base Dia. at 9 N Load for a Pitch 0.6 mm

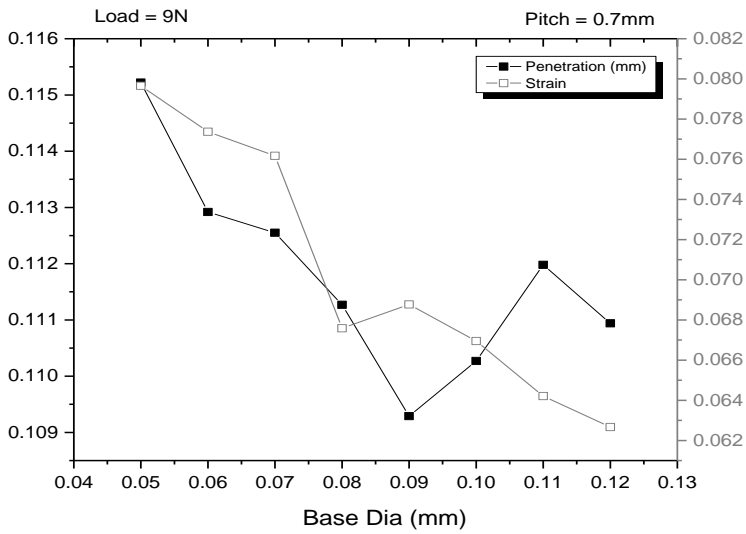


**Figure 10.40** Plot on Penetration, Strain vs. Base Dia. at 9 N Load for a Pitch 0.7 mm

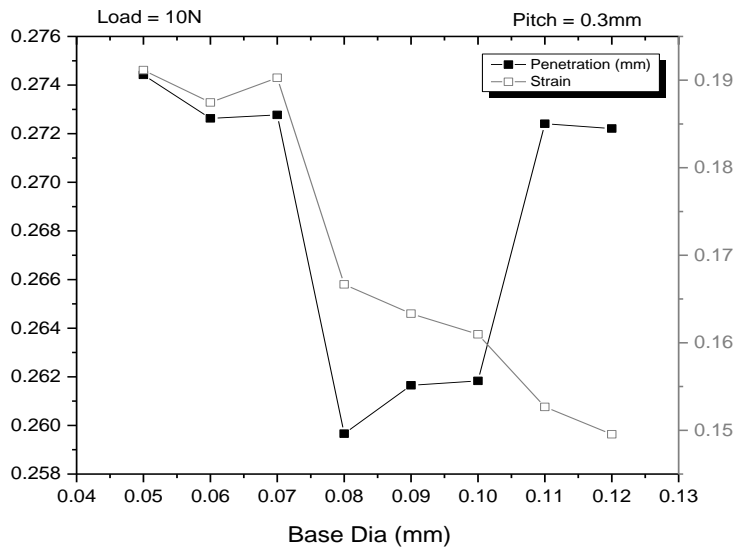


**Figure 10.41** Plot on Penetration, Strain vs. Base Dia. at 10 N Load for a Pitch 0.3 mm

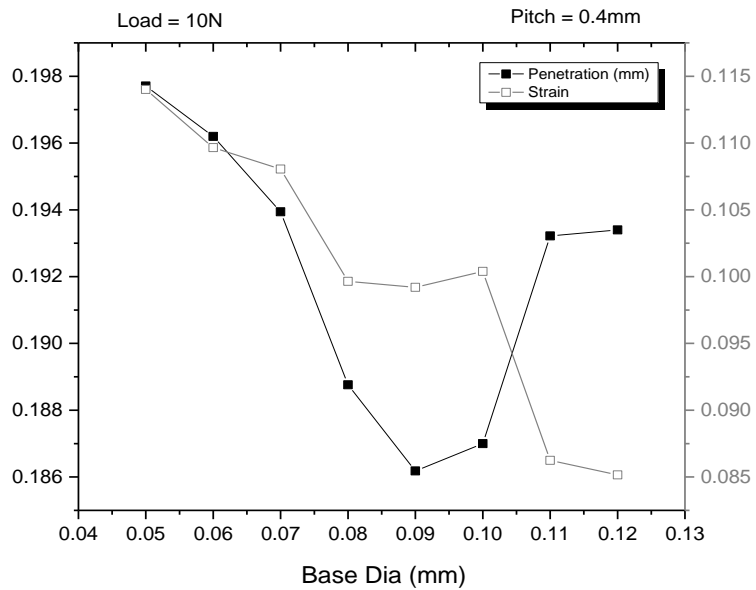


**Figure 10.42** Plot on Penetration, Strain vs. Base Dia. at 10 N Load for a Pitch 0.4 mm

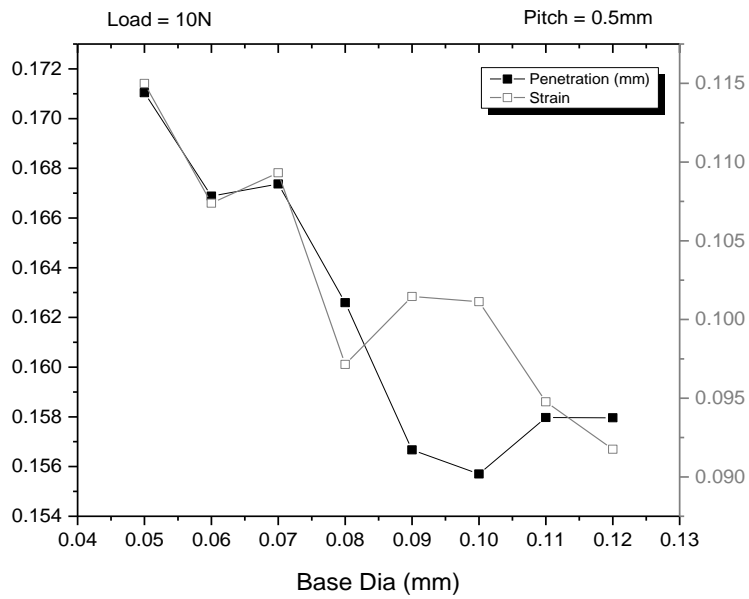


**Figure 10.43** Plot on Penetration, Strain vs. Base Dia. at 10 N Load for a Pitch 0.5 mm

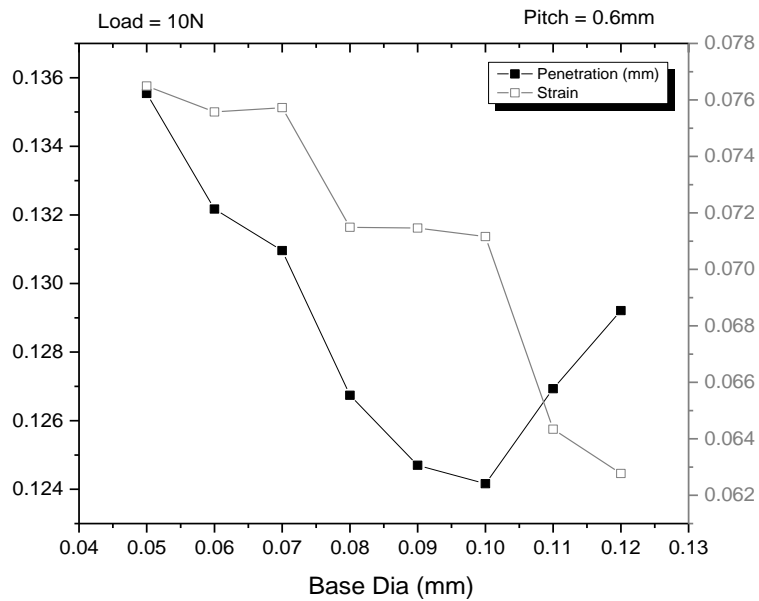


**Figure 10.44** Plot on Penetration, Strain vs. Base Dia. at 10 N Load for a Pitch 0.6 mm

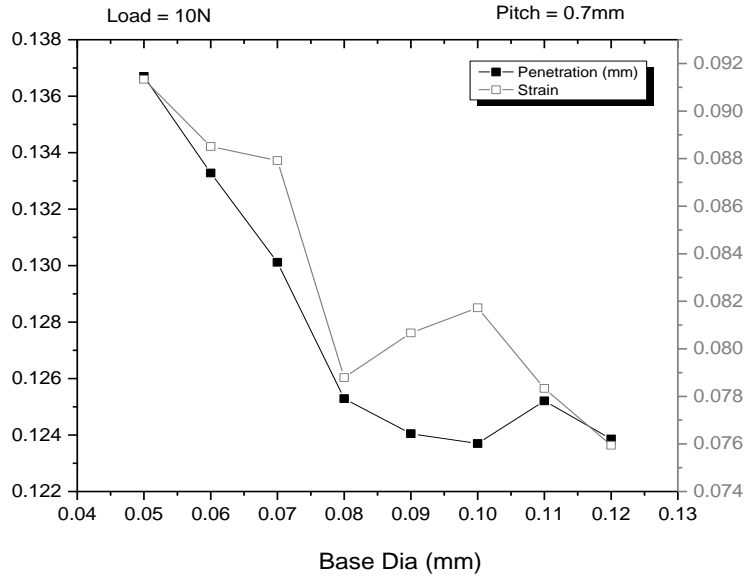


**Figure 10.45** Plot on Penetration, Strain vs. Base Dia. at 10 N Load for a Pitch 0.7 mm



### APPENDIX III

#### Micro Needle Dimensions after Micro Machining

<b>Measured Values of Micro Needle features</b>										
<b>Row/Column</b>	1,1	1,2	1,3	1,4	1,5	1,6	1,7	1,8	1,9	1,10
<b>Tip Dia. <math>\mu\text{m}</math></b>	5.4	7	6.7	6	4.7	11.38	4.6	10.19	<b>4.2</b>	6.75
<b>Base Dia. <math>\mu\text{m}</math></b>	115	118.3	115	114.5	114.4	115	113	<b>112.5</b>	115.6	113.4
<b>Height <math>\mu\text{m}</math></b>	233	226.7	225.7	228	227.3	220	227	221.8	221.4	223.8
<b>Row/Column</b>	2,1	2,2	2,3	2,4	2,5	2,6	2,7	2,8	2,9	2,10
<b>Tip Dia. <math>\mu\text{m}</math></b>	8.46	7.16	10.11	15	5.2	6.3	16.8	2.1	10.15	7.6
<b>Base Dia. <math>\mu\text{m}</math></b>	115.1	113.4	114.9	113	114	112	114.5	112.6	114.3	115.3
<b>Height <math>\mu\text{m}</math></b>	221.4	228.7	227.4	211	232	225	209.6	233	227	227.4
<b>Row/Column</b>	3,1	3,2	3,3	3,4	3,5	3,6	3,7	3,8	3,9	3,10

<b>Tip Dia. <math>\mu\text{m}</math></b>	8.8	7.5	10.54	14.7	2.56	6.33	9.3	8.4	9.277	8.43
<b>Base Dia. <math>\mu\text{m}</math></b>	112.5	116.8	115.5	115.8	115.7	115.8	114.1	115	116.4	115.9
<b>Height <math>\mu\text{m}</math></b>	223.2	225.2	209.5	212.5	229.4	232.5	223.3	216.1	220	224.9
<b>Row/Column</b>	4,1	4,2	4,3	4,4	4,5	4,6	4,7	4,8	4,9	4,10
<b>Tip Dia. <math>\mu\text{m}</math></b>	9.35	8.4	8	3.8	6.3	10.12	5.54	7.1	16.8	18.1
<b>Base Dia. <math>\mu\text{m}</math></b>	114.5	117	116.2	114.6	116.1	114.4	114.8	116	117.2	116.4
<b>Height <math>\mu\text{m}</math></b>	226.3	221.6	233.9	231.9	226	221.4	235.1	223	211.3	214.8
<b>Row/Column</b>	5,1	5,2	5,3	5,4	5,5	5,6	5,7	5,8	5,9	5,10
<b>Tip Dia. <math>\mu\text{m}</math></b>	7.6	8.1	6.3	4.7	15.81	10.95	5.8	8	3.4	16.43
<b>Base Dia. <math>\mu\text{m}</math></b>	116.3	117.1	117.5	116.5	116.8	115.6	116.9	116.8	118.2	117.3
<b>Height <math>\mu\text{m}</math></b>	227.8	222.3	226.5	231.8	231.4	219.4	230.1	225.6	236.1	211
<b>Row/Column</b>	6,1	6,2	6,3	6,4	6,5	6,6	6,7	6,8	6,9	6,10

<b>Tip Dia. <math>\mu\text{m}</math></b>	12.75	7.174	8.467	4.2	11.24	6.7	12.64	7.5	3.8	6.3
<b>Base Dia. <math>\mu\text{m}</math></b>	115.5	117.4	116.2	117.6	114.9	116.5	115.4	114.4	117.5	114.7
<b>Height <math>\mu\text{m}</math></b>	216.5	226.5	222.7	235.4	229.2	229.3	226.4	228.4	236.6	<b>236.7</b>
<b>Row/Column</b>	7,1	7,2	7,3	7,4	7,5	7,6	7,7	7,8	7,9	7,10
<b>Tip Dia. <math>\mu\text{m}</math></b>	10.12	8.4	17.32	9.7	9.8	6.74	8.46	9.2	7.17	9.72
<b>Base Dia. <math>\mu\text{m}</math></b>	117.3	114.9	117.6	115.9	117.5	115	116.6	117	116.4	116.9
<b>Height <math>\mu\text{m}</math></b>	228.5	227.4	203	229.4	225.7	227	227.3	223.4	227	227.1
<b>Row/Column</b>	8,1	8,2	8,3	8,4	8,5	8,6	8,7	8,8	8,9	8,10
<b>Tip Dia. <math>\mu\text{m}</math></b>	15.1	14.7	8	7.59	8	10.11	9.2	5.4	9.6	17.7
<b>Base Dia. <math>\mu\text{m}</math></b>	117.5	116.3	117.9	116.9	117	115.8	115.1	116	115.6	114.7
<b>Height <math>\mu\text{m}</math></b>	214	211.7	225.4	228.8	229.3	225.8	226.8	227	227.5	215.6

Micro Needle Dimensions after Micro Machining (Continuation)

<b>Measured Values of Micro Needle features</b>										
<b>Row/Column</b>	9,1	9,2	9,3	9,4	9,5	9,6	9,7	9,8	9,9	9,10
<b>Tip Dia. <math>\mu\text{m}</math></b>	8	11.8	3.8	5.9	9.3	6.3	8.8	8.8	8	<b>24.47</b>
<b>Base Dia. <math>\mu\text{m}</math></b>	115.9	115.7	118.2	117.8	117.6	<b>118.6</b>	117.9	117.2	116.8	116.3
<b>Height <math>\mu\text{m}</math></b>	232.5	223.8	233.2	233.3	229.5	233.6	234.4	225.7	228.7	201.7
<b>Row/Column</b>	10,1	10,2	10,3	10,4	10,5	10,6	10,7	10,8	10,9	10,10
<b>Tip Dia. <math>\mu\text{m}</math></b>	7.5	17.29	3.3	7.5	5.4	7.1	11	8.9	9.2	12.6
<b>Base Dia. <math>\mu\text{m}</math></b>	116.3	117	117.2	115	115.5	114	115.9	117.7	117.5	116.3
<b>Height <math>\mu\text{m}</math></b>	230	<b>209.4</b>	237.5	222.9	233.9	235.5	227.2	229.3	235.5	224

## APPENDIX IV

### Summary of Micro Needle Dimensions after Micro Machining

Sl. No.	Description	Value
1	Tip Diameter, Minimum, $\mu\text{m}$	4.20
2	Tip Diameter, Maximum, $\mu\text{m}$	24.47
3	Base Diameter Minimum, $\mu\text{m}$	112.50
4	Base Diameter, Maximum, $\mu\text{m}$	118.60
5	Height, Maximum, $\mu\text{m}$	236.7
6	Height, Minimum, $\mu\text{m}$	209.40